

Important Notice

This copy may be used only for the purposes of research and private study, and any use of the copy for a purpose other than research or private study may require the authorization of the copyright owner of the work in question. Responsibility regarding questions of copyright that may arise in the use of this copy is assumed by the recipient.

UNIVERSITY OF CALGARY

A seismic study of active faults, Canterbury, New Zealand

by

Jessie Marie Arthur

A THESIS

SUBMITTED TO THE FACULTY OF GRADUATE STUDIES
IN PARTIAL FULFILMENT OF THE REQUIREMENTS FOR THE
DEGREE OF MASTER OF SCIENCE

DEPARTMENT OF GEOSCIENCE

CALGARY, ALBERTA

SEPTEMBER, 2013

© JESSIE ARTHUR 2013

Abstract

The 2010-2011 Canterbury earthquake sequence on the South Island of New Zealand occurred in a region where hidden faults systems were unknown, but were suspected. Following the 2011 Christchurch earthquake, 2D seismic reflection data was acquired in the Canterbury region. The seismic data, along with a regional tectonic and geologic overview, is used to image, interpret, and identify faults extending to basement structure beneath the Canterbury Plains. Seismic risk hazard is further assessed through the multi-channel analysis of surface waves (MASW) method, where Rayleigh wave dispersion curves are inverted to generate shear wave velocity profiles. Low shear velocity areas are identified, indicating lower soil stiffness and thus risk of potential liquefaction which is an important characterization in seismically active areas. Further fault zone research is investigated by seismic physical modeling inspired by the Greendale Fault in New Zealand, and final imaged results are comparable to acquired field data.

Acknowledgements

This thesis is the result of a larger collaborative, which I am truly thankful for. I would like to start by thanking Don Lawton for taking me on as his student and providing such an interesting topic. Thank you Don for your time, guidance, direction, and showing me the true value of independent research while keeping me on my toes, ensuring I considered many different angles to solve a problem.

I had the opportunity to work with Dr. Jarg Pettinga from the University of Canterbury. Working with Jarg on the seismic interpretation of the 2D seismic lines collected in New Zealand proved to be the highlight of my research. I learned a great deal from Jarg, who was always willing to explain complicated concepts with clarity and patience. I would also like to thank Richard Jongens, a consulting geoscientist from New Zealand who graciously sent me his unpublished reports, figures, and conference poster which complemented my research.

I am thankful to the CREWES sponsors who supported this research and the CREWES staff. The support from CREWES staff ranged from moral to technical support. I would like to thank Laura Baird for encouragement and always looking out for me. I learned so much from Joe Wong, who is a vault of information and always available for a discussion – it was an absolute pleasure working with Joe. I would like to thank Malcolm Bertram for discussions on the New Zealand acquisition and always showing an interest in my research. A sincere thank you to Kevin Hall for providing some pictures of data acquisition and technical support when required. I also would like

to thank Rob Ferguson for always having an open door to discuss the complexities of surface waves, or raising a young family. Sincere thanks to Helen Isaac, Dave Henley, Rolf Maier, and Eric Gallant for their availability, discussions, and providing technical expertise. I would also like to thank Roohollah Askari for discussions on the MASW technique. I feel fortunate to have been part of such a supportive research group.

Camaraderie and peer support from fellow graduate students are a large part of graduate school, and I would like to thank Kim Pike, Patricia Gavotti, Heather Lloyd, Faranak Mahmoudian, Shahin Moradi, Steve Kim, Byron Kelly, Andrew Nichol, Dave Cho, and Peter Gagliardi for discussions, debates, and laughs when needed.

I would like to thank Kris Innanen and Elise Fear for their time and role taken on my defence committee. The comments and feedback were very much appreciated.

My return to school has been an endeavour on my life list, and I am extremely thankful to my husband, Danny Guenette, for being there every step of the way with love and perseverance. Juggling grad school and a new baby was not easy – who knew?! I would like to thank my sisters Erin and Bonnie for encouragement and providing a listening ear or a kick in the pants when needed. I am indebted forever to my parents, Rick and Nathene Arthur, and my inlaws Mike and Diana Guenette, for moral support and millions of hours of childcare.

Dedication

To my husband, Danny

And to my two year old son, Gabe.

Table of Contents

Abstract	ii
Acknowledgements	iii
Dedication	v
Table of Contents	vi
List of Tables	ix
List of Figures and Illustrations	x
List of Symbols, Abbreviations and Nomenclature	xviii
CHAPTER ONE: INTRODUCTION	1
1.1 Background	1
1.2 Geographic setting of the study area	1
1.3 The 2010-2011 Canterbury Earthquake sequence	4
1.3.1 The 4 September 2010 Darfield Earthquake	5
1.3.2 The 22 February 2011 Christchurch Earthquake	8
1.3.3 Aftershocks	9
1.4 Thesis objectives	9
1.5 Contribution of the thesis	12
1.6 Thesis outline	12
1.7 Datasets and software used	13
CHAPTER TWO: SEISMIC INTERPRETATION OF THE CANTERBURY PLAINS, NEW ZEALAND	15
2.1 Introduction	15
2.2 Tectonic and geologic overview	15
2.2.1 The tectonic history of New Zealand	16
2.2.2 The current tectonic setting of New Zealand	18
2.2.3 The tectonic setting of the Canterbury Region, South Island	20
2.2.4 Geologic setting and stratigraphy of the Canterbury Plains	24
2.2.4.1 Permian to Early Cretaceous basement	24
2.2.4.2 Late Cretaceous to Pleistocene volcanic and sedimentary rocks	26
2.2.4.3 Quaternary Sedimentary deposits	29
2.3 Additional information for seismic interpretation	29
2.3.1 Wells	29
2.3.2 Previous geophysical work	30
2.3.3 Earthquake history in the Canterbury Region	32
2.4 Seismic Interpretation	33
2.4.1 Data acquisition and processing	33
2.4.2 Christchurch seismic data	33
2.4.2.1 Seismic interpretation of Line 1, New Brighton Beach	34
2.4.2.2 Seismic interpretation of Line 2, Barbadoes Street	40
2.4.2.3 Seismic interpretation of Line 3, Highfield Road	44
2.4.3 Discussion on fault reactivation	47

CHAPTER THREE: MASW INVESTIGATION OF AN ACTIVE FAULT ZONE	49
3.1 Introduction.....	49
3.1.1 Liquefaction.....	50
3.1.1.1 Definition	50
3.1.1.2 Liquefaction and application of shear wave velocity measurements....	51
3.1.2 Seismic wave types.....	52
3.1.2.1 Body waves.....	52
3.1.2.2 Surface waves	53
3.1.3 Dispersion.....	54
3.2 Theoretical background of the MASW method.....	55
3.2.1 Acquisition.....	55
3.2.2 Dispersion curve – Fundamental mode	58
3.2.3 Inversion	60
3.3 Data acquisition and study area	62
3.3.1 Data acquisition at New Brighton Beach (Line 1)	63
3.3.2 Data acquisition at Highfield Road (Line 3)	63
3.4 Surface wave analysis.....	66
3.4.1 New Brighton Beach (Line 1)	66
3.4.1.1 Data processing.....	66
3.4.1.2 Dispersion curve analysis	72
3.4.1.3 Inversion analysis.....	76
3.4.2 Highfield Road (Line 3)	83
3.4.2.1 Data processing.....	83
3.4.2.2 Dispersion Curve Analysis	86
3.4.2.3 Inversion Analysis	90
3.5 . Discussion.....	94
3.5.1 Discussion of New Brighton Beach results	94
3.5.2 Discussion of Highfield Road results	98
 CHAPTER FOUR: SEISMIC PHYSICAL MODELING OF AN ACTIVE FAULT ZONE.....	 100
4.1 Introduction.....	100
4.1.1 Physical modeling background.....	100
4.1.2 Seismic resolution theory	100
4.1.2.1 Vertical resolution.....	101
4.1.2.2 Lateral resolution	101
4.2 Physical modeling.....	102
4.2.1 The physical models	102
4.2.2 Physical modeling data acquisition	105
4.3 Seismic data processing	109
4.3.1 Zero-offset data processing	109
4.3.2 Common source data processing	115
4.4 Event identification.....	126
4.5 Discussion.....	129

CHAPTER FIVE: CONCLUSIONS AND RECOMMENDATION FOR FUTURE WORK	133
5.1 Seismic interpretation of the Canterbury Plains	133
5.1.1. Conclusions	133
5.1.2 Recommendations for future work	134
5.2 MASW investigation of an active fault zone	135
5.2.1 Conclusions	135
5.2.2. Recommendations for future work	135
5.3 Seismic physical modeling of an active fault zone	137
5.3.1. Conclusions	137
5.3.2 Recommendations for future work	138
REFERENCES	139
APPENDIX A: GEOLOGIC TIMESCALE	156
APPENDIX B: ENVIRONMENT CANTERBURY BEXLEY BOREHOLE	157
APPENDIX C: STACKING VELOCITIES OF SEISMIC DATA	165
C.1. Velocity structure beneath New Brighton Beach (Line 1)	165
C.2. Velocity structure beneath Barbadoes Street (Line 2)	166
C.3. Velocity structure beneath Highfield Road (Line 3)	167
APPENDIX D: ENVIRONMENTAL CANTERBURY WELL LOGS	168
APPENDIX E: PROCESSING JOB FLOWS FOR PHYSICAL MODELING	171
E.1. VISTA job flow created for zero-offset data	171
E.2. VISTA job flow for common-source data (Part 1: Filtering and deconvolution)	171
E.3. VISTA job flow for common-source data (Part 2: Velocity analysis)	172
E.4. VISTA job flow for common-source data (Part 3: Apply NMO and stack)	172
E.5. VISTA job flow for common-source data (Part 4: 2D Post-stack Kirchhoff migration)	173

List of Tables

Table 3-1. Seismic data acquisition parameters.....	63
Table 3-2. Initial model for 10 layers, variable density, and a fixed Poisson ratio of 0.4.....	80
Table 3-3. Initial model for 10 layers, variable density, and a fixed Poisson ratio of 0.15.....	80
Table 3-4. Initial model for 10 layers, variable density, and a fixed Poisson ratio of 0.4.....	91
Table 4-1. Summary of physical model prototypes	104
Table 4-2: Summary of expected two-way arrival times of the identified events.	129

List of Figures and Illustrations

- Figure 1-1. (a) New Zealand plate tectonics, with the Canterbury Region indicated. (b) Map of the Canterbury Plains and surrounding area, overlaying a shaded topographic relief model. Figure adapted from Forsyth et al. (2008)..... 3
- Figure 1-2. Map showing fault trace of the Greendale Fault (in red) which ruptured the surface on 4 September 2011 during the Darfield earthquake. The Port Hills Fault (in dashed yellow) is the surface projected fault location based on GPS and DInSAR data from Beaven et al. (2012). Event epicentres are green stars. Google earth V 7.0.3.8542. (17 Jan 2013) New Zealand. 43°42'07.48"S, 172°30'08.00"E, Eye alt 108.78 km. SIO, NOAA, U.S. Navy, NGA, GEBCO. Cnes/Spot Image 2013. <http://www.earth.google.com> [May 30, 2013]. 5
- Figure 1-3. Aerial photograph of the E-W trending Greendale Fault. A drainage canal is displaced by shear fractures along the fault surface. Image taken by Richard Jongens of GNS science..... 6
- Figure 1-4. LiDAR hillshade DEM along the Greendale Fault demonstrating a left stepping en echelon rupture. Fault step-over and bulges are indicated. Red arrows indicate lateral displacement. Yellow circles denote damaged buildings. Image adapted from Van Dissen et al. (2011). 8
- Figure 2-1. The tectonic setting of New Zealand, simplified. Google earth V 7.0.3.8542. (2013) New Zealand. 41°30'22.33"S, 173°28'17.01"E, Eye alt 2680.23 km. SIO, NOAA, U.S. Navy, NGA, GEBCO. Cnes/Spot Image 2013. <http://www.earth.google.com> [May 30, 2013]..... 19
- Figure 2-2. Structural domain map of New Zealand's South Island and the Canterbury Region from Pettinga et al. (2001). The focus of this research is located in Domain 7, where hidden faults are present. The Greendale Fault, which ruptured during the 4 September 2010 earthquake is marked as 'GF' within the boundary of the Canterbury Plains..... 23
- Figure 2-3. Geologic map of basement rocks on the South Island of New Zealand. Adapted from MacKinnon [1983]. The Torlesse terrane, part of the Eastern province is highlighted in green..... 25
- Figure 2-4. (a) Stratigraphic chart of the western Canterbury Plains. Adapted from Forsyth et al. (2008). (b) Map area showing location of (a). Adapted base map provided by Environment Canterbury..... 27
- Figure 2-5. Map showing petroleum wells Arcadia-1 (drilled in 2000) and Leeston-1 (drilled in 1969). Google earth V 7.0.3.8542. (4 September 2013) New Zealand. 43°35'13.73"S, 172°22'30.02"E, Eye alt 148.29 km. SIO, NOAA, U.S. Navy,

NGA, GEBCO. TerraMetrics 2013. http://www.earth.google.com [June 29, 2013].	30
Figure 2-6. Overview map showing seismic data acquisition in the city of Christchurch, New Zealand. Line 1 (orange) is along New Brighton Beach, and Line 2 (yellow) is along Barbadoes Street. Google earth V 7.0.3.8542. (25 April 2012) Christchurch, New Zealand. 43°32'06.48"S, 172°40'34.28"E, Eye alt 17.68 km. TerraMetrics 2013. http://www.earth.google.com [May 30, 2013].	34
Figure 2-7. New Brighton Beach seismic line with corresponding stations is shown along the east coast of Christchurch. The Environment Canterbury Bexley testbore location is illustrated by the green star. The projection of the Port Hills Fault to the surface is shown by a dashed orange line and is based on GPS and DInSAR data from Beaven et al. (2012). Figure adapted from Hall et al. (2011). Google earth V 6.0.3.2197. (2011) Christchurch, New Zealand. 43°30'04.99"S, 172°48'32.49"E, Eye alt 10.89 km. TerraMetrics 2011, Whereis® Sensis Pty Ltd, and Geoeye 2011. http://www.earth.google.com [Oct 17, 2011].	35
Figure 2-8a. Uninterpreted New Brighton Beach 2D seismic line with 3x vertical exaggeration. The Bexley testbore is 1 km to the west of New Brighton Beach, and the borehole location is projected onto the seismic line.....	37
Figure 2-8b. Interpreted New Brighton Beach 2D seismic line with 3x vertical exaggeration. The green horizon represents the Wainoni gravels, the yellow horizon represents the Early Pleistocene Top of Kowai Formation, and the red horizon represents the Miocene Volcaniclastics. The Port Hills Fault is interpreted 400 ms below stations 500-520. An additional projected fault shown in black dashed line towards the north end of the seismic line just intersects the Miocene Volcaniclastics.	38
Figure 2-9. Barbadoes Street seismic line (in blue). Started on south end at station 205 and ended north at station 571. Google earth V 7.0.3.8542. (25 April 2012) Christchurch, New Zealand. 43°32'06.98"S, 172°40'34.27"E, Eye alt 10.24 km. Whereis® Sensis Pty Ltd. and TerraMetrics 2013. http://www.earth.google.com [June 7, 2013].	40
Fig 2-10a. Barbadoes Street seismic profile without interpretation, 3x vertical exaggeration.	42
Figure 2-10b. Barbadoes Street seismic profile with interpretation, 3x vertical exaggeration. The green horizon represents the Wainoni gravels, the yellow horizon represents the Early Pleistocene Top of Kowai Formation, and the red horizon represents the Miocene Volcaniclastics. Possible projected faults are indicated in dashed black lines. Also interpreted is a channel and fill zone in the near surface.	43

- Figure 2-11. Highfield Road seismic line (in yellow). Started on south end at station 306 and ended north at station 641. The Greendale Fault ruptures the surface in an E-W orientation. Greendale Fault trace based on Holden et al. (2011). Google earth V 7.0.3.8542. (28 January 2013) Highfield Road, New Zealand. 43°35'34.06"S, 172°12'54.20"E, Eye alt 5.6 km. DigitalGlobe 2013. <http://www.earth.google.com> [June 29, 2013]..... 44
- Figure 2-12. (a) Highfield Road seismic line uninterpreted. (b) With interpretation. The 125,000 year gravels are represented by the light blue horizon, the Top of the Kowai formation is represented by the yellow horizon, the Miocene volcanoclastics/Mid-Tertiary limestone is represented by the red horizon, the Top of the Paleogene (?) is represented in green, and the undifferentiated Mesozoic basement is picked in brown. The Greendale fault is illustrated below station 440, where the fault ruptured the surface. Fault splays are indicated by short dashed lines off the main Greendale Fault..... 46
- Figure 3-1. Radiation pattern of Rayleigh waves generated by a vertical source. Adapted from Lai, C.G. (2005)..... 53
- Figure 3-2. Near-field and far-field effect of ground roll observed in swept-frequency records obtained by uncorrelated Vibroseis records. Good quality data is shown in (a), where the source offset is 27 m. The near-field effect is shown in (b) with a source offset is 1.8 m. Linear coherency is reduced by weaker energy and discontinuous energy packets. Arrivals show increased frequencies. The far-field effect is shown in (c) with a source offset of 89 m. Linear coherency is reduced due to interference from high velocity body waves. Far offset effects are seen as a decrease in ground roll slope (an increase phase velocity). Adapted from Park et al. (1999). 58
- Figure 3-3. New Brighton Beach seismic line, east of Christchurch city center. The yellow box highlights the segment used for MASW analysis. Environment Canterbury well is indicated by a green star. Adapted from Hall et al., (2011). Image © 2011 TerraMetrics and © 2011 Whereis® Sensis Pty Ltd and Image © 2011 GeoEye (Google Earth, 2011)..... 65
- Figure 3-4. Highfield Road seismic line, approximately 35 km west of Christchurch city center. The Environment Canterbury well is indicated by a green star. The Greendale Fault was transverse near Station 440. Adapted from Hall et al., (2011). Image © 2011 TerraMetrics and © 2011 Whereis® Sensis Pty Ltd and Image © 2011 GeoEye (Google Earth, 2011)..... 65
- Figure 3-5. Seismic data processing flow applied prior to dispersion curve analysis. 66
- Figure 3-6. Frequency content of a raw shot record from New Brighton Beach. The frequency content for entire window (A) is shown, and the frequency content for a window focused on the surface waves is shown (B)..... 67

Figure 3-7. Seismic acquisition for (a) split-spread geometry, and (b) off-end geometry.....	68
Figure 3-8. (a) Raw shot record showing direct arrivals (A at 1689 m/s) and surface wave events (B & C at 229m/s and 111 m/s respectively), (b) with a 0-3-32-38 Hz bandpass filter applied, (c) with a Radial Trace filter applied.	70
Figure 3-9. (a) Shot gather with first arrivals displayed, and (b) with a top mute applied.	71
Figure 3-10. Overtone image displaying the fundamental mode, and higher modes. A broad phase velocity range (0 - 3000m/s) identifies fundamental and higher modes.	73
Figure 3-11. Testing spread length parameters and dispersion curve resolution of the fundamental mode. (a) Spread length = 300 m; (b) Spread length = 200 m; (c) Spread length = 150 m; (d) Spread length = 100 m.	74
Figure 3-12. (a) Surface wave range identified in SurfSeis 3.15 for a 100 m spread length, (b) Corresponding dispersion image	75
Figure 3-13. (a) Fundamental model picks for the dispersion curve at Station 601, (b) Inversion results, where the black circles show the trend of the measured fundamental mode, the dashed blue line represents V_s of the initial model, and the solid blue line represents V_s of the final inversion results.....	78
Figure 3-14. New Brighton Beach inversion results with a constant Poisson ratio = 0.4, and different densities provided in the initial model. (a) with $\rho=1700$ kg/cm ³ in the initial model, (b) $\rho=2000$ kg/cm ³ , and (c) variable density.	81
Figure 3-15. New Brighton Beach inversion results with Poisson ratio = 0.15 provided in the initial model. (a) with $\rho=2000$ kg/cm ³ in the initial model, (b) variable density.	82
Figure 3-16. Raw shot record and frequency content from Highfield Road on left hand side. With AGC applied on right hand side. This dataset has a peak frequency of 30 Hz.....	84
Figure 3-17. (a) Raw shot record before RT domain filtering, (b) after RT domain filtering, and (c) airwave and signal discarded from the RT domain filter.....	85
Figure 3-18. Spread lengths of (a) 1940, (b) 1000, (c) 500, and (d) 300 m were tested in producing the dispersion images. The fundamental mode resolution was best enhanced with a spread length of 300 m.....	87
Figure 3-19. Dispersion curve comparison between input data with (a) a maximum frequency 30 Hz low pass RT domain filter, and (b) a maximum frequency 15	

Hz low pass RT domain filter. The frequency of the fundamental mode ranges from 13 to 28 Hz.	88
Figure 3-20. (a) Shot record at Station 417 used for dispersion curve analysis. The analysis area and fault location are highlighted (b)Resulting dispersion image approaching the Greendale Fault. Amplitudes are high scattered and have low S/N ratios. The blue trend line with small squares shows where the curve had been previously picked prior to emergence of the fault zone within the analysis area.	89
Figure 3-21. The final S-wave profiles for three locations before (Record 321), near (Record 417), and after the fault zone (Record 550). Initial Vs measurements (blue dashed line) from the initial model is shown, with the final Vs inversion result (solid blue line). The extracted dispersion curve picks are plotted solid black circles, representing the measured fundamental mode.	92
Figure 3-22. (a) The final S-wave velocity model for Highfield Road, and (b) associated RMSE. The RMSE provides an indication of where the inversion results are unreliable.	93
Figure 3-23. S-wave velocity inversion results for (a) New Brighton Beach, and (b) Highfield Road. Dashed lines indicate areas of lower S-wave velocity. Overall lower shear wave velocities are observed at New Brighton Beach.	97
Figure 4-1. The Fresnel zone radius (r) for a coincident source and receiver. Adapted from Yilmaz (1987).	102
Figure 4-2. Schematic diagram of seismic acquisition over the final limestone model with corresponding field dimensions. The transducers are positioned 200 m over the model.	107
Figure 4-3. The Limestone-Wax model in the physical modeling water tank (left), and the limestone model (right), held in place by putty prior to fault zone infill. The blue 'x' signifies the zero marker location.	107
Figure 4-4. Plan view of the zero-offset acquisition. The Tx-Rx pair moved in 5 m increments and have 50 m offset.	108
Figure 4-5. General processing flow applied to the zero-offset data.	110
Figure 4-6. (a) Raw image of the zero-offset seismic data. (b) Wiggle trace with a zoom on fault zone.	111
Figure 4-7. Autocorrelation of the deconvolved data is examined. (a) Raw data. Operator lengths of (b) 20 ms; (c) 40 ms; and (d) 60 ms. The yellow box highlights the signal at the bottom of the limestone model.	112

Figure 4-8. (a) Raw data. The deconvolved data with tested operator lengths of b) 20 ms, c) 40 ms, and d) 60 ms.	113
Figure 4-9. Noise attenuated in the FK domain with a symmetrical fan filter. (a) Input, (b) Applied filter, (c) Output, (d) With noise removed.....	114
Figure 4-10. Comparisons of the final 2D Kirchhoff migrated image with tested migration apertures. (a) Raw data with scaling, (b) Migration aperture = 50 traces, (c) Migration aperture = 15 traces, (d) Selected migration aperture = 10 traces.	115
Figure 4-11. General processing flow applied to the common-source data.....	116
Figure 4-12. Spectral analysis of (a) Shot point 41 of the Limestone-Acrylic model, and (b) Shot point 135 of the Limestone-Water model. Two bands of energy are apparent throughout the data.....	117
Figure 4-13. Noise attenuated in the FK domain with a symmetrical fan filter on the Limestone-Acrylic model in the shot domain. (a) Input data, (b) Applied filter, (c) Output data, and (d) Noise removed.....	118
Figure 4-14. Spiking deconvolution testing on SP 101 of the Limestone-Water fault model. (a) Raw shot, (b) Operator length = 20 ms, (c) = 40 ms, (d) = 90 ms, and (e) = 120 ms. The 20 ms operator length was selected.	119
Figure 4-15. A comparison of the pre- and post- deconvolved shot point 101 for the Limestone-Acrylic model. FK-Filter and ExpTPower is applied. (a) No decon, AmpSc = 8, (b) With decon (operator = 20 ms), AmpSc = 8. (c) & (d) are the same, but have AGC applied prior.....	120
Figure 4-16. Semblance and constant velocity stack analysis for (a) the Limestone-Acrylic model, and (b) the Limestone-Water model. Images show the velocity picks at CMP 201, which is where the center of the fault is located. The velocities and a mute function were picked on every tenth CMP.....	122
Figure 4-17. The final velocity models for (a) the Limestone-Acrylic model, and (b) the Limestone-Water model. A decrease in velocity is seen in the water filled fault zone compared to the acrylic filled fault zone.....	123
Figure 4-18. (a) Brute stack of the Limestone-Acrylic fault model seismic section, (b) Brute stack of the Limestone-Water fault model seismic section. With AGC.	124
Figure 4-19. Noise attenuated in the FK domain with a symmetrical fan filter on the Limestone-Water model CMP stack. (a) Input data, (b) Applied filter, (c) Output data, and (d) Noise removed.	125

Figure 4-20. (a) CMP stack of the Limestone-Acrylic fault model, followed by (b) Post-stack migration. (c) CMP stack of the Limestone-Water fault model, followed by (d) Post-stack migration.....	126
Figure 4-21. Event identification by ray tracing. A: Direct arrival (~32 ms), B: Water bottom/top of fault (~270 ms), C: Bottom of limestone (~380-400 ms), D: Bottom of water filled fault (~720 ms), E: Source ghost (~1020 ms), F: Receiver ghost/multiple of water bottom (~1275 ms).....	128
Figure 4-22. Average trace calculation showing identified reflection events in the shot record. The traces calculated in the average are shown in the inset figure.....	128
Figure 4-23. Illustration of events transmitted and received by the transducers. The ray paths taken through water and the model are used to calculate expected arrival time.	129
Figure 4-24. Final postmigrated images of the modeled fault zone. (a) Common-source Limestone-Water fault model. (b) Zero-offset Limestone-Water fault model. (c) Common-source Limestone-Acrylic fault model. (d) Zero-offset Limestone-Acrylic fault model.	131
Figure 4-25. Post-stack migrated seismic sections imaging a fault rupturing the surface for (a) the physical model (b) the Greendale Fault zone, New Zealand. The deformed fault zone is outlined by a dashed black line.....	132
Figure A1. Geologic time scale listing events focused on New Zealand.	156
Figure B1-1. Environment Canterbury Well Log M35/6068 Bexley Borehole Page 1 of 8.	157
Figure B1-2. Environment Canterbury Well Log M35/6068 Bexley Borehole Page 2 of 8.	158
Figure B1-3. Environment Canterbury Well Log M35/6068 Bexley Borehole Page 3 of 8.	159
Figure B1-4. Environment Canterbury Well Log M35/6068 Bexley Borehole Page 4 of 8.	160
Figure B1-5. Environment Canterbury Well Log M35/6068 Bexley Borehole Page 5 of 8.	161
Figure B1-6. Environment Canterbury Well Log M35/6068 Bexley Borehole Page 6 of 8.	162
Figure B1-7. Environment Canterbury Well Log M35/6068 Bexley Borehole Page 7 of 8.	163

Figure B1-8. Environment Canterbury Well Log M35/6068 Bexley Borehole Page 8 of 8.	164
Figure C1. RMS velocities provided by Sensor Geophysical Ltd. and overlain on processed seismic data acquired at New Brighton Beach, Christchurch, New Zealand. Vertical exaggeration x2, for 2000 m/s.....	165
Figure C2. RMS velocities provided by Sensor Geophysical Ltd. and overlain on processed seismic data acquired at Barbadoes Street, Christchurch, New Zealand. Vertical exaggeration x2, for 2000 m/s.....	166
Figure C3. RMS velocities provided by Sensor Geophysical Ltd. and overlain on processed seismic data acquired at Highfield Road, Canterbury, New Zealand. Vertical exaggeration x2.5, for 2400 m/s.....	167
Figure D1-1. Environment Canterbury Well Log M35, New Brighton Beach. Page 1 of 2.	168
Figure D1-2. Environment Canterbury Well Log M35, New Brighton Beach. Page 2 of 2.	169
Figure D1-3. Environment Canterbury Well Log M35, Highfield Road Page 1 of 1. ...	170

List of Symbols, Abbreviations and Nomenclature

Symbol	Definition
°	Degree
1D	One-dimensional space
2D	Two-dimensional space
3D	Three-dimensional space
AGC	Automatic gain control
BP	British Petroleum
cm/yr	Centimeter per year
CMP	Common midpoint
CREWES	Consortium for Research in Elastic Wave Exploration Seismology
C_w	Phase velocity for w
dB	Decibel
DInSar	Differential Radar Interferometry
EQC	Earthquake commission
f	Frequency
GPR	Ground Penetrating Radar
GPS	Global Positioning System
h	Layer thickness
Hz	Hertz
k	Wavenumber
kg/ cm ³	Kilogram per centimeter cubed
KGS	Kansas Geological Survey
KHz	Kilohertz
km	Kilometers
L	Receiver spread length
m	Meters
m/s	Meters per second
Ma	MegaAnnum
MHz	Megahertz
mm	Millimeter
mm/yr	Millimeter per year
ms	Millisecond
Mw	Moment magnitude
NMO	Normal moveout
p	Phase slowness
P-wave	Compressional wave
r	Radius of Fresnel zone
RMSE	Root mean square error
RT	Radial trace
Rx	Receiver location
s	Second

S/N	Signal to Noise
SEGY	File format for storing seismic data
S-wave	Shear wave
<i>T or t</i>	Time
Tx	Source location
<i>v</i>	Velocity
Vp	Compressional wave velocity
Vs	Shear wave velocity
w-v	Frequency-Phase
<i>x</i>	Offset
Zmax	Maximum depth
<i>Zo</i>	Depth for a coincident source and receiver
<i>λmax</i>	Maximum wavelength
ρ	Density
σ_1	Maximum stress
τ	Intercept time
ϕ	Phase shift
ω	Angular frequency

Chapter One: INTRODUCTION

1.1 Background

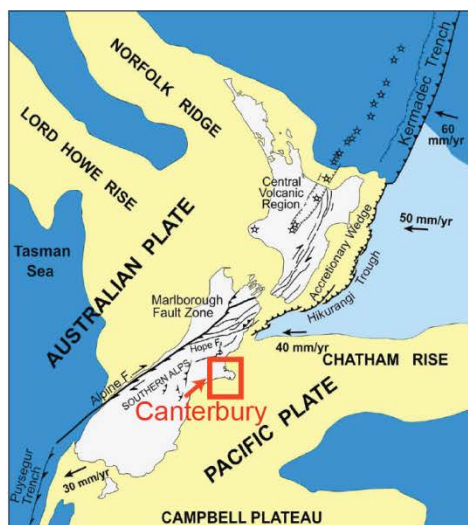
New Zealand is a seismically active region, located within a complex tectonic environment. The 2010-2011 Canterbury earthquake sequence in the Canterbury Plains on the South Island of New Zealand ruptured previously unknown fault systems, and resulted in severe damage to infrastructure and loss of life. The region continues to experience aftershock activity in the present day. Identifying faults in seismically active populated areas is essential in geotechnical engineering applications and seismic hazard risk assessment in earthquake studies. Seismic reflection and imaging techniques provide a means to identify and characterize fault zones, and an understanding of the regional tectonics and geology is essential for interpreting the seismic data.

1.2 Geographic setting of the study area

The Canterbury Region on the South Island of New Zealand (Figure 1-1a) is the largest government administrated region in all of New Zealand. The region includes the Canterbury Plains, the city of Christchurch, the Clarence River catchment to the north, the Waitaki River catchment to the south, and the mountains to the west (Environment Canterbury, 2013a). The Canterbury Plains are constrained within the Canterbury Region, and are bound by the foothills of the Southern Alps to the west, and Banks Peninsula and the Pacific Ocean to the east (Figure 1-1b). The Northern Canterbury Plains border basin and range topography, whereas flat alluvial outwash plains are represented by the central area (Forsyth et al., 2008).

Two areas are of interest for this research. The first location is on the east coast of the Canterbury Region in the city of Christchurch, and the second area of interest is located in the central Canterbury Plains; these areas are shown in the red highlighted rectangles in Figure 1-1.

a.



b.

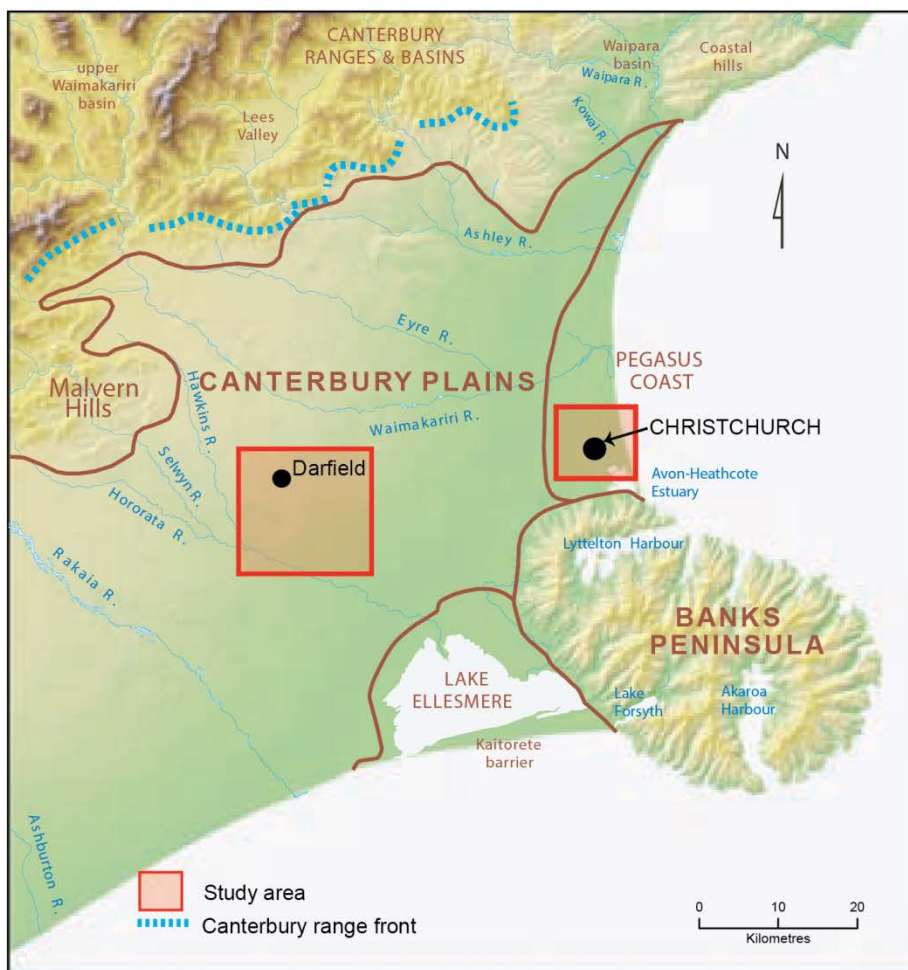


Figure 1-1. (a) New Zealand plate tectonics, with the Canterbury Region indicated. (b) Map of the Canterbury Plains and surrounding area, overlaying a shaded topographic relief model. Figure adapted from Forsyth et al. (2008).

1.3 The 2010-2011 Canterbury Earthquake sequence

The Canterbury earthquake sequence includes the 4 September 2010 Darfield earthquake with an epicenter approximately 40 km west of Christchurch, the 22 February 2011 Christchurch earthquake, the 6 June 2011 aftershock, and the 23 December 2011 New Brighton aftershock sequence. The focus of this thesis is on the Darfield and Christchurch events. The fault ruptures are described by Beaven et al. (2012) as a rupturing of intact rock rather than a smoother rupture along a well developed plate boundary, since the fault surfaces have been immobile for a long period of time, which is characteristic of an intraplate setting. The earthquake sequence is related to coexisting strike-slip and thrust activity on an evolving thrust system (Campbell et al., 2012) in the upper crust. The earthquakes occurred along previously unknown faults. The first two larger earthquakes of the sequence involved rupturing of the Greendale Fault and Port Hills Fault (Figure 1-2).

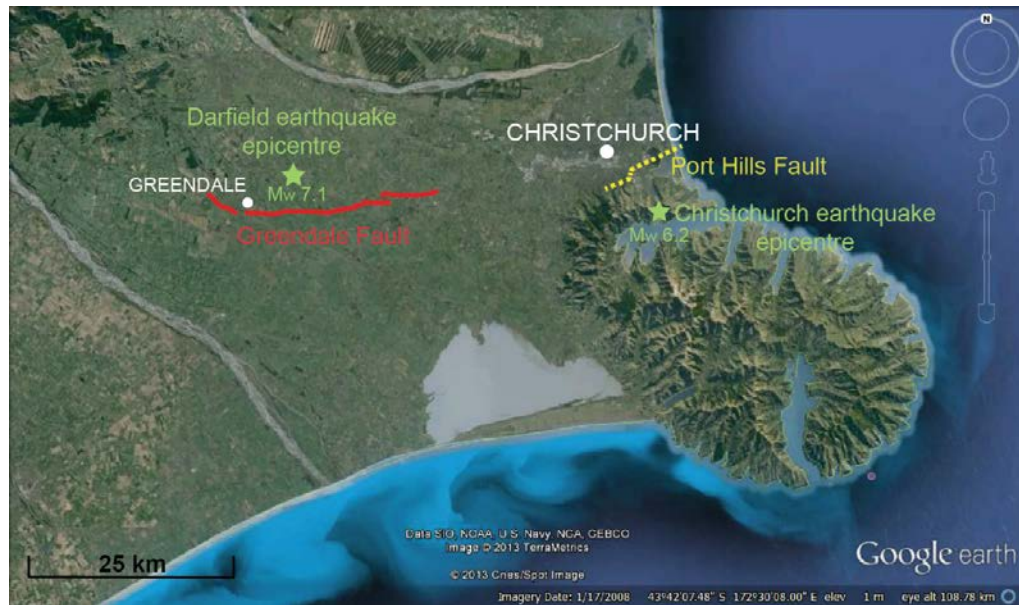


Figure 1-2. Map showing fault trace of the Greendale Fault (in red) which ruptured the surface on 4 September 2011 during the Darfield earthquake. The Port Hills Fault (in dashed yellow) is the surface projected fault location based on GPS and DInSAR data from Beaven et al. (2012). Event epicentres are green stars. Google earth V 7.0.3.8542. (17 Jan 2013) New Zealand. 43°42'07.48"S, 172°30'08.00"E, Eye alt 108.78 km. SIO, NOAA, U.S. Navy, NGA, GEBCO. Cnes/Spot Image 2013. <http://www.earth.google.com> [May 30, 2013].

1.3.1 The 4 September 2010 Darfield Earthquake

The 7.1 moment magnitude (Mw) Darfield earthquake initiated 11 km below the Canterbury Plains in a low relief rural farming area, with an epicenter approximately 6 km southeast from the town of Darfield on a previously unknown fault system (Sibson et al., 2012). Multiple fault planes ruptured, with the Greendale Fault undergoing most of the earthquake's moment release and caused rupturing of the ground surface (Beaven et al., 2010; Beaven et al., 2012). The Greendale Fault rupture was triggered a few kilometers to the north of the main rupture by the NE trending blind Charing Cross Fault, an Mw 6.3 event on a steeply dipping reverse fault segment (Beaven et al., 2010; Gledhill et al., 2011). The Greendale Fault ruptured in both the east and west directions and the

rupturing occurred over approximately 10 seconds, followed 17 seconds later by a third fault rupture at the western end of the Greendale Fault near Horotata, a Mw 5.7 event with a reverse right lateral component mechanism (Holden et al., 2011). An image of part of the Greendale Fault is shown in Figure 1-3.



Figure 1-3. Aerial photograph of the E-W trending Greendale Fault. A drainage canal is displaced by shear fractures along the fault surface. Image taken by Richard Jongens of GNS science.

The complex Greendale Fault rupture is the main source of the rupture sequence (Holden et al., 2011), and is generally described by three fault segments: the main E-W trending dextral strike-slip fault rupture, a fault segment to the west of the main rupture trending NW, and an offset right-lateral fault segment trending NE to the east of the main rupture (Beaven et al., 2010). Deformation features including left step-overs are observed

with associated push up structures (Villamore et al., 2012) with an average strike of 085° for the left-stepping fault traces (Sibson et al., 2012).

The mainly dextral strike-slip surface rupture extends east-west for approximately 30 km (Quigley et al., 2010). Measured displacement and deformation includes approximately up to 5 m of predominantly dextral displacement (2.5 m average displacement), vertical displacement at fault bends was measured at 1 – 1.5 m, and a 30 – 300 m wide deformation zone exists perpendicular to the strike of the fault (Holden et al., 2011; Van Dissen et al., 2011). Ground displacement to the north of the Greendale Fault is generally eastward, with uplift to the south of the fault (Beaven et al., 2010). More ground deformation is present on the western end of the fault (Campbell et al., 2012). The surface deformation from the Darfield earthquake is complex. Van Dissen et al. (2011) describe the fault structures in areas of maximum deformation as “E-SE striking Riedel fractures with right-lateral displacements, SE striking extensional fractures, S-SE to S striking Riedel fractures with left-lateral displacements, NE striking thrusts, horizontal dextral flexure, and decimeter-amplitude vertical flexure and bulging.” An image of fault step-overs and bulging is shown in Figure 1-4.

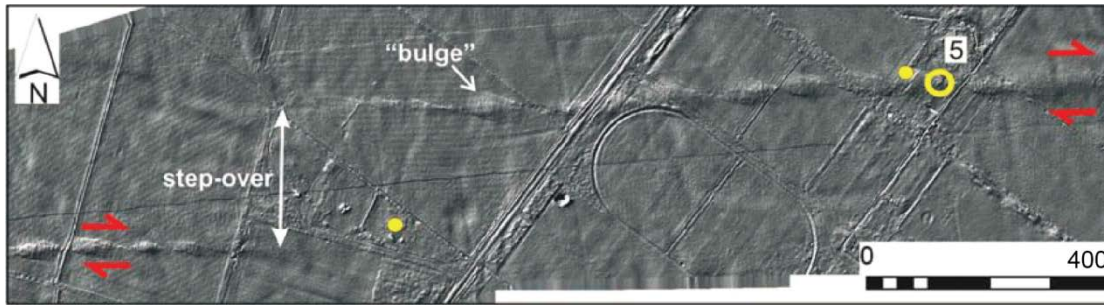


Figure 1-4. LiDAR hillshade DEM along the Greendale Fault demonstrating a left stepping en echelon rupture. Fault step-over and bulges are indicated. Red arrows indicate lateral displacement. Yellow circles denote damaged buildings. Image adapted from Van Dissen et al. (2011).

The Darfield earthquake caused significant damage to buildings near the fault rupture, and also to many older buildings in Christchurch, mostly as a result of differential settlement of foundations due to liquefaction and lateral spreading (Gledhill et al., 2011). Over 5000 aftershocks were measured seven months following the Darfield earthquake, most with focal depths less than 15 km (Sibson et al., 2012).

1.3.2 The 22 February 2011 Christchurch Earthquake

Following the Darfield earthquake, right lateral deformation occurred to the east of the Greendale Fault (Beaven et al., 2012) causing a change in the crustal stress regime near Christchurch. On 22 February 2011, a 6.2 Mw earthquake occurred with an epicenter approximately 6 km SE of Christchurch city center on a previously unknown fault with multiple fault plane ruptures (Bannister and Gledhill, 2012). A surface rupture did not occur, but uplift occurred to the south of the surface projection of a fault, now known as the Port Hills Fault, resulting in extensive damage and loss of life. The earthquake focus was at a depth of approximately 4 km, and was initially modelled on a planar fault striking NE-SW at approximately 59° and dipping 69° SE with a mixture of

right-lateral and reverse slip (Beaven et al. 2011). Beaven et al. (2011) later provided a two-fault model with slip on two sub-parallel fault planes to provide a better fit to the geodetic source data. Beaven et al. (2012) again further updated the model to three fault segments with oblique-reverse/right-lateral slip on the eastern fault section, right-lateral slip on the western fault section, and pure reverse faulting on the NNE-trending cross fault. Maximum slip is determined to be 2.5-3 m for the geodetic model.

1.3.3 Aftershocks

After the Darfield and Christchurch earthquakes, there still remained a continuation of complex aftershocks. As of May 2013, over 11850 earthquakes have been recorded in the last year in the Canterbury region, with 13 events having Mw 4 to 5 (GeoNet, 2013). A region identified between the Darfield and Christchurch epicentres is identified where significant moment release has not occurred, and may possibly fail in the near future (Beaven et al., 2012).

1.4 Thesis objectives

The main goals of this thesis were a seismic study of active faults using newly acquired 2D seismic reflection data from the Canterbury Plains and within the city of Christchurch, following the 2011 Christchurch earthquake. Three different approaches were undertaken, each with their own distinct objectives.

1. The first approach was seismic interpretation of the newly acquired data with the following objectives:

- Provide a review of the tectonic and geologic background of New Zealand with a focus on the Canterbury Plains, in order to complement seismic interpretation of the region.
 - Interpretation of the 2D seismic reflection data in the city of Christchurch and the Canterbury Plains by delineating local stratigraphy and mapping fault systems for seismic risk hazard assessment.
2. The second approach focused on the near surface (top 50 m), using the multi-channel analysis of surface waves (MASW) method to generate shear wave velocity profiles. Shear wave velocity studies are important in geotechnical and environmental investigations where the stiffness of soils can be evaluated, an important characterization in liquefaction potential. The specific objectives were:
- Use 2D seismic reflection data previously acquired for mapping unknown faults, and apply the MASW seismic method at two distinct locations near active fault zones.
 - Investigate seismic velocities at liquefied sites by evaluating S-wave velocity profiles as determined by the MASW seismic method for site characterization.

- Use shear-wave velocity to identify stiffness properties of the near surface, which is an important soil parameter in liquefaction assessment in earthquake studies.

It is important to bear in mind that ‘liquefaction potential’ cannot be directly measured, only various parameters that control a soil’s tendency to liquefy can be measured (Glaser, 1995).

3. The third approach was established out of interest to create a physical model of a fault rupturing the surface with a deformed fault zone. The seismic data were acquired at the University of Calgary Seismic Physical modeling Facility which is maintained by the Consortium for Research in Elastic Wave Exploration Seismology (CREWES). The objectives were to:

- Create several physical model prototypes of a simple vertical fault which ruptures a geologic surface.
- Process and image a fault deformation zone using 2D seismic techniques, and investigate fault detection.
- Compare the physical modeling results to seismic field data acquired traversing the surface ruptured Greendale Fault in New Zealand.

1.5 Contribution of the thesis

Hidden fault structures have been suspected in the Canterbury Plains (Pettinga et al., 2001); however the region has been largely unstudied with very little well control and a lack of seismic data. This thesis contributes to constraining seismic hazard and risk assessment by identifying the presence of faults beneath the central Canterbury plains and within the city of Christchurch in newly acquired 2D seismic profiles. In addition, the MASW method is used to investigate the shallow surface by generating S-wave velocity profiles. Lower S-wave velocities may be indicative of reduced soil rigidity, a contributor to geological hazards such as liquefaction following an earthquake. Fault zone research is further extended in this thesis by seismic physical modeling, where physical models are constructed and seismic data is acquired in a scaled environment and processed. Physical modeling demonstrates a method to test seismic acquisition parameters for detecting faults, and the final imaging results are comparable to a recent field survey across an active fault zone in New Zealand.

1.6 Thesis outline

A tectonic and geologic overview of the study area, and seismic interpretation of the 2D seismic reflection data from the Canterbury Plains and the city of Christchurch is given in Chapter 2.

In Chapter 3, the theoretical background and methodology of the MASW method is reviewed. Data processing to enhance surface waves on raw shot gathers and the results of the shear wave velocity profiles are discussed.

Physical modeling of a fault zone is presented in Chapter 4. A general background on physical modeling and seismic resolution is reviewed. The challenges of constructing physical models are discussed, in addition to a discussion of acquisition and processing of the physical modeling data. Event identification by raytracing and a comparison of the physical modeling data to field data acquired in New Zealand is included.

Chapter 5 summarizes the research of this thesis, and offers recommendations for future work.

1.7 Datasets and software used

The 2D seismic reflection data used for interpretation was processed by Sensor Geophysical Ltd. in Calgary, Alberta. Final processed 2D post-stack migrated seismic sections were used for interpretation using the IHS Kingdom® Suite Interpretation Package.

Raw shot gathers of the 2D seismic reflection data were processed to enhance surface waves in the ProMAX software package, to prepare the seismic data for surface wave analysis in SurfSeis® 3.15, developed at the Kansas Geological Survey.

Physical modeling seismic data was initially viewed in SeiSee 2.16.1 for quality control, and then processed in GEDCO's VISTA® 11.0 seismic data processing software.

Google EarthTM 7.0.3.8542 was used to generate numerous maps in this thesis.

Adobe® Illustrator® CS6 and Microsoft® PowerPoint® were used to construct and edit figures.

Chapter Two: **SEISMIC INTERPRETATION OF THE CANTERBURY PLAINS, NEW ZEALAND**

2.1 Introduction

New Zealand is a region of active earthquake activity and is structurally complex. The active oblique convergent Australian-Pacific plate boundary zone underlies New Zealand from the northeast to the southwest. The Pacific plate subducts beneath the Australian plate along the east coast of the North Island, the Australian plate subducts under the Pacific plate south of the South Island, and an oblique transform fault system occurs in between. The converging plate boundary on the South Island of New Zealand has resulted in compressional deformation and rapid uplift of the Southern Alps. Since the last glacial period during the Late Quaternary, the Canterbury Plains have been buried by eroded greywacke sediments transported in eastbound rivers from the Southern Alps by glaciations and fluvial outwash (Wilson, 1985). This thick layer of quaternary unconsolidated sediment blankets geologic structure, including hidden faults which were activated during the 2010-2011 Canterbury earthquake sequence.

2.2 Tectonic and geologic overview

A review of the tectonic history of New Zealand with a focus of the South Island and Canterbury Region is given to provide a general understanding of the current plate boundaries. An overview of the geologic stratigraphy of the Canterbury Plains is presented to support interpretation of seismic data analysis and observed geophysical trends. A geologic time scale is provided in Appendix A.

2.2.1 The tectonic history of New Zealand

New Zealand was once part of the eastern Pacific margin of Gondwana and formed part of the Australia and Antarctic sectors of the Pacific-facing margin up until the Cretaceous period (Laird and Bradshaw, 2004). The history of Gondwana is summarized by Teichert (1959) as an idea originating and developing in the late nineteenth century. It was proposed that a large Indo-Oceanic super continent existed from early Permian time to the end of the Miocene. Gondwana is believed to have included the area of eastern South America, the southern Atlantic Ocean, central and southern Africa, the Indian Ocean, Peninsular India, Australia, and Antarctica (Molnar et al., 1975). The foundations of New Zealand were built during Paleozoic and Mesozoic sediment accretion processes, as a result of the Permian oceanic crust subducting beneath the eastern Gondwana margin (Cox and Sutherland, 2007).

Approximately 81 million years ago during the Late Cretaceous, the continent of Zealandia which includes New Zealand, the Campbell Plateau, and the Chatham rise, began to separate from Gondwana by rifting and sea floor spreading, and drifted to its current position by the opening of the Tasman Sea (Molnar et al., 1975). Cretaceous extension following rifting led to east and northeast trending normal faults at the Gondwana margin, and are mapped in the basement of the Chatham Rise and to the west in Canterbury region (Field et al., 1989). Seafloor spreading ended during the early Eocene (Cox and Sutherland, 2007). Following separation from Gondwana, Zealandia is regarded as a mostly submerged micro-continent with only ten percent of the continental

crust emerged above sea level (Mortimer, 2004), exposing the North and South Islands of New Zealand.

Submergence of Zealandia during the Late Cretaceous to the Oligocene is associated with marine transgression and coal and clastic dominated deposition. Carbonate-dominated deposition then occurred at maximum submergence during the Oligocene to early Miocene through most of New Zealand, however, this occurred earlier in eastern areas such as the Canterbury Basin (Jongens et al., 1999; King, 2000;).

Tectonic plate motion reconstructions of the Late Eocene - early Oligocene (about 38 Ma) correspond with development of the Australian-Pacific plate boundary similar to present day (Molnar, 1975; King, 2000). The initiation of the Alpine fault on the South Island is debated (Cooper et al., 1987); however there is general agreement that the fault was first established during the Late Oligocene or Early Miocene (Cox and Sutherland, 2007; King, 2000) and became an active transform around 25 Ma (Norris et al., 1990, and references therein). Correspondingly, during the early Miocene in the last 24-30 Ma, the Pacific Plate began to subduct beneath the Australian plate along the Hikurangi Margin (Nichol et al., 2007). Intraplate volcanism followed in the mid to Late Miocene with three main active volcanoes on the South Island between 11 and 5.8 Ma: Lyttelton, Akaroa, and the Mt. Hebert Volcanic Groups (Hampton and Cole, 2009).

Marine regression, as well as uplift and erosion at convergent margins during the Pliocene-Pleistocene contributed to significant volume of coarse clastic sediment

deposited throughout New Zealand basins (King, 2000). Glacial deposits and alluvial gravels dominated sedimentary deposition during the Quaternary period. Up until the present, continuing compression, uplift, and erosion of the Southern Alps contribute to sedimentation around the South Island, and plate boundary deformation zone continues to increase (Forsyth et al., 2008).

2.2.2 The current tectonic setting of New Zealand

The active oblique convergent Australian-Pacific plate boundary crosses New Zealand from the northeast to the southwest, with the North Island of New Zealand on the continental Australian Plate, and most of the South Island on the continental Pacific plate. A simplified image of the tectonic setting and plate boundaries is shown in Figure 2-1. The Hikurangi subduction system off the East Coast of the North Island dips westward subducting the Pacific plate under the Australian Plate, while the Puysegur subduction system southwest of the South Island dips eastward subducting the Australian plate under the Pacific plate (Davey et al., 1998). The oblique plate motion can be viewed as the vector sum of parallel and perpendicular movement along the plate boundary. The southwest motion of the Pacific plate relative to the Australian plate decreases from > 40 mm/yr northeast of the north island to approximately 30 mm/yr in the south (Townend et al., 2012).

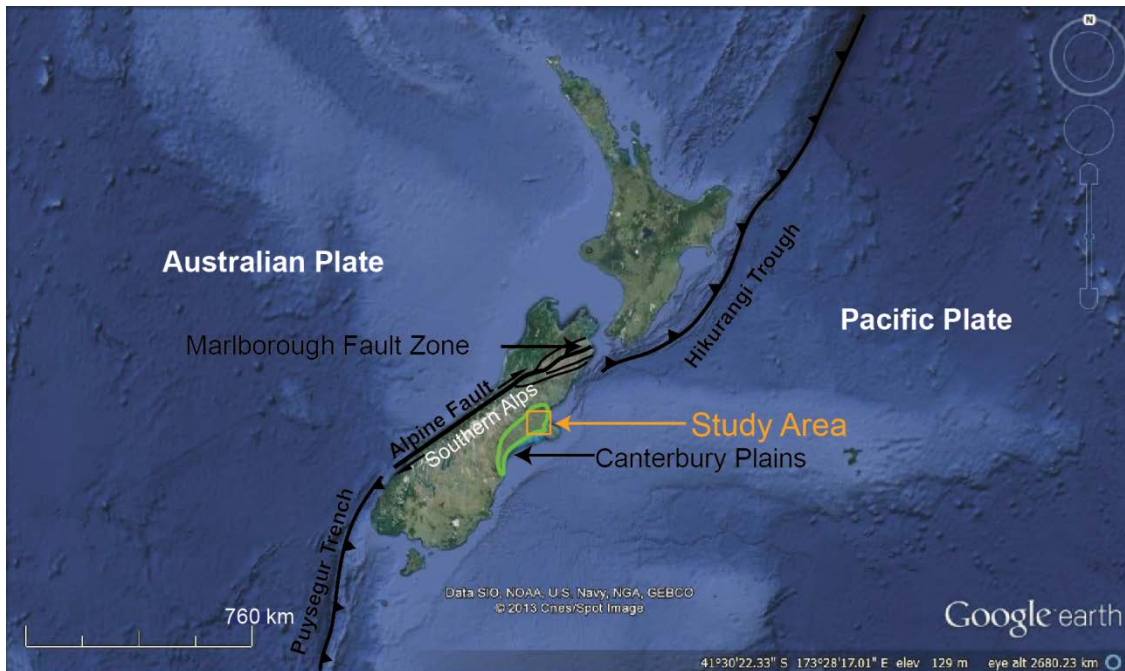


Figure 2-1. The tectonic setting of New Zealand, simplified. Google earth V 7.0.3.8542. (2013) New Zealand. 41°30'22.33"S, 173°28'17.01"E, Eye alt 2680.23 km. SIO, NOAA, U.S. Navy, NGA, GEBCO. Cnes/Spot Image 2013. <http://www.earth.google.com> [May 30, 2013].

At the Hikurangi subduction zone, the overriding Australian plate is deformed by a 480 km wide zone and is accompanied by strike-slip faulting throughout the central North Island (Nichol and Beaven, 2003). However, most of the convergent component of relative plate motion occurs on the Hikurangi subduction thrust, where there exists major thrust faults in the upper plate (Wallace et al., 2009). The Pacific Plate subducts beneath the Hikurangi trough at a rate of 5-6 cm/year (Campbell et al., 2012a). A shift in the plate motion mechanics then occurs in the northern South Island from oblique subduction to oblique transpression (Townend et al., 2012) with upper plate deformation and tectonics dominated by the strike-slip faults of the Marlborough Fault Zone at the northern end of the South Island (Eberhart-Phillips and Bannister, 2010). Large

subduction thrusts are not expected beneath Marlborough and North Canterbury, as the subduction boundary is believed to be permanently locked (Reyners, 1998). Further southwest, oblique continental collision dominates most of the central South Island by means of the active Alpine Fault, where the Marlborough Fault Zone branches off. The Alpine Fault, with 480 km of right lateral slip since the Jurassic, delineates a transform boundary between the active Australian-Pacific plates (Norris et al., 1990). The compressional deformation through the central South Island has created rapid uplift of the Southern Alps mountain range through the central South Island to the east of the Alpine Fault (Kleffmann et al., 1998, Smith et al., 1995). Southwest and offshore of the South Island, the Australian plate subducts eastward below the Pacific plate along the Puysegur subduction zone, where a thrust faulted regime dominates (LaMarche and Lebrun, 2010; Townend et al., 2012).

2.2.3 The tectonic setting of the Canterbury Region, South Island

The Canterbury Region resides in an area of active earth deformation, as a result of oblique continental collision of the Australian and Pacific plates along the Alpine Fault to the west of the region (Stirling et al., 2001). At approximately the same latitude as Christchurch, the Australia-Pacific plate boundary motion is predicted to be 39 mm/yr at 43.5 °S at a bearing of N71 °E, along the N55 °E trending Alpine Fault (DeMets et al., 1990, p. 446). The oblique convergence slip estimates are approximately 35.5 mm/year parallel to the fault and 10 mm/year perpendicular to it, resulting in a transpressional zone boundary with strike-slip and dip-slip components (Norris and Cooper, 2001). The

regional maximum compressive stress field (σ_1) is horizontal and is estimated to trend approximately 115° in the Canterbury Plains (Sibson et al., 2012).

For the most part, the Alpine Fault is an east-dipping oblique shear, projecting and flattening beneath west Canterbury where the crustal interface thins (Pettinga et al., 2001, Kleffman et al., 1998). The majority of plate boundary deformation is accommodated by the Alpine Fault; however 25% of the plate motion ($\pm 15\%$ uncertainty) is divided among other structures across the 150-200 km wide Southern Alps into the Canterbury Region (Norris and Cooper, 2001; Jongens et al., 1999). The active tectonics of the continent-to-continent collision have the potential to activate existing buried faults in the Canterbury Plains (Campbell et al., 2012a). The rate of deformation of the Pacific Plate begins to subside from the Southern Alps towards the southeast in central and south Canterbury (Pettinga et al., 2001).

The upper crustal structure of the northern Canterbury Region is dominated by north and northeast trending faults and folds formed to accommodate plate motion between the Hikurangi Trench and the Alpine Fault, whereas the central and south Canterbury region is dominated by north trending active structures as a response to deformation from continent collision of the Southern Alps (Pettinga et al., 2001). The structures of the Canterbury Region are grouped by Pettinga et al. (2001) into structural domains (Figure 2-2). The focus area of this thesis is within Domain 7 in the Canterbury Plains Zone, which is generally described as a hidden and unstudied fault zone. Thrust and strike-slip faults are thought to have initiated in the foothills of western Canterbury,

and spread with time into the plains as deformation expanded to the south and east (Campbell et al., 2012b).

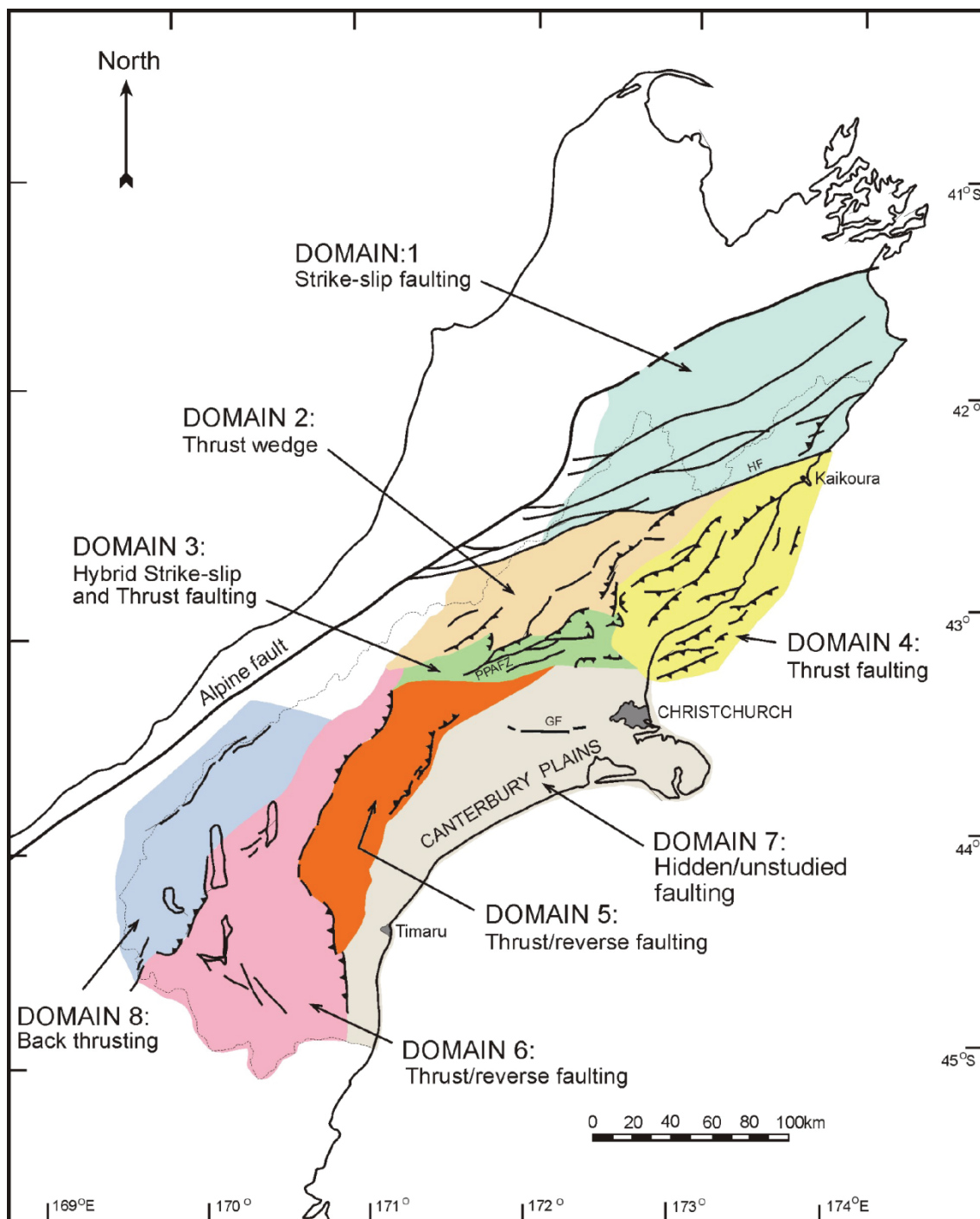


Figure 2-2. Structural domain map of New Zealand's South Island and the Canterbury Region from Pettinga et al. (2001). The focus of this research is located in Domain 7, where hidden faults are present. The Greendale Fault, which ruptured during the 4 September 2010 earthquake is marked as 'GF' within the boundary of the Canterbury Plains.

2.2.4 Geologic setting and stratigraphy of the Canterbury Plains

2.2.4.1 Permian to Early Cretaceous basement

The basement rocks which form the foundation of the South Island in New Zealand are divided by the Median Tectonic Zone into a Western province, and an Eastern province which is also known as the New Zealand geosyncline (Landis and Coombs, 1967). Figure 2-3 shows a geologic map of the basement rocks on the South Island of New Zealand. The older Western province is composed of Paleozoic sedimentary rocks and various crystalline rocks of late Precambrian to Cretaceous age (MacKinnon, 1983). The younger Eastern province is composed of a collection of terranes which include a belt of clastic rock which belong to the Torlesse Composite Terrane (Mortimer, 2004) and underlie the Canterbury region. Terranes are defined as “fault-bounded slices of regional scale, each with their own distinctive geologic history” (Wandres and Bradshaw, 2005) and are divided by provenance, structural styles, lithologies, and low-grade metamorphic changes (Beetham and Waters, 1985). In many cases, the faults separating terrane boundaries in a suture zone are obscure (Howell et al., 1985).

The Torlesse rocks are fragments shed from continental margin basins, and are primarily quartzofeldspathic greywacke and gray-to-black mudstone (MacKinnon, 1983; Howell et al., 1985). The Torlesse is divided by the Esk-Head Melange into two sub-terrane which become younger eastward; The Permian-Triassic older Torlesse (Rakaia) which underlies most of the Southern Alps and eastern foothills of the Canterbury Plains, and the Late Jurassic-Early Cretaceous younger Torlesse (Pahau) in northeast Canterbury

(Bishop et al., 1985, Wandres et al., 2004). The regional trend of the Mesozoic Torlesse terrane elongated boundaries reflect the northwest orientation of the Mesozoic Gondwana margin (Bradshaw et al., 1996; Cox and Sutherland, 2007). A structural basement high extends northwest from Banks Peninsula into the Canterbury Plains (Hicks, 1989).

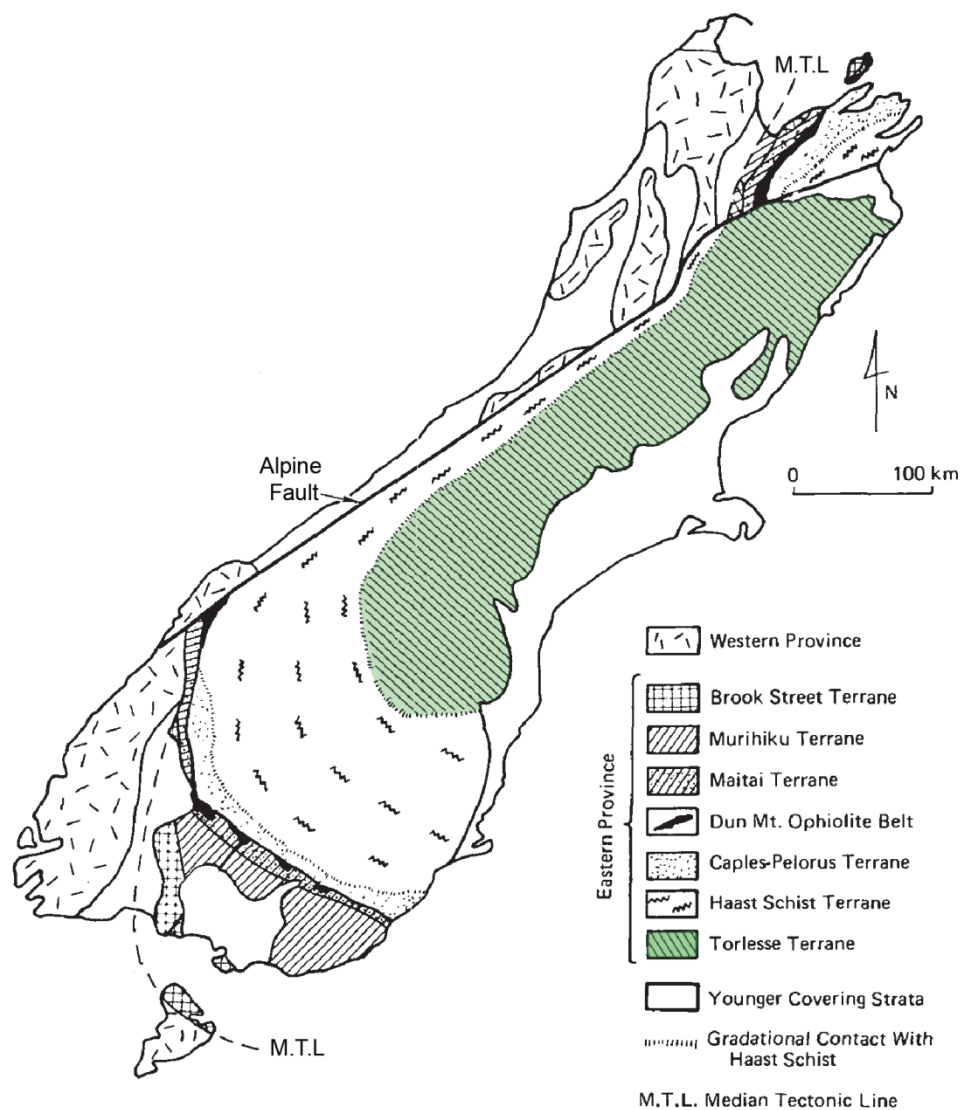


Figure 2-3. Geologic map of basement rocks on the South Island of New Zealand. Adapted from MacKinnon [1983]. The Torlesse terrane, part of the Eastern province is highlighted in green.

2.2.4.2 Late Cretaceous to Pleistocene volcanic and sedimentary rocks

This section provides a stratigraphic summary of southwest Canterbury in the Malvern Hills, Burnt Hill, and Oxford areas, and is based on Forsyth et al. (2008) and references therein. A stratigraphic chart listing geologic successions since the Early Cretaceous is shown in Figure 2-4. The central Canterbury region is characterized by a 1 - 2 km thick blanket of sedimentary and minor volcanic rocks of late Cretaceous to Cenozoic age overlying the greywacke basement (Browne et al., 2012). The sediment thickness is relatively constant between Banks Peninsula and the foothills of the Southern Alps.

The Mt. Somers Volcanic group erupted during late Cretaceous (89 ± 2 Ma) rifting and extension, and contains sequences of lavas, ignimbrites, and tuffs up to 1 km thick which unconformably overlay the eroded Torlesse rocks (Barley, 1987). West of Darfield in the Malvern Hills area (Figure 1-1), the middle late Cretaceous Monro conglomerate overlies the Mt. Somers volcanic group and older Torlesse rocks and is interpreted as a localised fault-angle depression filled with braided-river deposits.

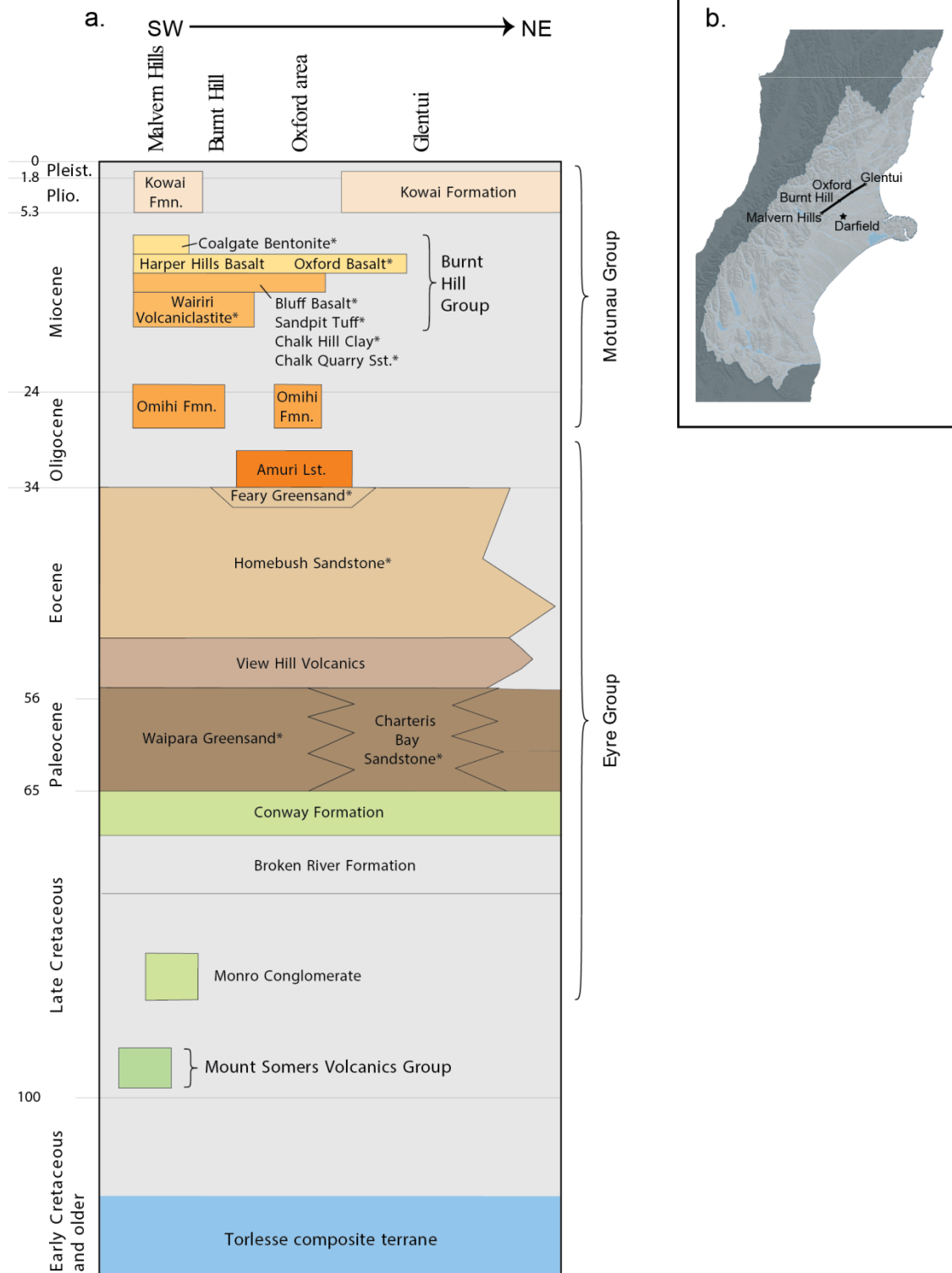


Figure 2-4. (a) Stratigraphic chart of the western Canterbury Plains. Adapted from Forsyth et al. (2008). (b) Map area showing location of (a). Adapted base map provided by Environment Canterbury.

During the latest Cretaceous to early Oligocene, a sedimentary succession of interbedded non-marine and marine sandstone and mudstone in the Eyre group is a result of subsidence in a passive margin setting throughout southwest Canterbury. The Eyre group also consists of the early Eocene intraplate View Hill Volcanics, and the Amuri Limestone found outcropping north of Darfield. Unconformities representing 3 to 10 million year time gaps separate the Eyre Group from the overlying limestone Omihi Formation of the Motunau Group.

The Motunau Group is composed of late Oligocene through early Pleistocene strata and is widespread, yet laterally intermittent sedimentary rock sequence beneath the Canterbury Plains. The Motunau Group also includes the middle to late Miocene Burnt Hill Group, an assembly of volcanoclastic rocks, basaltic flows, and sedimentary rocks. During the late Miocene, intraplate volcanism resulted in the formation of large overlapping stratovolcanoes on Banks Peninsula: Lyttelton to the northwest, and Akaroa in the southeast of the peninsula.

The late Pliocene to early Pleistocene alluvial Kowai Formation caps Motunau Group rocks, and is up to several hundred meters thick in central and northern Canterbury. The weathered greywacke gravel resulted from rapid uplift and erosion of the Southern Alps.

2.2.4.3 Quaternary Sedimentary deposits

Sedimentary deposition during the Quaternary Period in the Canterbury region is dominated by glacial events and thick accumulations of alluvial gravel in structural depressions, including the late Pliocene to early Pleistocene Kowai gravels (Pillans, 1991). A considerable amount of glacial melt water and unconsolidated debris flooded many South Island rivers. The large area of river deposits in the Canterbury Plains consist mostly of unweathered alluvium with well-preserved channel patterns (Forsyth et al., 2008). During the Holocene, windblown fine grained silt (loess) was deposited with thickness of 2 to 4 meters, covering the widespread unconsolidated sediments (Pillans, 1991; Forsyth et al., 2008). Quaternary volcanism does not exist in the Canterbury region.

2.3 Additional information for seismic interpretation

This section provides a record of data available that will support the seismic interpretation. This included petroleum and water wells, previous geophysical work in the area, and also an overview of the earthquake history in the region.

2.3.1 Wells

Exploration wells in the Canterbury Plains are sparse. The Leeston-1 and Arcadia-1 wells are closest to Darfield and the Greendale Fault zone, however they are not near (Figure 2-5). Petroleum development and exploration activity increased during the 1960's in New Zealand when a major gas field was discovered off the North Island Taranaki coast (Katz and Kliever, 1970). The Leeston-1 test well was drilled in 1969 and reached the Mesozoic greywacke basement at just over 1000 m depth. The Leeston-1 well is

located approximately 20 km south from the Greendale Fault. The Arcadia-1 well was drilled in 2000 and is located approximately 20 km north from the Greendale Fault.

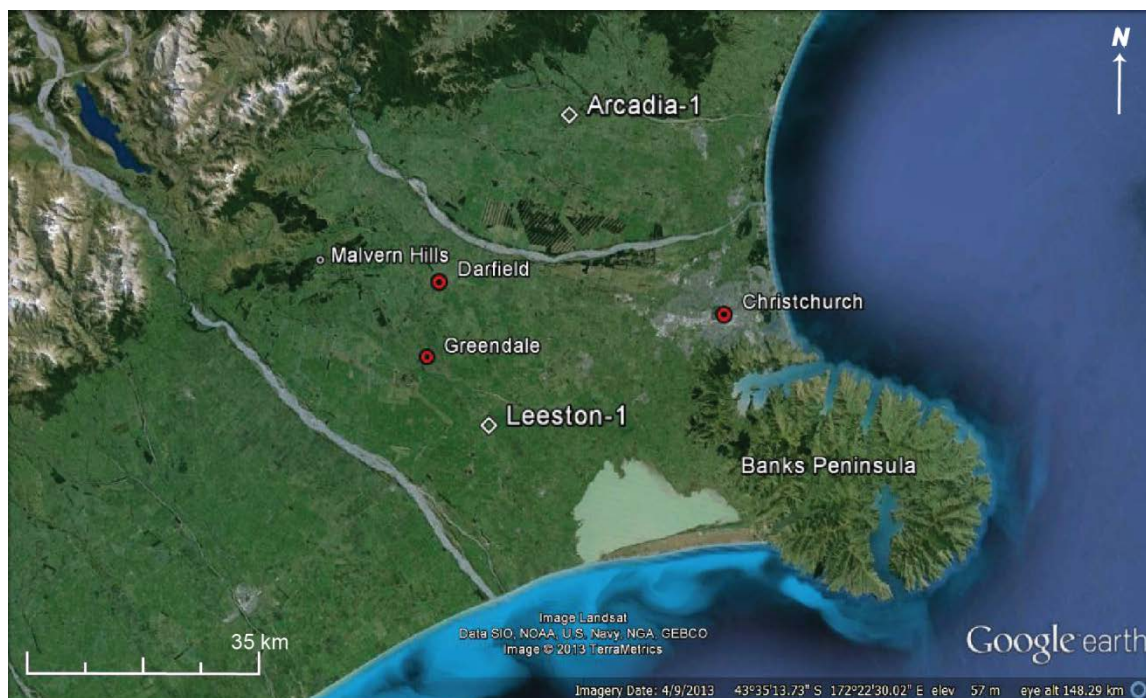


Figure 2-5. Map showing petroleum wells Arcadia-1 (drilled in 2000) and Leeston-1 (drilled in 1969). Google earth V 7.0.3.8542. (4 September 2013) New Zealand. 43°35'13.73"S, 172°22'30.02"E, Eye alt 148.29 km. SIO, NOAA, U.S. Navy, NGA, GEBCO. TerraMetrics 2013. <http://www.earth.google.com> [June 29, 2013].

A 433 m deep Environment Canterbury water well named the Bexley testbore (well no. M35/6038), is used for reference in the seismic interpretation of the Christchurch seismic data, and is located within the city of Christchurch. The Environment Canterbury Bexley testbore log is given in Appendix B.

2.3.2 Previous geophysical work

Geophysical investigations in the Canterbury Plains are limited, especially prior to the 2010-2011 Canterbury earthquake sequence. Most previous research is focused in the

northwest Canterbury Plains near the Malvern Hills. This section summarizes key geophysical investigations during the past fifty years which were considered in this research.

In 1963, a seismic reflection survey consisting of 9 seismic lines totalling 280 km was acquired throughout the Canterbury Plains and is documented in Kirkaldy et al. (1963). Interestingly, Line 8 intersects the present day Greendale Fault surface rupture, however the data is too poor of quality to identify geologic structures. Horizons identified include Quaternary gravels and the geologic basement.

More recently, seismic data has been used to better characterize the Canterbury Plains in terms of potential seismic hazard. Jongens et al. (1999) reported on the structure and stratigraphy of the onshore Canterbury Plains using processed seismic data acquired by Indo-Pacific Energy (NZ) Ltd. The report summarized that basement faults contribute to active deformation in the overlaying strata, and major thrust faults were identified in the seismic lines to the northwest of the study area of this thesis. Finnemore (2004) used integrated geological and geophysical surveys to develop groundwater aquifer models, and characterize sedimentary units and a major fault zone in the northwest Canterbury Plains. The identified fault zone in the study is indicative of geologic structure from the western range front extending below the Canterbury Plains. Dorn et al. (2010) acquired and interpreted shallow seismic data with an aim to study seismogenic structures below the Canterbury Plains northwest of Darfield and the Malvern Hills, nestled against the Foothills of the Southern Alps. The seismic sections in the study provide evidence of

intensely faulted and folded basement and Late Cretaceous-Tertiary layers. Gentle folding was shown to exist in the Quaternary layers and suggest that the structures below the Canterbury Plains have the ability to generate large earthquakes. Shallow seismic and GPR data were recorded just prior to the Canterbury Earthquake Sequence in the NW Canterbury Plains, the data were interpreted and shows interconnected faults and folds underlying an undisturbed surface (Carpentier et al., 2012).

Two recent studies were most beneficial to the research presented in this chapter. An intensive study of marine seismic data was done by Barnes et al. (2011) for the New Zealand Natural Hazards Research Platform, mapping horizons and fault structures beneath Pegasus Bay. The offshore seismic data and interpretations were used as a guide in interpreting the 2D seismic data collected in the city of Christchurch utilized in this research. The study by Jongens et al. (2012), which interprets faulting and folding of structures in seismic data from 1963 BP Shell Todd seismic reflection lines, Indo-Pacific Energy reconnaissance seismic reflection surveys, and existing nearby wells were referenced for interpretation of 2D seismic data acquired in the central Canterbury Plains.

2.3.3 Earthquake history in the Canterbury Region

The Canterbury Plains are fairly quiet in terms of historical seismicity. Pettinga et al. (2001) summarized historical earthquakes in the Canterbury Plains, based on research from the New Zealand National Earthquake Information Database. The most significant historical earthquakes related to this study in the Canterbury region are the 1869 and 1870 Christchurch earthquakes, of approximate magnitude 5 and 5.5 respectively. Further

west into the Canterbury Plains near the Darfield area, there are no records of large earthquakes (Gledhill et al., 2011).

2.4 Seismic Interpretation

2.4.1 Data acquisition and processing

A collaborative effort between the University of Calgary CREWES research group and the University of Canterbury resulted in a 2D reflection seismic data program in April 2011. Seismic data was acquired in the city of Christchurch and the Canterbury area with the goal of mapping blind faults, and interpreting the structure of the Greendale Fault. The 2011 Christchurch seismic acquisition program parameters are given in Hall et al. (2011). A total of 6 seismic reflection lines were acquired; however the interpretation of just three lines will be included in this thesis. The 2D seismic data was processed by Sensor Geophysical Ltd. in Calgary, Alberta. Stacking velocities with underlying stacked seismic data from seismic processing are shown in Appendix C. Final post-stack migrated seismic sections are used for interpretation using the IHS Kingdom® Suite Interpretation Package.

2.4.2 Christchurch seismic data

Two 2D seismic lines were acquired in the city of Christchurch: Line 1 was acquired along the eastern edge of Christchurch down the length of New Brighton Beach, and Line 2 was acquired in Christchurch city center along Barbadoes Street. An overview map of the seismic line locations is shown in Figure 2-6.



Figure 2-6. Overview map showing seismic data acquisition in the city of Christchurch, New Zealand. Line 1 (orange) is along New Brighton Beach, and Line 2 (yellow) is along Barbadoes Street. Google earth V 7.0.3.8542. (25 April 2012) Christchurch, New Zealand. 43°32'06.48"S, 172°40'34.28"E, Eye alt 17.68 km. TerraMetrics 2013. <http://www.earth.google.com> [May 30, 2013].

2.4.2.1 Seismic interpretation of Line 1, New Brighton Beach

The New Brighton Beach seismic line is 8 km long, and spans from stations 101-900 with 10 m shot and receiver spacing. Figure 2-7 shows a map of the seismic line and corresponding stations, with an orange dashed line indicating the projected Port Hills Fault, extended to the surface (based on the slip model derived by GPS and DInSAR data in Beaven et al., 2012). The fault projection shows that the Port Hills Fault can be expected to intersect the seismic line near station 510. Approximately 1 km to the west of the northern portion of the seismic line is the Environment Canterbury Bexley testbore (well no. M35/6038), a 433 m deep testbore. The Bexley testbore is projected orthogonally to the seismic line to intersect it at station 715. Also used to provide

information and considered in the interpretation of the acquired Christchurch seismic data are south trending high resolution marine seismic profiles in Pegasus Bay, parallel with seismic lines ranging from approximately 2 to 25 km to the east of the New Brighton Beach seismic profile (Barnes et al., 2011).

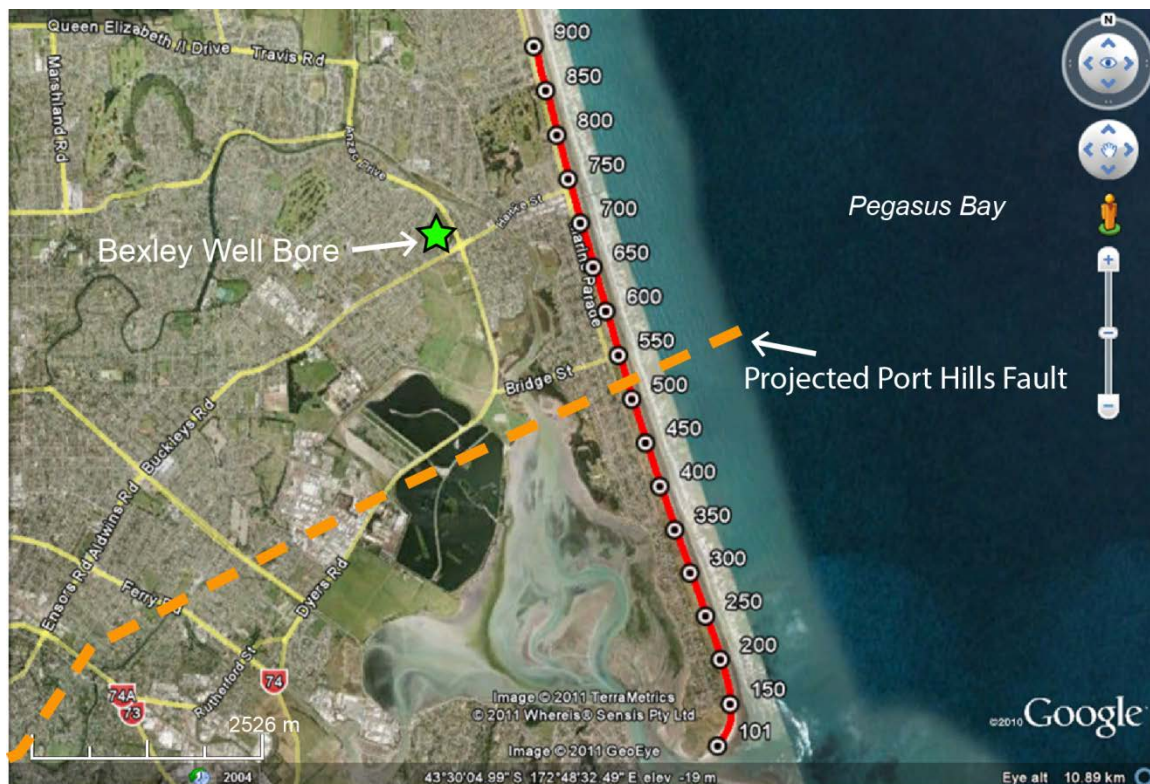


Figure 2-7. New Brighton Beach seismic line with corresponding stations is shown along the east coast of Christchurch. The Environment Canterbury Bexley testbore location is illustrated by the green star. The projection of the Port Hills Fault to the surface is shown by a dashed orange line and is based on GPS and DInSAR data from Beaven et al. (2012). Figure adapted from Hall et al. (2011). Google earth V 6.0.3.2197. (2011) Christchurch, New Zealand. 43°30'04.99\"S, 172°48'32.49\"E, Eye alt 10.89 km. TerraMetrics 2011, Whereis® Sensis Pty Ltd, and Geoeye 2011. <http://www.earth.google.com> [Oct 17, 2011].

The New Brighton Beach seismic profile without and with interpretation is shown in Figures 2-8a and 2-8b respectively. The top of the Late Quaternary Wainoni Gravels is

identified with a green horizon marker near 250 ms (Figure 2-8b). The RMS seismic P-wave velocity in the top 300 ms is approximately 1680 m/s. The Wainoni Gravels were deposited as outwash deposits from glacial periods and has no outcrop, so its lateral extent is uncertain (Brown et al., 1988). The Wainoni gravels present an acoustic impedance contrast from the overlying formations which contain more sand and clay, whereas the Wainoni gravels contain coarser gravel. However, the Wainoni gravels are difficult to distinguish from the continuous sequence of overlying fluvial deposits, even in a wellbore (Brown et al., 1988). The depth to the Wainoni gravels at station 715 is calculated to be approximately 150 m deep, which is in close agreement with the depth to Wainoni gravels formation provided in Brown et al. (1988) and the Bexley testbore. The maximum thickness of the Wainoni gravels are approximately 20 m (Brown et al., 1988).

The Early Pleistocene Top Kowai Formation is identified in the Bexley testbore just below 240 m and also in the Barnes et al. (2011) study. The Top Kowai Formation is interpreted as the yellow horizon marker. The Kowai Formation thins towards the south and Banks Peninsula which consists of large overlapping remnant composite volcanoes (Forsyth et al., 2008), where the Miocene Volcaniclastics are encountered.

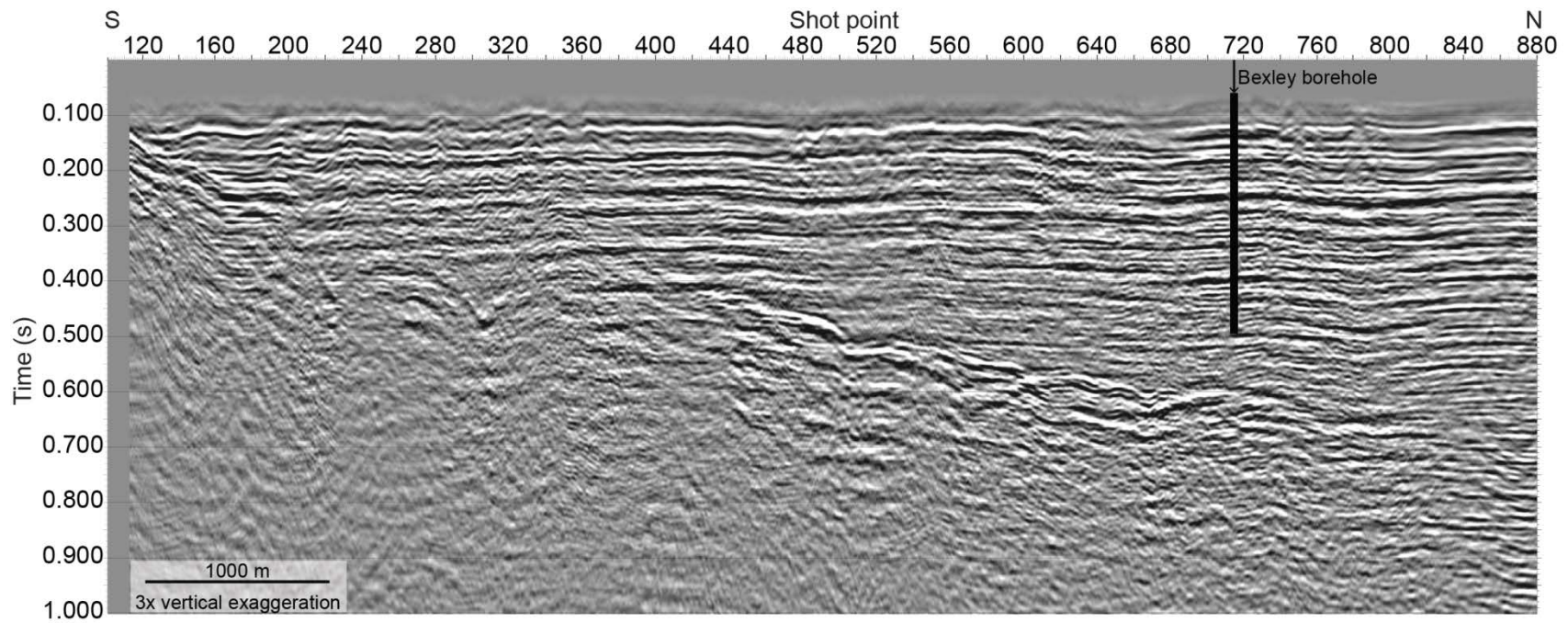


Figure 2-8a. Uninterpreted New Brighton Beach 2D seismic line with 3x vertical exaggeration. The Bexley testbore is 1 km to the west of New Brighton Beach, and the borehole location is projected onto the seismic line.

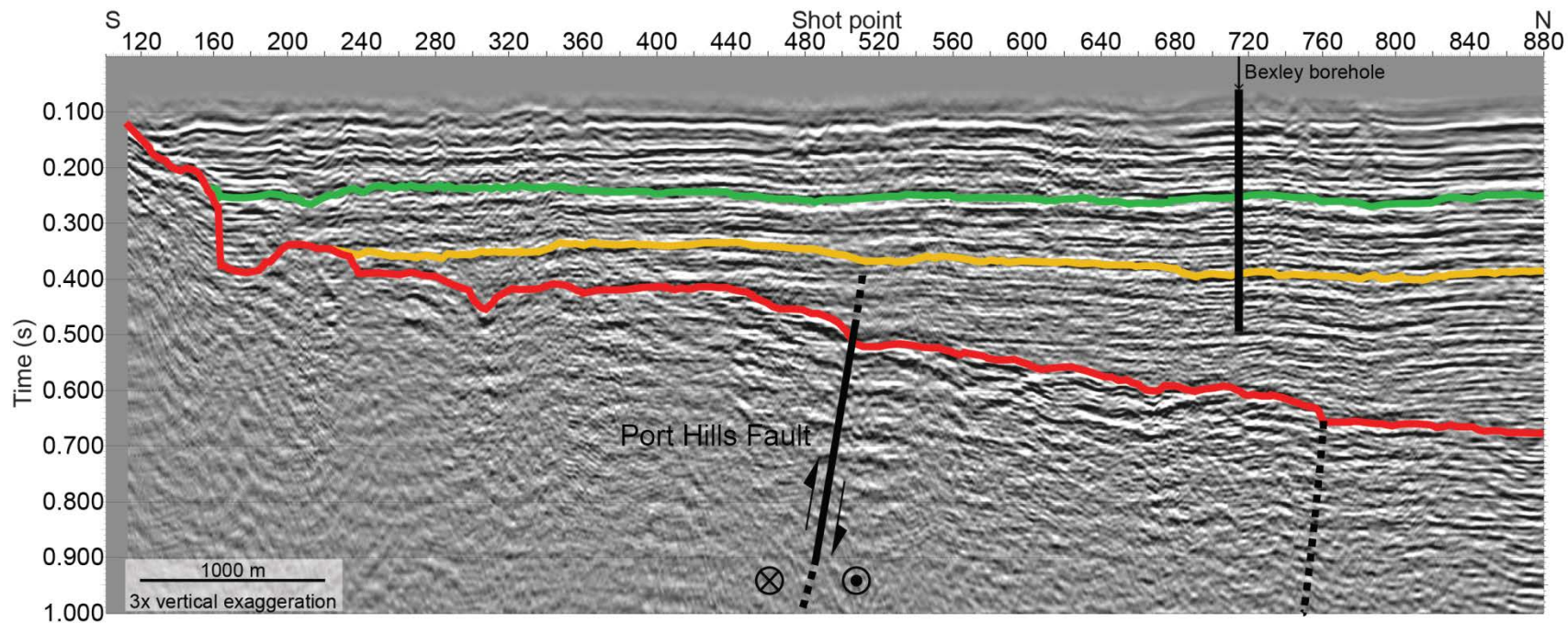


Figure 2-8b. Interpreted New Brighton Beach 2D seismic line with 3x vertical exaggeration. The green horizon represents the Wainoni gravels, the yellow horizon represents the Early Pleistocene Top of Kowai Formation, and the red horizon represents the Miocene Volcaniclastics. The Port Hills Fault is interpreted 400 ms below stations 500-520. An additional projected fault shown in black dashed line towards the north end of the seismic line just intersects the Miocene Volcaniclastics.

The Banks Peninsula Miocene Volcaniclastics (6 to 9 Ma) are interpreted with a red horizon marker along a hummocky reflector, and have a strong and continuous seismic reflector that marks the hydrologic basement (Finnemore, 2004). The Miocene Volcaniclastics outcrop near the southern end of the seismic line along coastal cliffs of Banks Peninsula (Barnes et al., 2011). RMS seismic velocities of the volcanics are approaching approximately 1900 m/s, while the interval velocities are approximately 2700 m/s at station 520. Barnes et al. (2011) show interval velocities of 2500-2700 m/s for the Miocene Volcanics.

The south dipping Port Hills Fault projects approximately 350 m below the ground surface near station 510 (for a velocity of 1800 m/s at 0.44 s). Beaven et al. (2012) modeled maximum slip of 2.5 m at 5-6 km depths in the Christchurch earthquake. The horizon marker for the Miocene Volcanics shows vertical displacement of approximately 27 ms, or 28 m for a material velocity of 2080 m/s. The larger calculated vertical displacement in this study indicates that most of the displacement occurred pre-Upper Miocene. A possible projected fault is also indicated on the northern end of the seismic line below station 760, and just encounters the Miocene Volcaniclastics. Deformation and up-warping of seismic reflections is also seen between stations 700 to 800 near the surface. Most other geologic structure at greater depths in the seismic reflection survey is concealed below the Miocene Volcanics.

2.4.2.2 Seismic interpretation of Line 2, Barbadoes Street

The 3.7 km long Barbadoes Street seismic line (Figure 2-9) was acquired through Christchurch city center and is just less than 8 km west of New Brighton Beach. The line started at the south with a NW trend, then turned north onto Barbadoes Street.

Acquisition parameters are described in Hall et al. (2011). Considering the GPS and DInSAR modelled data (Beaven et al., 2012); the Port Hills Fault is not expected to be seen in this seismic line data.

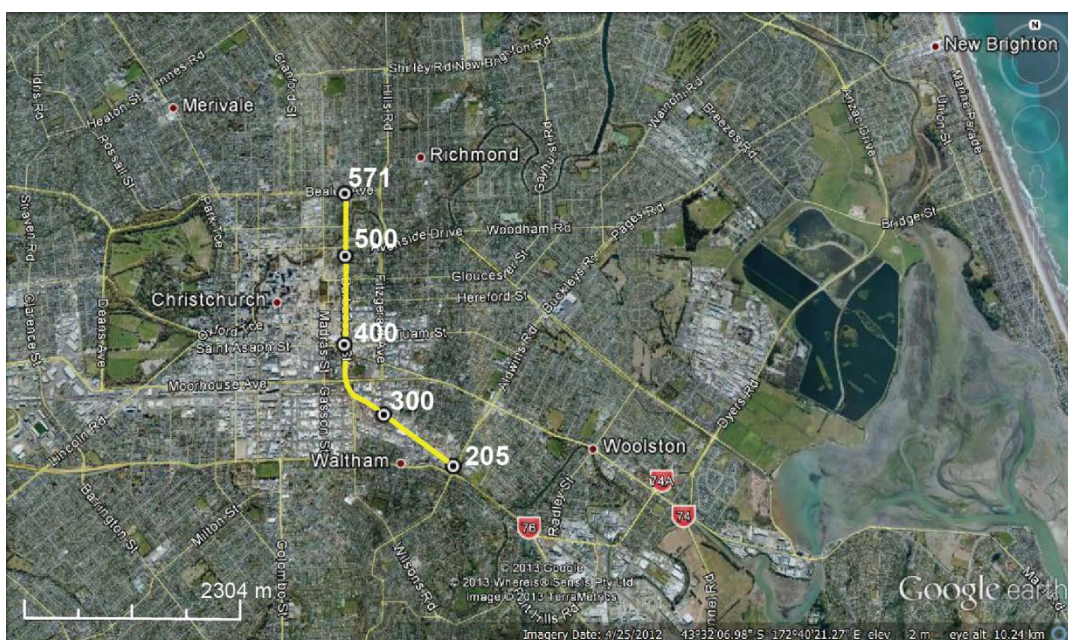


Figure 2-9. Barbadoes Street seismic line (in blue). Started on south end at station 205 and ended north at station 571. Google earth V 7.0.3.8542. (25 April 2012) Christchurch, New Zealand. 43°32'06.98\"S, 172°40'34.27\"E, Eye alt 10.24 km. Whereis® Sensis Pty Ltd. and TerraMetrics 2013. <http://www.earth.google.com> [June 7, 2013].

The Barbadoes Street seismic profile without and with interpretation is shown in Figures 2-10a and 2-10b respectively. The change in line direction occurs at station 360. In the shallow section of the survey, a possible infilled channel is identified in blue. Also,

the disruption in the near-surface between stations 525-545 may indicate a liquefied zone. The top of the Late Quaternary Wainoni Gravels is identified with a green horizon marker slightly above 250 ms at a depth of 165 m (Figure 2-10b). The Top Kowai Formation is interpreted with a yellow horizon marker near 375 ms, and intersects the Miocene Volcaniclastics at the southern portion of the line, indicated by a red horizon marker. Two possible south dipping faults are indicated in the deeper part of the seismic section.

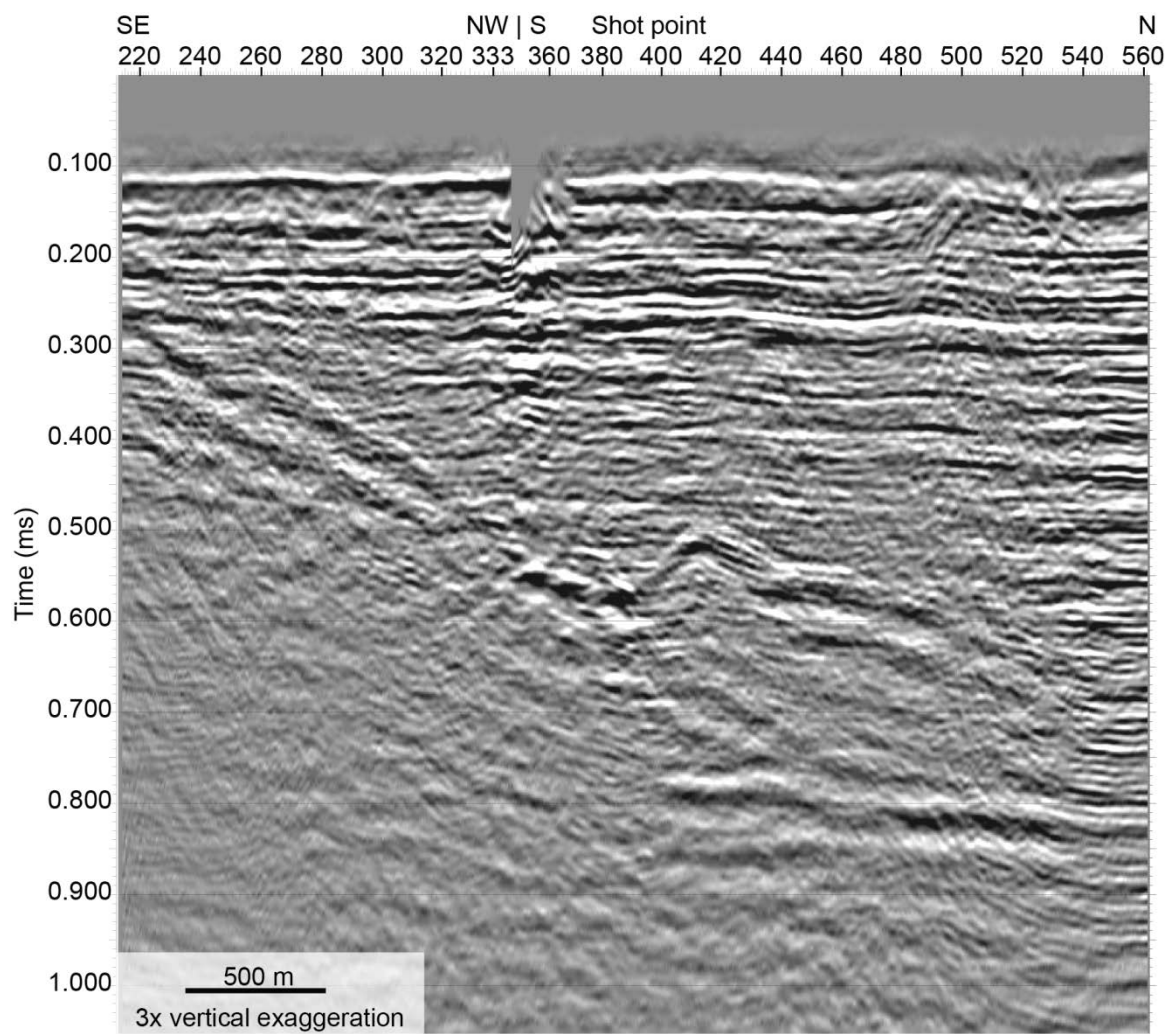


Fig 2-10a. Barbadoes Street seismic profile without interpretation, 3x vertical exaggeration.

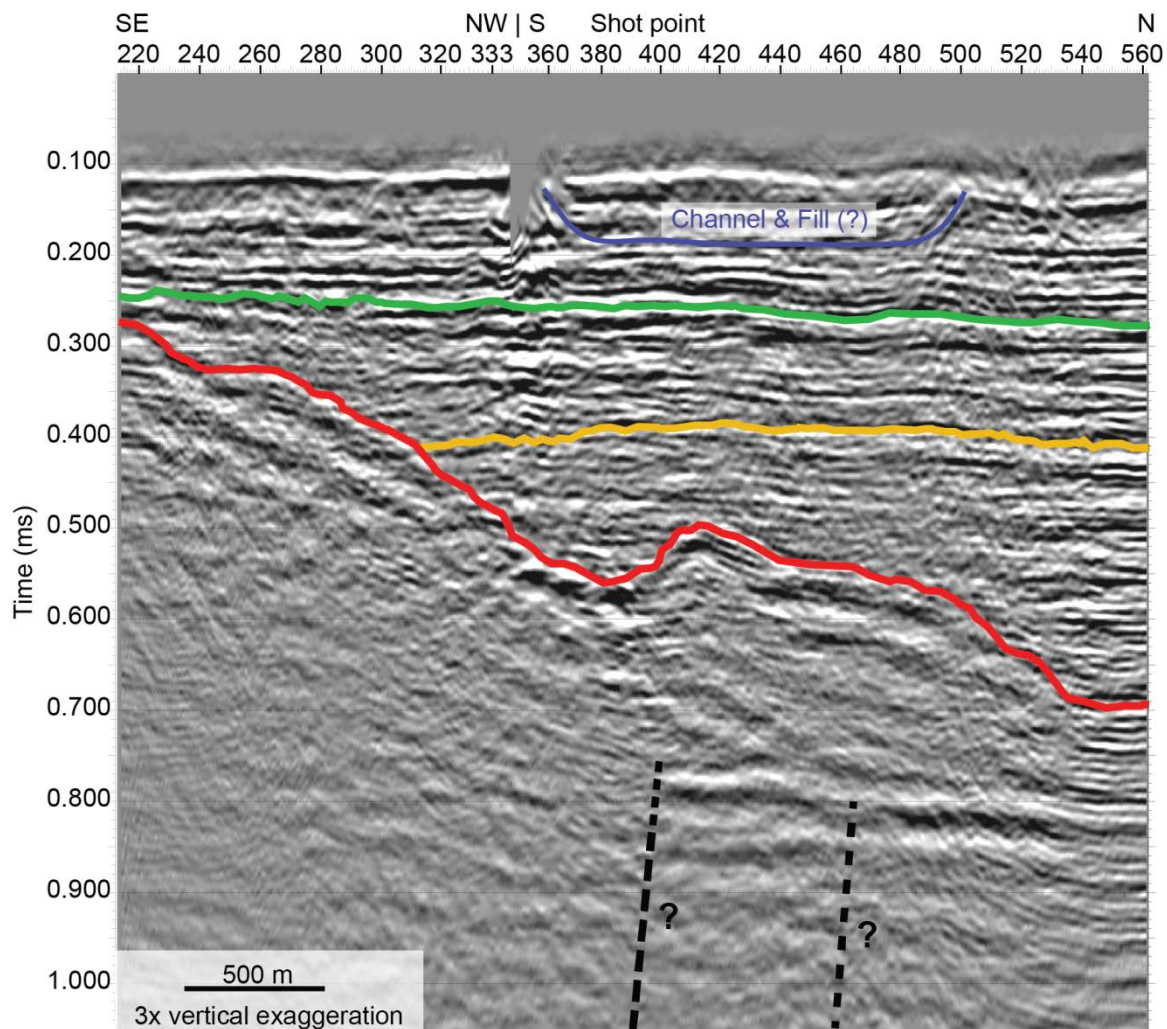


Figure 2-10b. Barbadoes Street seismic profile with interpretation, 3x vertical exaggeration. The green horizon represents the Wainoni gravels, the yellow horizon represents the Early Pleistocene Top of Kowai Formation, and the red horizon represents the Miocene Volcaniclastics. Possible projected faults are indicated in dashed black lines. Also interpreted is a channel and fill zone in the near surface.

2.4.2.4 Seismic interpretation of Line 3, Highfield Road

The Highfield Road seismic line (Figure 2-11) is approximately 35 km west of Christchurch city center, and intersects the EW trending Greendale Fault near station 440. The seismic line acquired on Highfield Road runs from south to north and is 3.4 km long. Data acquisition parameters are summarized in Hall et al. (2011). The fault and fold structures beneath the Canterbury plains to the west of Highfield Road interpreted by Jongens et al. (2012) were considered during the interpretation of this seismic line.

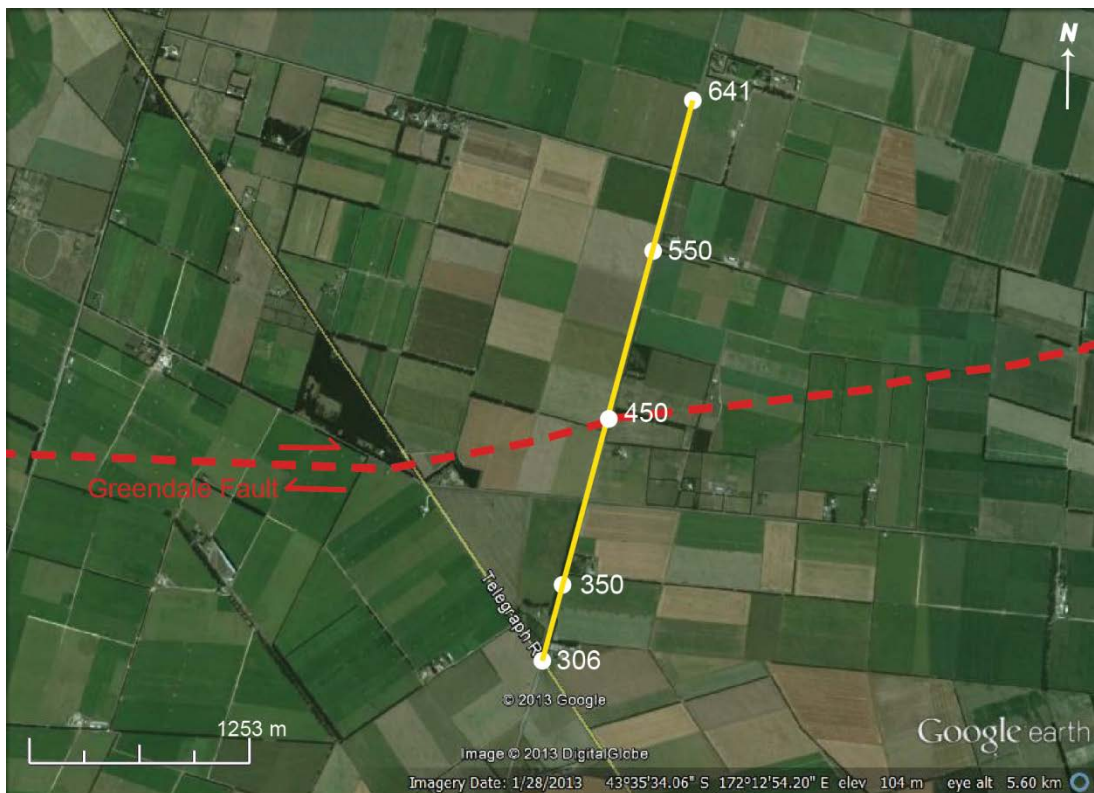


Figure 2-11. Highfield Road seismic line (in yellow). Started on south end at station 306 and ended north at station 641. The Greendale Fault ruptures the surface in an E-W orientation. Greendale Fault trace based on Holden et al. (2011). Google earth V 7.0.3.8542. (28 January 2013) Highfield Road, New Zealand. 43°35'34.06"S, 172°12'54.20"E, Eye alt 5.6 km. DigitalGlobe 2013. <http://www.earth.google.com> [June 29, 2013].

Figures 2-12a and 2-12b show the uninterpreted and interpreted seismic data respectively. The 125,000 year gravels, an inter-fingering of river gravels with coastal sand, silt, clay, and peat from the last glacial-interglacial cycle (Brackley, 2012) is marked by a light blue horizon pick along a prominent reflector. The 125,000 year gravels mark high eustatic sea levels during the last interglaciation (Bal, 1996) when temperatures were warmer. Slip displacement is difficult to calculate in the shallow unconsolidated materials, however approximately 7 m of vertical deformation (assuming an interval velocity of 2400 m/s for 6 ms of time difference) exists along this horizon.

The Pliocene-Pleistocene Kowai Formation is interpreted by the yellow horizon near 300 ms. Vertical displacement is calculated to be approximately 17 m from a 13 ms time difference in the horizon marker 600 m on each side of the fault, assuming an interval velocity of 2600 m/s.

The Miocene volcanoclastic horizon marker is interpreted near 500 ms in red, or it possibly could also be interpreted as a Mid-Tertiary limestone. Vertical displacement is much more prominent at this reflector and approximately 26 m of displacement is calculated from the vertical time difference of 20 ms at the horizon 1 km on each side of the fault, assuming an interval velocity of 2600 m/s.

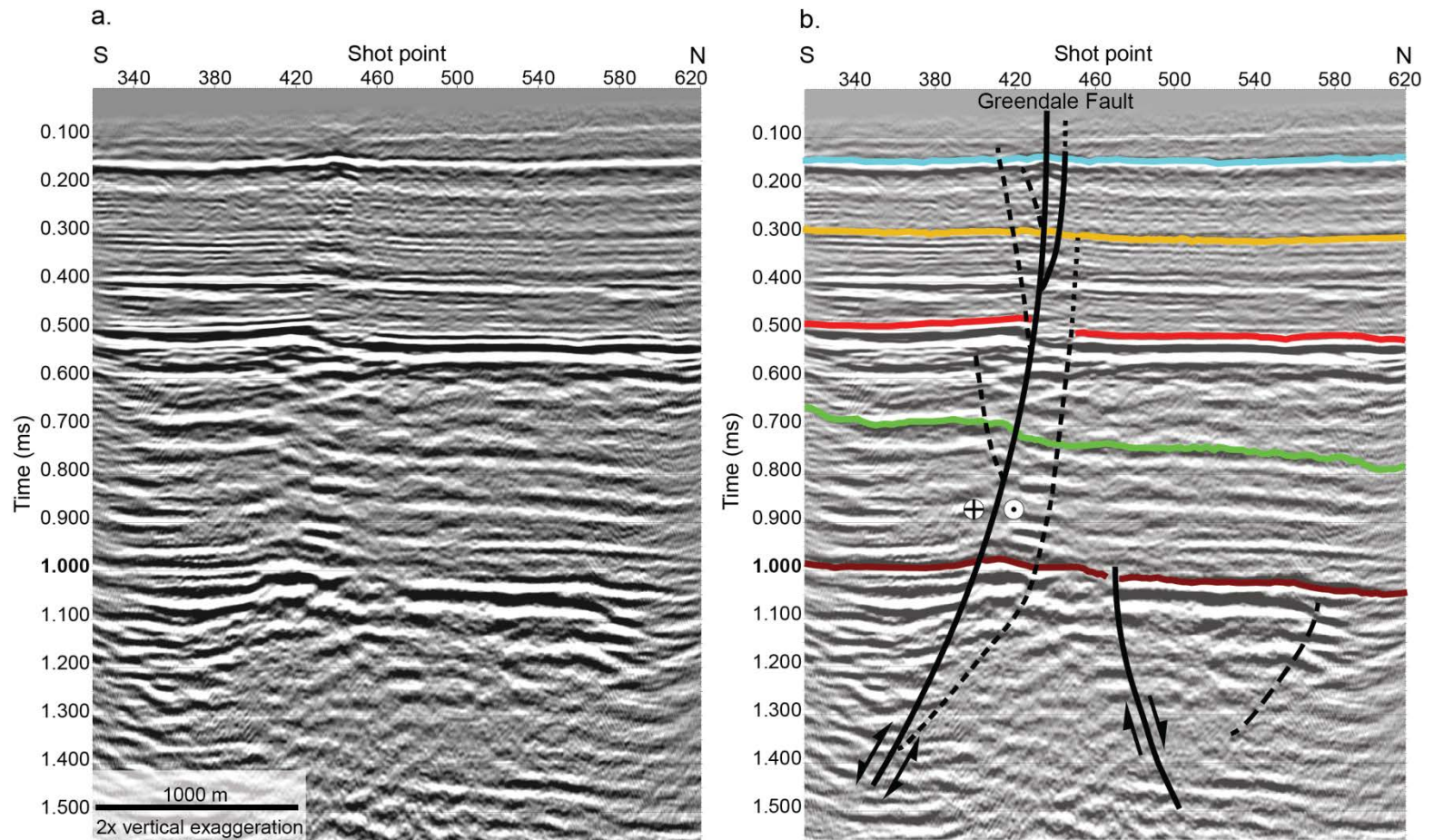


Figure 2-12. (a) Highfield Road seismic line uninterpreted. (b) With interpretation. The 125,000 year gravels are represented by the light blue horizon, the Top of the Kowai formation is represented by the yellow horizon, the Miocene volcanics/Mid-Tertiary limestone is represented by the red horizon, the Top of the Paleogene (?) is represented in green, and the undifferentiated Mesozoic basement is picked in brown. The Greendale fault is illustrated below station 440, where the fault ruptured the surface. Fault splays are indicated by short dashed lines off the main Greendale Fault.

The Top of the Paleogene, representing marine sediments and volcanic deposits during regional submergence and marine transgression (Forsyth et al., 2008) is speculated to be the green horizon marker interpreted near 750 ms. The Top of the Paleogene shows the most horizon offset (47 ms) on each side of the fault, with displacement of over 50 m for an assumed interval velocity of 2300 m/s.

The lowermost brown reflection marker is interpreted to be the top of the undifferentiated Mesozoic basement. Approximately 38 m of displacement offset is calculated on each side of the fault (time difference of 32 ms) for an interval velocity of 2400 m/s. The basement rock surface is approximately 1165 m deep.

The Greendale Fault is shown to rupture the surface. Several fault splays are also interpreted off the main Greendale Fault. The strike slip motion of the fault is indicated by towards and away arrows, with the foot wall on the north side of the fault displaced to the east, and the hanging wall on the south side of the fault displaced towards the west. A blind fault structure is interpreted to the north of the Greendale Fault, and is interpreted to be not reverse-reactivated. Further north below the basement, another possible fault is projected and indicated by a dashed line.

2.4.3 Discussion on fault reactivation

The faults in this study are comparable to south dipping E-W trending faults observed in Pegasus Bay (Barnes, 2011) and the southern Canterbury Plains (Jongens et al., 2012). Barnes identifies two types of basement involved faults: Cretaceous and

Paleogene inactive extensional structures, and basement faults that have undergone Plio-Pleistocene contractional and strike slip deformation. Most Plio-Pleistocene faults are considered reactivated Cretaceous and Paleogene structures which are predominantly E-W trending. It is highly probable that the Greendale Fault is associated with a reactivated Late Cretaceous normal fault (Jongens et al., 2012).

Barnes et al. (2011) infer that S-SE striking offshore faults have considerable strike-slip displacement, and more NE striking faults are more likely to have oblique-slip displacement, which is in agreement with the described structure of the Greendale and Port Hills faults, respectively.

Chapter Three: MASW INVESTIGATION OF AN ACTIVE FAULT ZONE

3.1 Introduction

Shear wave (S-wave) velocity studies can be used to characterize the stiffness of the shallow subsurface and evaluate the shear modulus of soil, an important task in geotechnical and environmental investigations. Applications include foundation dynamics, pavement analysis, soil improvement, liquefaction potential, and static corrections for S-wave reflection data (Pelton, 2005). Non-destructive surface wave analysis is quickly becoming a prominent method to generate near-surface S-wave velocity profiles. Surface wave analysis is based on the dispersive nature of Rayleigh waves propagating in a vertically heterogeneous medium (Rix, 2005). This chapter discusses the use of the multi-channel analysis of surface waves (MASW) method to investigate seismic velocities at two separate locations, each with a distinct sedimentary depositional environment near an active fault zone following the 2010-2011 Darfield and Christchurch earthquakes in New Zealand.

The MASW method (Park et al., 1999) expands upon the spectral analysis of surface waves (SASW) method developed by Nazarian et al. (1983), where dispersion curves from surface wave data are generated and inverted for S-wave velocity profiles. The main difference between the SASW and MASW method is an increase in the number of receivers used in acquisition. The MASW procedure records Rayleigh waves by acquisition of multi-channel shot records. Rayleigh wave dispersion curves are then constructed, analyzed, and inverted to generate S-wave velocity profiles as a function of depth. Greater detail of the MASW method is discussed in Section 3.2.

Many studies have investigated S-wave velocities at liquefied sites following earthquakes (Andrus and Stokoe, 1999; Bay and Cox, 2001; Kayabali, 1996; Pease and O'Rourke, 1997; Stokoe et al., 1988; among others). This leads to the importance of the MASW method, where a surge of research (Anbazhagan et al., 2010; Lin et al., 2004; Sundararajan and Seshunarayana, 2011; Trupti et al., 2012) has been devoted to investigate liquefied potential by means of the MASW method to obtain S-wave velocity profiles quickly and unobtrusively. The accuracy of the MASW method has been successfully tested with borehole measurements (Park et al., 1999; Xia et al., 2000a; Banab and Motazedian, 2010).

3.1.1 Liquefaction

3.1.1.1 Definition

Liquefaction is a process in which external forces cause a saturated mass of soil to suddenly lose its shear strength and behave as a fluid (Richart et al., 1970, p.172). Soil shear strength decreases when excess water pressure becomes equal to the acting earth pressure (Srbulov, 2008, p.119). Liquefiable soils are generally defined as loose sediments which range from silts to gravels, and the potential of liquefaction is a direct function of the shear stiffness of a soil (Glaser and Chung, 1995). Pore water pressure response varies with depth and distance from a source, suggesting liquefaction is largely controlled by the layered structure of the near surface (Inazaki, 2004). To predict the potential of liquefaction occurring, a liquefaction potential index was developed by Iwasaki et al. in 1978. However, liquefaction potential cannot be directly measured. What

can be measured are the direct or indirect parameters that control a soils tendency to liquefy upon seismic loading (Glaser and Chung, 1995). Liquefaction potential is a term used in this thesis which simply relates a soils tendency to liquefy with decreasing shear velocity measurements of the soil.

3.1.1.2 Liquefaction and application of shear wave velocity measurements

Measurements of shear wave velocity (V_s) can be used to identify areas with liquefaction potential, where lower values of V_s indicate lower rigidity and higher susceptibility to liquefaction. Andrus et al. (2004) showed that for sands with similar penetration resistance and age, values of V_s from liquefied sands are consistently less than values from non-liquefied sands. Also, S-wave velocity measurements can be used successfully to evaluate liquefaction resistance (Andrus and Stokoe, 1999), and can be used as a supplement or alternative to penetration based approaches (Yunmin et al. 2005). In stress-based liquefaction assessment, V_s is corrected for the effects of atmospheric pressure and overburden stress (Andrus and Stoke 1997, 1999).

Andrus and Stoke (1997) list two limitations of using V_s to evaluate liquefaction resistance of soils:

1. Weakly cemented soils may be classed as non-liquefiable by V_s criteria, but might in fact be liquefiable. Liquefaction is considered a large-strain phenomenon, and field measurements are made at small strains. Therefore

there are limitations in cemented soils as V_s is sensitive to weak particle bonding, which does not exist at large strains.

2. Samples are needed to classify soils and identify soft clay rich soils that are considered non-liquefiable (i.e. clay content $> 15\%$; or moisture content $< 90\%$ of the liquid limit).

3.1.2 Seismic wave types

Seismic waves cause elastic deformation within the material they propagate in, consisting of alternating compressions and dilations in the material as a response to forces associated with the travelling wave (Dobrin, 1976, p. 25). Wave propagation characteristics can primarily be described by body waves (compressional and S-waves) and surface waves (Rayleigh and Love waves). Body waves spread out on wavefronts that are generally spherical, whereas surface waves spread as an expanding circle across a surface (Stacey, 1992, p. 214).

3.1.2.1 Body waves

The particle motion of compressional waves in an elastic solid is in the direction of motion, and consists of alternating condensations and rarefactions (Dobrin, 1976, p. 35). Particle motion of S-wave propagation is perpendicular to the direction of wave propagation, and S-waves can only travel in solid materials since liquids do not have shear strength. Compressional speed is always greater than S-wave speed, with a V_p/V_s ratio of 1.5 to 2.0 for consolidated sediments (Dobrin, 1976, p. 37).

3.1.2.2 Surface waves

Two-thirds of total seismic wave energy is dominated by Rayleigh surface waves, and Rayleigh waves decay much slower than body waves with distance (Richart et al., 1970, p. 92). Rayleigh waves, the main component of ground roll, is of primary interest in the MASW method, and only Rayleigh waves will be discussed here. Rayleigh waves travel along the free surface of a solid material in a vertical plane, with elliptical and retrograde motion with respect to the direction of propagation (Dobrin, 1976, p. 38). An example of the Rayleigh wave radiation pattern for a vertical source is illustrated in Figure 3-1. An exponential decrease in amplitude of motion occurs with depth. When propagating in the same medium, Rayleigh wave velocity is approximately 90% of the S-wave velocity (Dobrin, 1976, p. 38).

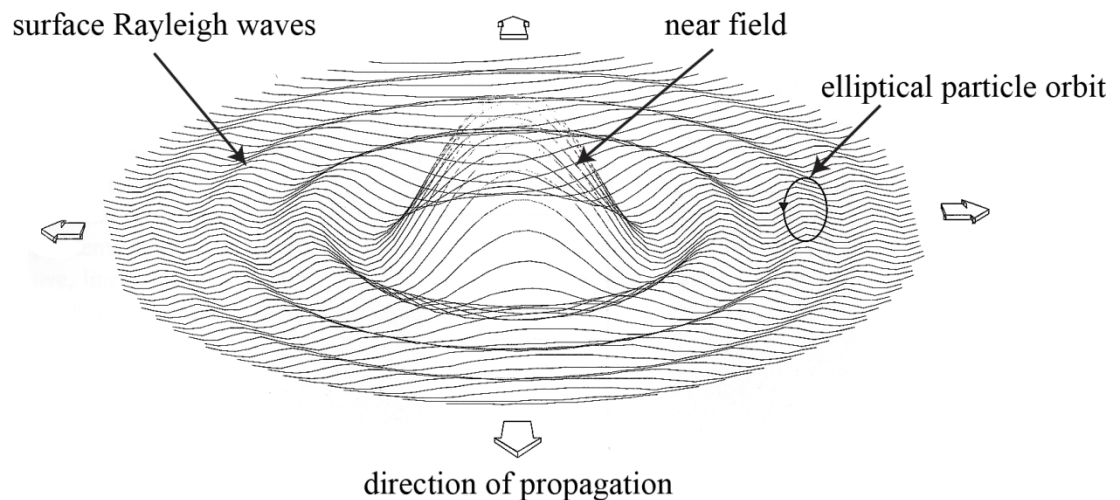


Figure 3-1. Radiation pattern of Rayleigh waves generated by a vertical source. Adapted from Lai, C.G. (2005).

3.1.3 Dispersion

For a vertically heterogeneous medium, Rayleigh wave propagation is dispersive, as velocity varies with frequency or wavelength (Sheriff, R.E., 1991, p. 76; Foti, 2005). Dobrin (1976) describes dispersive waves as appearing as a train of events in which successive cycles have increasing or decreasing periods. Given a low-speed layer which overlies a thicker high-speed layer, the properties of the top layer control speed for short wavelengths since short wavelengths will not penetrate the lower layer. The properties of the faster lower layer control speed for long wavelengths, and with farther penetration, the longer wavelength will have higher velocities which then cause the wavelength to shorten towards the end of the wave train. In each layer, the speed of the Rayleigh wave is approximately 90% of shear velocity in the material (Nazarian et al., 1983). Rayleigh wave phase velocity is influenced by S-wave velocity, P-wave velocity, layer thickness, and density (Xia et al., 1999). As Rayleigh waves have a broad range of frequencies, a dispersion curve (phase velocity vs. frequency) can be constructed (Rix, 2005). Dispersion curves are further discussed in section 3.2.2.

Since Rayleigh waves have a range of velocities at any particular frequency, multiple modes of propagation exist and each are associated with a unique dispersion curve (Tokimatsu et al., 1992). The fundamental mode has the lowest velocity and frequency at which the Rayleigh wave propagates, and for this study only fundamental mode dispersion curves are considered and used in the inversion.

3.2 Theoretical background of the MASW method

The MASW procedure is briefly summarized in three steps:

1. Acquisition of multichannel shot records and recording of Rayleigh waves
2. Construction of Rayleigh wave dispersion curves by wavefield transformation from the offset-time (x - t) domain to frequency-phase velocity (w - v) domain.
3. Obtain an S-wave velocity profile as a function of depth by inversion of the dispersion curve.

Constructing dispersion curves (step 2) is considered to be the most critical step for later inversion of an accurate shear-wave velocity profile (Park et al., 1999). Inversion of the dispersion curve (step 3) is considered the most difficult of the three steps as an optimization technique is required to find a non-unique solution (Pelekis and Athanasopoulos, 2011). Each step is described in greater detail in the following sections.

3.2.1 Acquisition

Data for MASW analysis may be acquired by the passive or active method, whose main difference is the source used to generate seismic waves. Both methods use a survey line of low frequency evenly spaced vertical geophones as receivers, attached to a seismometer and recorded. The objective is to record horizontally travelling, fundamental mode Rayleigh plane waves.

The passive MASW method uses natural background noise (i.e. tidal waves) or cultural noise (i.e. road traffic) as a seismic source. Lower frequencies are obtained in the passive MASW method, and thus greater depth of penetration. The active MASW method, introduced by Park et al. (1999), uses a controlled seismic source such as Vibroseis or an impulsive source such as a hammer on a plate.

Recommended MASW survey parameters such as source offset to nearest receiver, and receiver spread length have been under debate (Park and Carnevale, 2010). Source offset to nearest receiver (also referenced as ‘source offset’ or ‘near offset’) is an important parameter in avoiding near-field effects. Near-field effects are those that occur when the assumption of horizontal propagation of surface waves as a plane wave is invalid near the source, and the adverse effect decreases with increased offset (Yoon and Rix, 2009). Often, the phase velocities of the surface waves are lower in the near field than elsewhere; however this is dependent on field location and can sometimes be negligible (Park and Carnevale, 2010).

Field tests have shown an empirical criterion $Z_{max} = L/2$, which relates maximum depth of investigation Z_{max} and receiver spread length, L . Park and Carnevale (2010) studied the dependence of maximum wavelength (λ_{max}) on L and found that phase velocities start to fluctuate in an oscillatory pattern for $\lambda \geq L$, however further investigation is needed from a diverse selection of field studies and soil types. As a current guideline for maximum accuracy in measuring maximum wavelength, $\lambda_{max} \approx L$. Therefore, maximum depth of investigation is determined by maximum wavelength. Park

and Carnevale (2010) also showed that increasing source offset can extend maximum wavelength, and hence maximum depth of investigation.

If the spread length is too large, body waves may contaminate the high frequency components of surface wave energy due to attenuation with increasing offset. This is known as the far-offset effect (Park et al., 1999).

The near-field and far-offset effects can be evaluated for quality control in a swept frequency multichannel record, obtained by an uncorrelated Vibroseis field record, or by an impulsive record passed through a stretch function (Park et al., 1999). The near-field effect is observed as a lack of linear coherency in phase at lower frequencies. The far-offset effect is observed as a decrease in ground roll slope due to interfering body waves increasing the phase velocity. Field data examples from Park et al. (1999) show these effects in Figure 3-2.

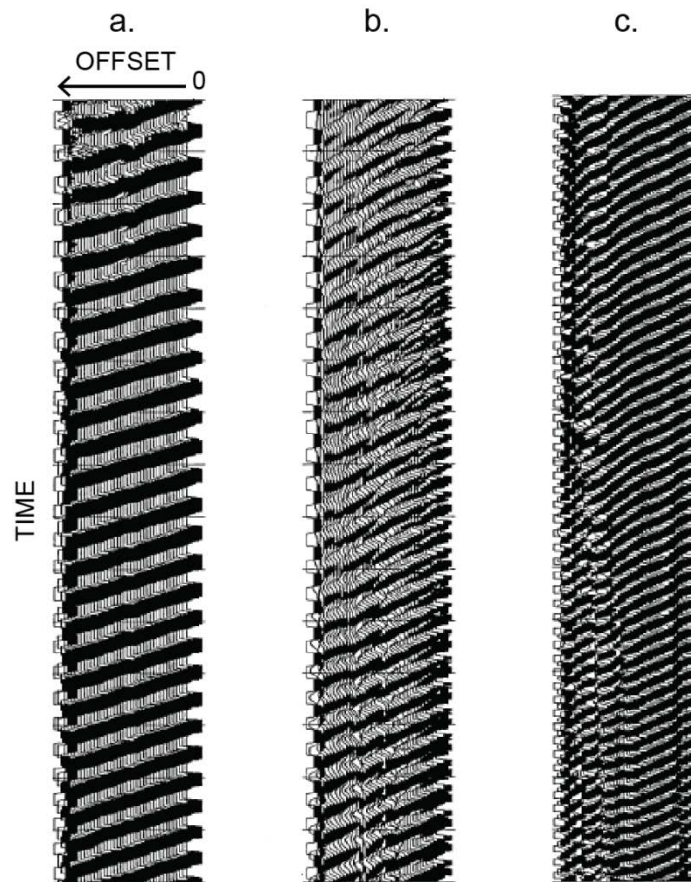


Figure 3-2. Near-field and far-field effect of ground roll observed in swept-frequency records obtained by uncorrelated Vibroseis records. Good quality data is shown in (a), where the source offset is 27 m. The near-field effect is shown in (b) with a source offset is 1.8 m. Linear coherence is reduced by weaker energy and discontinuous energy packets. Arrivals show increased frequencies. The far-field effect is shown in (c) with a source offset of 89 m. Linear coherence is reduced due to interference from high velocity body waves. Far offset effects are seen as a decrease in ground roll slope (an increase phase velocity). Adapted from Park et al. (1999).

3.2.2 Dispersion curve – Fundamental mode

The 2D wave field transformation technique (Park et al., 1998) is used to transform each multi-channel shot record in the offset-time domain to the phase velocity-frequency domain and image dispersion curves, where the Rayleigh wave fundamental

mode is determined. The transformation method is described by Park et al. (1998) in three steps:

1. A Fourier transform is applied to shot gather data $u(x,t)$ in offset-time domain, to obtain $U(x,w)$:

$$U(x,w) = \int u(x,t)e^{i\omega t} dt = P(x,w)A(x,w) \quad (3.1)$$

where x is offset, t is time, and w is angular frequency. $U(x,w)$ is also regarded as the multiplication of the phase spectrum $P(x,w)$ and the amplitude spectrum $A(x,w)$. The phase spectrum $P(x,w)$ contains dispersive property information, and the amplitude spectrum $A(x,w)$ contains other property information such as spherical divergence and attenuation. As a result, $U(x,w)$ can be expressed as:

$$U(x,w) = e^{-i\psi x} A(x,w) \quad (3.2)$$

where $\psi = w/c_w$, and c_w is the phase velocity for angular frequency w .

2. An integral transformation is then applied, and is considered as the summing over offset of wavefields of a frequency after applying an offset-dependent phase shift (ϕ) determined for an assumed phase velocity ($c_w = w/\phi$) to the wavefields $U(x,w)$ in equation 3.2 to obtain $V(w,\phi)$:

$$V(w,\phi) = \int e^{i\phi x} \left[\frac{U(x,w)}{|U(x,w)|} \right] dx = \int e^{-i(\phi-\psi)x} \left[\frac{A(x,w)}{|A(x,w)|} \right] dx \quad (3.3)$$

Normalization of $U(x,w)$ with respect to offset is required to ensure equal weighting from the effects of attenuation and spherical divergence at different offsets during wavefield analysis. As a result, for a given frequency (w), $V(w,\phi)$

will have a maximum if $\phi = \varphi = w/c_w$. The phase velocity (c_w) can then be determined for a value of ϕ where a peak of $V(w, \phi)$ occurs. More peaks will occur if higher modes have substantially more energy.

3. The $V(w, \phi)$ wavefield is transformed to the $I(w, c_w)$ wavefield by changing variables such that $c_w = w/\phi$. The trend of peaks in the phase velocity axis of the $I(w, c_w)$ wavefield for a given frequency results in dispersion curve construction.

Other techniques in multichannel analysis have been used to calculate dispersion curves. McMechan and Yedlin (1981) proposed a slant-stack method transformation from the x-t domain to the intercept time – phase slowness (τ - p) domain followed by a 1D Fourier transform over τ to the p - w domain. Gabriels et al. (1987) measured the dispersion properties of Rayleigh waves in the frequency-wavenumber (f - k) spectrum. However, at the time of publication, the method presented by Park et al. (1998) extracts multimodal dispersion curves with the highest accuracy, and is the method used to image dispersion curves in the SurfSeis 3.15 software. Analysis and removal of noise, such as body waves on ground roll data can enhance the accuracy of the dispersion curve (Park et al., 1999).

3.2.3 Inversion

Inversion is defined as deriving a model to describe the subsurface, which is consistent with measured field data (Sheriff, R.E., 1991, p. 162). Inversion of the fundamental mode dispersion curve given a set of initial earth model parameters is used

to derive S-wave (V_s) profiles of the near surface. Inversion schemes for MASW differ in the computation of the forward model and the method of optimization (Pelton, 2005). The inversion method of Xia et al. (1999) is used in this analysis and applies a linearized iterative damped least-squares approach, where only the fundamental mode is considered.

An initial earth model with laterally homogeneous, isotropic, and linearly elastic horizontal layers is assumed. Four parameters define the initial earth model: P-wave velocity, S-wave velocity, density, and thickness. The initial P-wave velocity (V_p) is determined in SurfSeis 3.15 by the initial V_s model, and entering a fixed value of Poisson's ratio. The initial V_s model is estimated from the measured phase velocities of the dispersion curve, such that V_s is 1.09 times the measured phase velocity (Stokoe et al., 1994). The S-wave velocity has the greatest effect on the most reliable convergence of the algorithm (Park et al., 1999). Using the initial model, theoretical dispersion curves (phase velocities as a function of frequency) are calculated using the forward modeling scheme of Schwab and Knopoff (1972). The theoretical dispersion curves are then compared to the measured dispersion curve data, and iteratively updated until a minimization of the misfit function is met.

A root mean square error (RMSE) graph between the measured and calculated dispersion curves is generated for each inversion process, and acts as a constraint where iterations update until a stopping criteria of minimum RMSE, or maximum number of iterations is met. Two formulas are employed to calculate RMSE at the i th iteration in

SurfSeis 3.15 during inversion. For equal weight, where equal confidence is given to each phase velocity in the dispersion curve, the RMSE is given as:

$$E_{RMS} = \sqrt{\frac{\sum_{k=1}^n [O^k - T_i^k]^2}{n}} \quad (3.4)$$

where O and T are the observed and calculated phase velocities respectively. A weighted RMSE can also be selected to give weight to dispersion data based on signal-to-noise ratio:

$$E_{RMS} = \sqrt{\frac{\sum_{k=1}^n w^k [O^k - T_i^k]^2}{\sum_{k=1}^n w^k}} \quad (3.5)$$

where w^k is the weight of the k th data. A long lasting inversion with a high number of iterations may result in a large RMSE, and is often due to a velocity reversal in Vs. The RMSE can be used to evaluate confidence in the results.

3.3 Data acquisition and study area

Two locations were selected for MASW investigation: New Brighton Beach (Line 1) along the eastern edge of Christchurch, and Highfield road (Line 3) which crosses the Greendale Fault. Acquisition parameters of the 2D seismic data are summarized in Table 3-1. The data was originally acquired with the objective of detecting and mapping previously unknown faults, and a MASW investigation is an addendum. The natural frequency of the geophone and source type limit the lowest frequency recorded (Park et al., 1999).

Table 3-1. Seismic data acquisition parameters

Geophones	Sensor SM-24 10 Hz vertical component
Seismic source	IVI Envirovibe. 10 – 120 Hz sweep, 10 s, 8 sweeps
Recorder	4000 ms recording length, 1 ms sample rate
Source spacing	10 m
Receiver spacing	10 m

3.3.1 Data acquisition at New Brighton Beach (Line 1)

Over 8 km of 2D seismic data was acquired along New Brighton Beach; however only 730 m of data near the center of the 2D line (stations 586 to 659) is used for MASW analysis (Figure 3-3). This segment was chosen for MASW analysis as it was the longest segment acquired with continuous stations and even shot spacing of 10 meters. Data were acquired on the beach in conditions ranging from saturated to dry sand, with most acquisition along the water line where ground conditions were wet but not saturated (Bertram, M., personal communication, 2013). Soil type in the shallow surface (top 60 m) is provided by Environment Canterbury well M35/7753, which is located approximately 500 m south of the segment used for MASW analysis. The shallow stratigraphy is dominated by the fine-grained Christchurch Formation (Wilson, D., 1976). The borelog indicates a water depth of -0.9 m and damp beach sand in the top 9 m. Gravels are detected at depths greater than 30 m.

3.3.2 Data acquisition at Highfield Road (Line 3)

The seismic survey along Highfield Road collected 3040 m of 2D seismic data from stations 306 to 641, and crossed the ruptured Greendale Fault near station 440 (Figure 3-4). Environment Canterbury Well L36/1199 on the northern end of the survey

indicates the top 46 m is dominated by claybound gravels, and the initial water depth is - 32.5 m with a minimum calculated water level encountered at -41 m. The Environment Canterbury well borelogs are available in Appendix D.

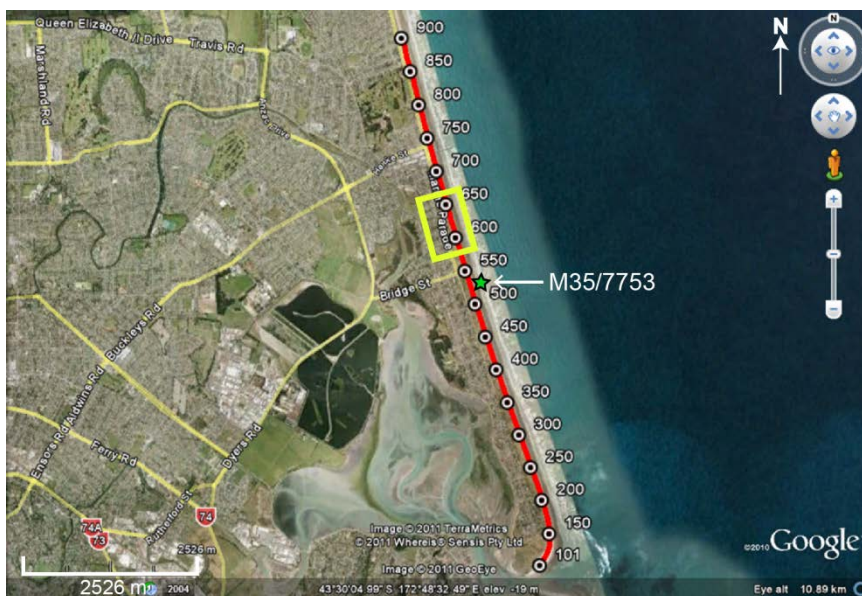


Figure 3-3. New Brighton Beach seismic line, east of Christchurch city center. The yellow box highlights the segment used for MASW analysis. Environment Canterbury well is indicated by a green star. Adapted from Hall et al., (2011). Image © 2011 TerraMetrics and © 2011 Whereis® Sensis Pty Ltd and Image © 2011 GeoEye (Google Earth, 2011).

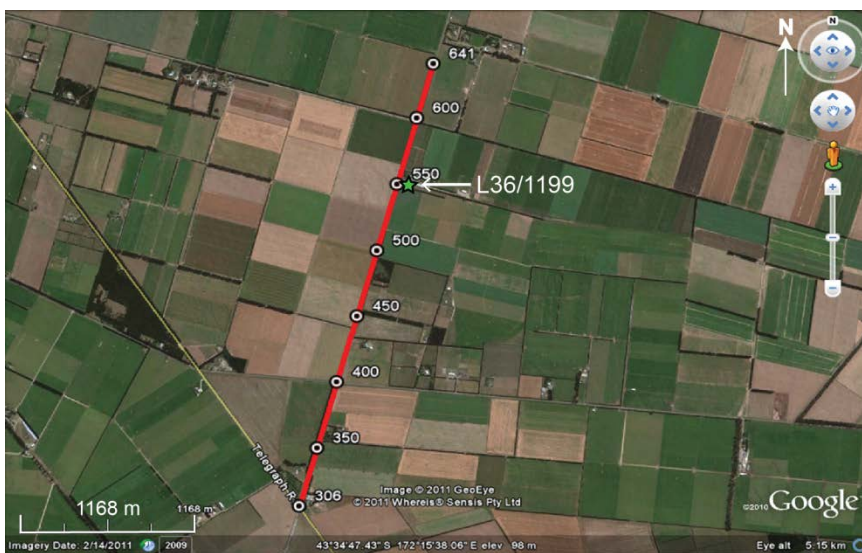


Figure 3-4. Highfield Road seismic line, approximately 35 km west of Christchurch city center. The Environment Canterbury well is indicated by a green star. The Greendale Fault was transverse near Station 440. Adapted from Hall et al., (2011). Image © 2011 TerraMetrics and © 2011 Whereis® Sensis Pty Ltd and Image © 2011 GeoEye (Google Earth, 2011).

3.4 Surface wave analysis

Surface wave analysis begins with enhancing the low frequency surface waves while suppressing noise from body wave contamination. The generalized data processing flow applied to each Line 1 and Line 3 is shown in (Figure 3-5). Processing parameters were selectively chosen to enhance each independent dataset. The ProMAX software package for seismic data processing was used to prepare the seismic data for surface wave analysis in SurfSeis 3.15.

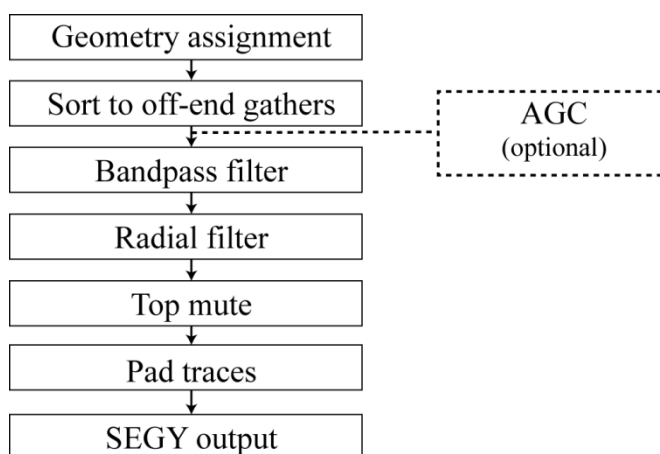


Figure 3-5. Seismic data processing flow applied prior to dispersion curve analysis.

3.4.1 New Brighton Beach (Line 1)

3.4.1.1 Data processing

The segment of beach line processed for surface analysis includes seismic acquisition of 73 shots over a total distance of 730 m. To illustrate the frequency range captured, Figure 3-6 shows a raw shot record, with window A outlining the frequency spectra from 0 to 2750 ms, and window B capturing the frequency content below the reflection events at 900 to 1625 ms. The frequency content in window A shows the

frequency range to be within 10 to 120 Hz, with a 40 Hz spike most likely due to a nearby generator. The frequency content captured in window B at the lower time window is focused more on lower frequency events which include surface waves, with the broader band occurring between 10 and 60 Hz.

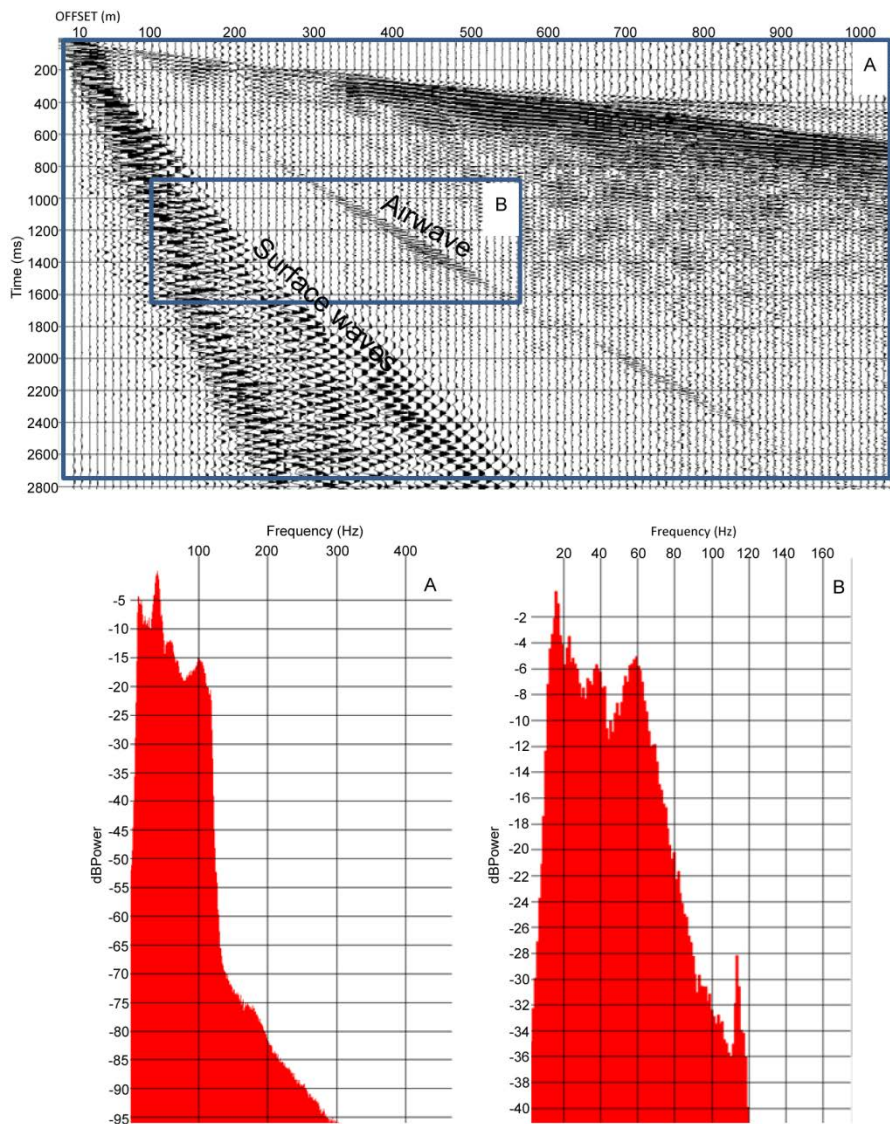


Figure 3-6. Frequency content of a raw shot record from New Brighton Beach. The frequency content for entire window (A) is shown, and the frequency content for a window focused on the surface waves is shown (B).

The data is sorted to off-end geometry (also called end-on geometry) for dispersion curve analysis. The data were originally acquired having a split spread geometry with a central shot, and was subsequently arranged to an off-end geometry with a shot on the left end of the spread, and receivers to the right side of the shot (Figure 3-7). For this analysis, only receivers with a positive offset were used, resulting in right off-end geometry. The shots were then padded with dead traces to maintain equivalent number of channels per shot as required for analysis in SurfSeis 3.15.

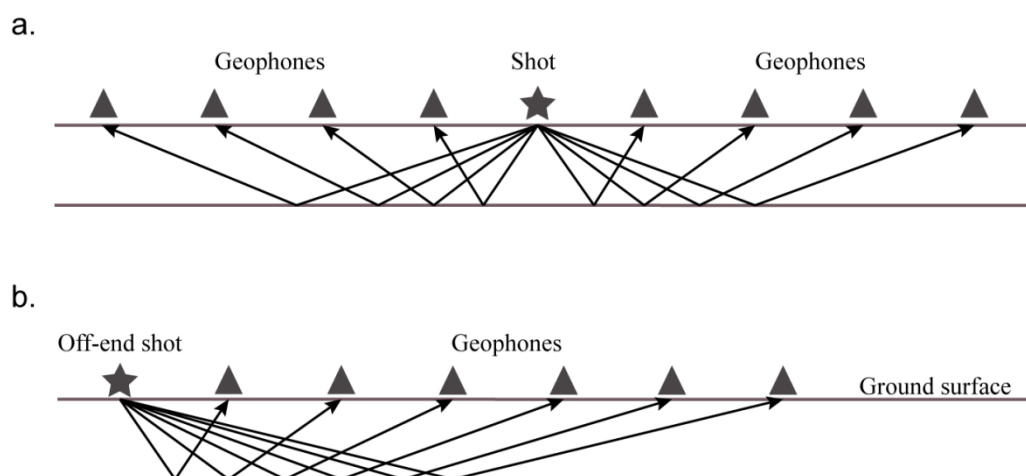


Figure 3-7. Seismic acquisition for (a) split-spread geometry, and (b) off-end geometry.

Seismic events and associated velocities are indicated in Figure 3-8a, where the direct arrivals (event A) are 1689 m/s, and Rayleigh waves are indicated by events B and C at 229 m/s and 111 m/s respectively on a raw shot gather at FFID 586. A bandpass filter of 0-3-32-38 Hz was applied (Figure 3-8b) to remove the air wave, and higher frequency body waves. To better isolate the surface waves, a radial trace (RT) domain filter (Henley, 2003) was applied (Figure 3-8c). The data was transformed from the $x-t$ domain to the RT domain where surface waves are isolated by designing an RT fan filter

to represent a wide range of velocities. For a single source, the fan filter is an appropriate design to best attenuate a variety of linear noises at different velocities (Henley, 2003). Traditionally, attenuation in the radial trace domain is designed to attenuate coherent noise such as a ground roll (Bagheri et al., 2007). However, in this case a low pass filter is designed to keep low velocity and low frequency events. A radial trace velocity of ± 1500 m/s and a maximum frequency low pass filter of 35 Hz were applied to the beach line.

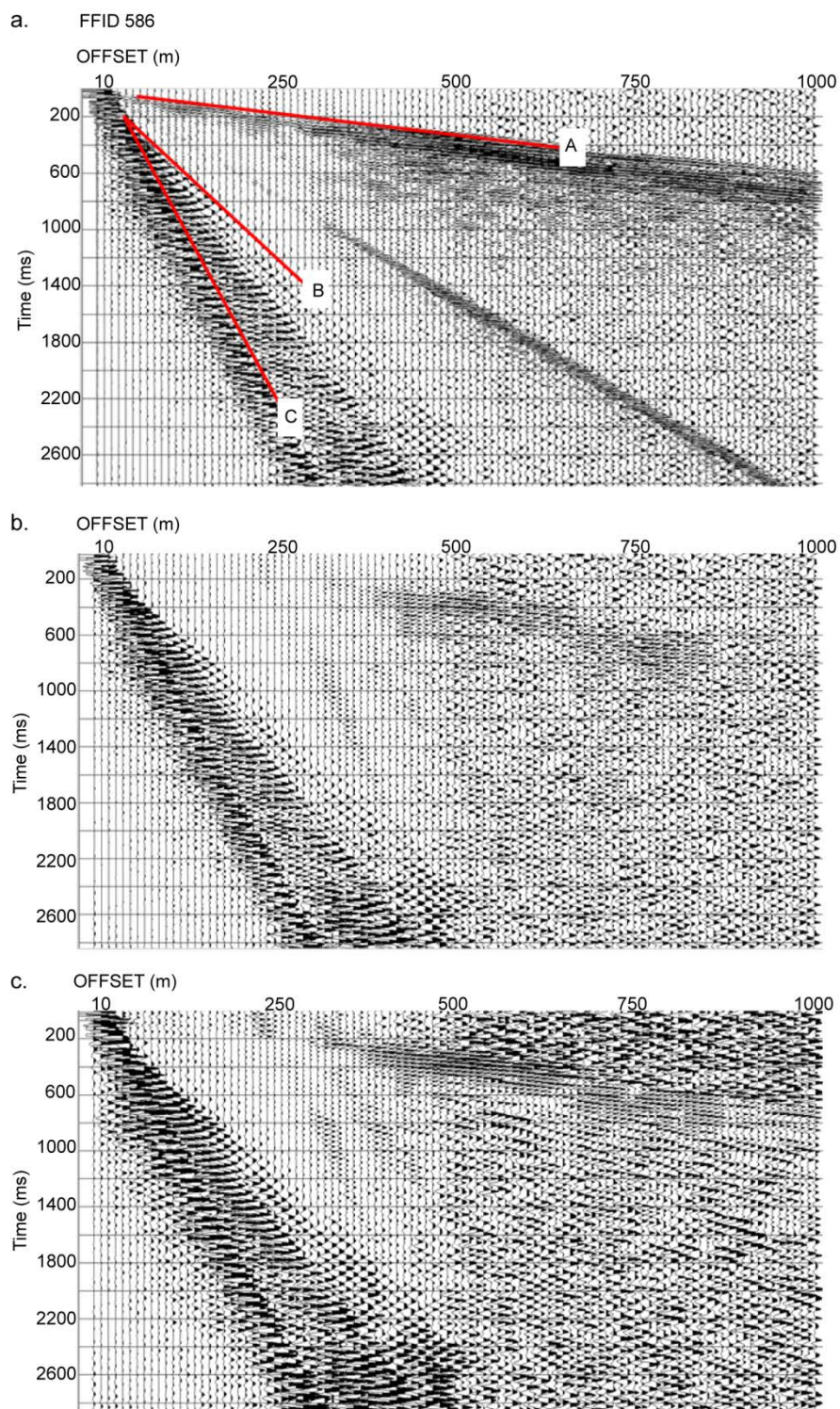


Figure 3-8. (a) Raw shot record showing direct arrivals (A at 1689 m/s) and surface wave events (B & C at 229m/s and 111 m/s respectively), (b) with a 0-3-32-38 Hz bandpass filter applied, (c) with a Radial Trace filter applied.

To ensure the strong energy and large range of frequencies from the refracted events does not dominate the surface wave events during later dispersion curve analysis, a time domain top mute was applied to reject the first arrival (Figure 3-9) as a final processing step.

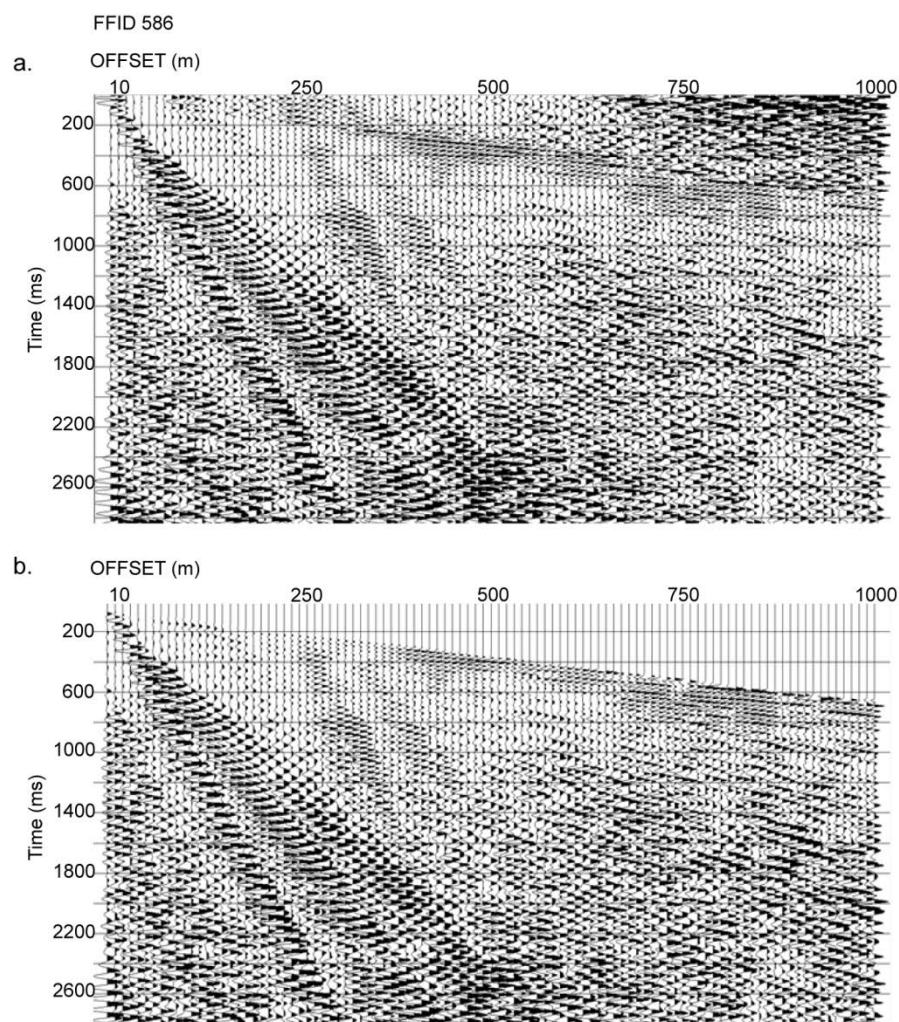


Figure 3-9. (a) Shot gather with first arrivals displayed, and (b) with a top mute applied.

3.4.1.2 Dispersion curve analysis

The shot gathers were loaded into SurfSeis 3.15 and converted from SEG Y to KGS format and geometry was applied. Surface waves are detected in each shot gather by selecting optimum parameters such as an estimation of phase velocity and frequency range for each record. The 2D wavefield transformation method (Park et al., 1998) transforms each shot gather into a dispersion image (also called overtone image) of phase velocity versus frequency. Figure 3-10 shows an initial overtone image created which displays a broad phase velocity range of 0-3000 m/s and frequency range from 0-45 Hz. The broad ranges are selected for display in order to identify and evaluate dispersion trends of the fundamental mode, higher modes, and any noise which may contaminate the dispersion curves. A source-receiver offset of 10 m and spread length of 100 m from the source resulted in 9 traces used to generate the dispersion image. For each shot record, a dispersion curve is picked along the fundamental mode in the overtone image and extracted, to be later inverted and generate a 1D S-wave velocity profile of the near surface.

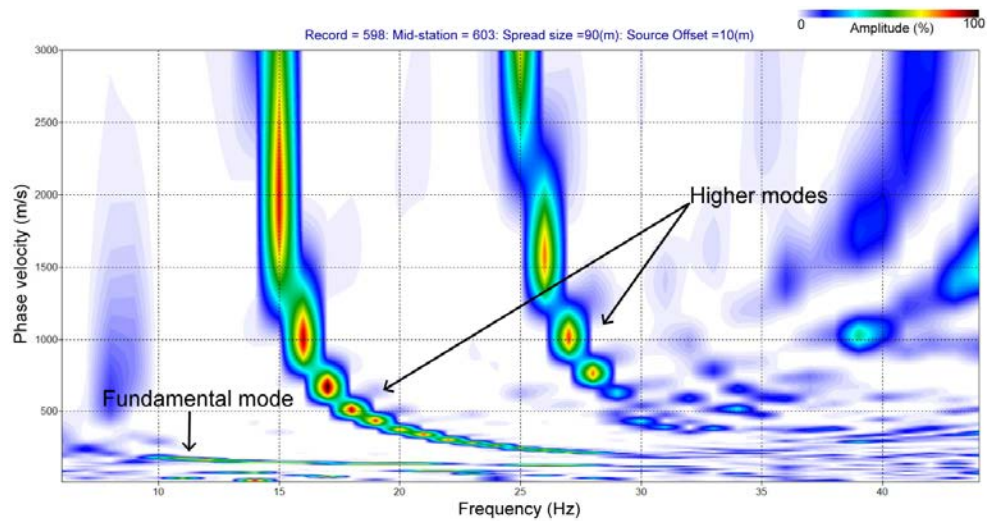


Figure 3-10. Overtone image displaying the fundamental mode, and higher modes. A broad phase velocity range (0 - 3000m/s) identifies fundamental and higher modes.

Dispersion curve resolution is affected by spread length. Linear spread length is related to the lower frequency range of the dispersion image and limits the highest recordable wavelength (Dikmen et al., 2010). Spread length should be kept as short as possible since the MASW method assumes a vertically heterogeneous layered earth model with no lateral variation in elastic properties (Park et al., 1999). Figure 3-11 shows how dispersion image resolution is affected by spread length, where spreads of approximately 300, 200, 150, and 100 m are selected for investigation. For this dataset, dispersion image resolution is best obtained when a spread length of 100 m is selected.

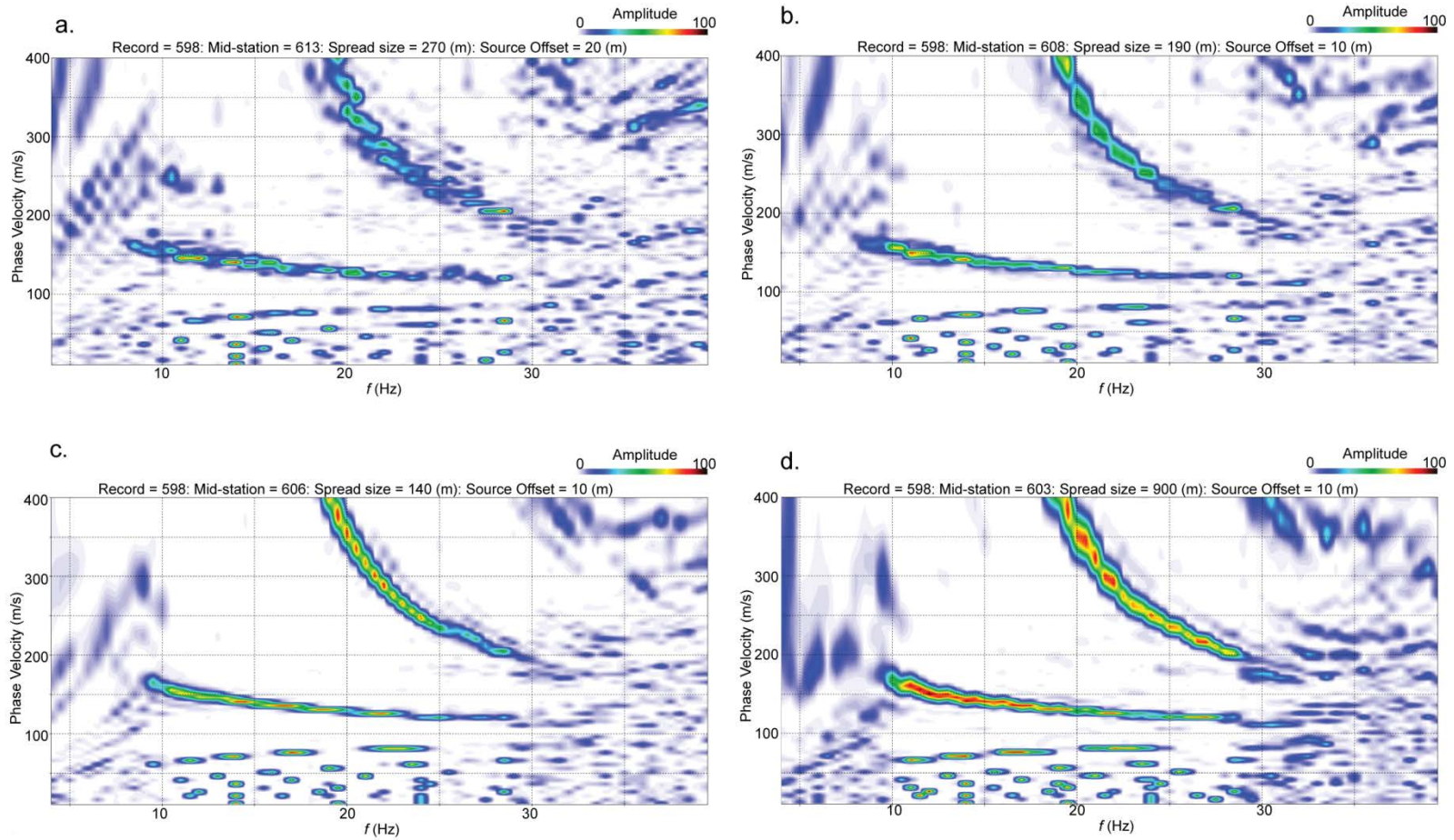


Figure 3-11. Testing spread length parameters and dispersion curve resolution of the fundamental mode. (a) Spread length = 300 m; (b) Spread length = 200 m; (c) Spread length = 150 m; (d) Spread length = 100 m.

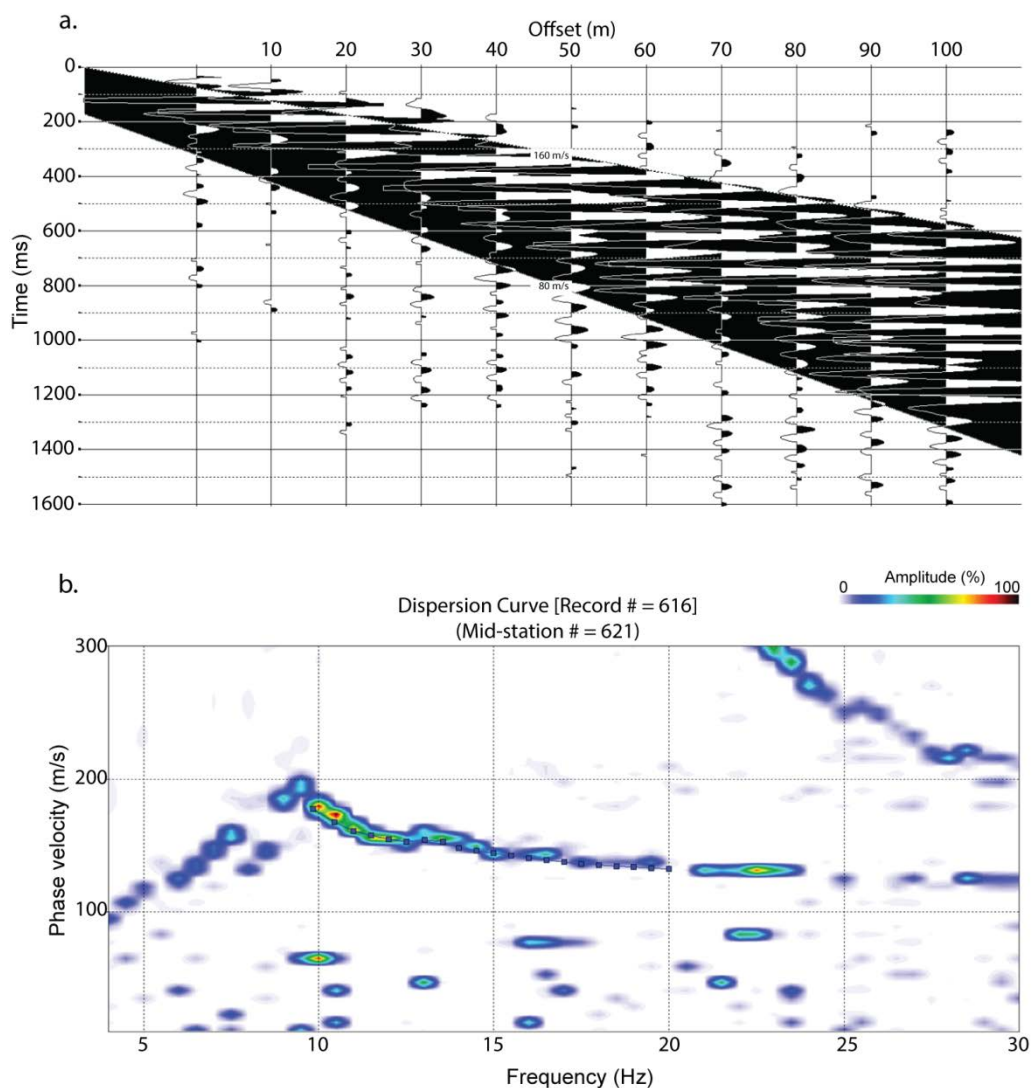


Figure 3-12. (a) Surface wave range identified in SurfSeis 3.15 for a 100 m spread length, (b) Corresponding dispersion image

Surface waves are identified for analysis (Figure 3-12a) within a spread length of 100 m, and from time 0 – 1600 ms. The resulting dispersion image (Figure 3-12b) is focused on the phase velocity and frequency range of the fundamental mode energy. The fundamental mode energy ranges from approximately 10 – 20 Hz, with a phase velocity of 125 – 190 m/s. A dispersion curve is extracted by setting a reference frequency of 15

Hz and corresponding phase velocity of 140 m/s. The program extracts a dispersion curve along a set bounding frequency range, and is usually manually edited to preserve a general down-going trend, while maintaining a reasonable signal-to-noise (S/N) ratio. The S/N ratio is expected to decrease as frequency increases as a result of added noise introduced at higher frequencies (Park et al., 1999). The phase velocity of the dispersion curve is also expected to decrease with increasing frequency, resulting in a down-going trend, unless a stiffer material (i.e. clay, partially cemented sediment, or pavement) overlies the survey area (Miller et al., 1999). The extracted dispersion curves for each seismic record are saved for inversion analysis.

3.4.1.3 Inversion analysis

During the inversion process (adopted in SurfSeis by Xia et al., 1999), a V_s profile is sought which has a theoretical dispersion curve that best corresponds with the measured dispersion curve. The initial vertical V_s profile can be calculated by: referencing phase velocities of the measured dispersion curve for each record using the inversion results of the previous dispersion curve record, using a fixed velocity-depth model for all records, or calculate an initial model for each record independently. Parameters of the initial earth model include V_s , P-wave velocity (V_p), density (ρ), and layer thickness (h); however V_s is the most significant parameter to the surface wave phase velocity analysis as a 25% change in V_s results in a 39% change in Rayleigh wave phase velocity (Xia et al., 1999). For an initial model calculated for each dispersion curve using phase velocities, the initial P-wave velocity is calculated using the initial V_s profile and a constant Poisson ratio of 0.4. A constant density (2000 kg/cm^3) with 10 layers is

also assigned. Layer thickness is variable and increases with depth to a maximum depth determined from the longest wavelength of the dispersion curve, with the last layer assumed to be a half-space. The inversion procedure iterates until a minimum root mean square error (RMSE) or the maximum number of iterations (set to 10 for this data set) is reached.

The dispersion curve for record 601 with the picked fundamental mode, and the associated inverted Vs profile to a depth of 7 m, calculated using an initial model derived from its own independent dispersion curve is shown in Figure 3-13. In addition to the picked fundamental mode (Figure 3-13a), an additional higher mode is apparent with frequencies >20 Hz. In Figure 3-13b, the extracted dispersion curve picks are plotted as the measured fundamental mode (linked black circles). The Vs initial earth model (blue dashed line) is forward modeled to obtain a theoretical dispersion curve that best matches the measured dispersion curve, and is plotted with the final inversion result (solid blue line). The initial and extracted dispersion curves are compared, and the initial model is updated (three iterations in this case) until the final model was obtained. The general trend of the final Vs curve generally has a good fit in an approximate sense with the picked dispersion curve, and improves upon the initial model. However, at lower frequencies, or in the deeper earth layers (> 5.75 m), a higher velocity is given in both the initial and final curves, compared to that of the measured dispersion curve due to the halfspace. The inverted 1D Vs profile represents an average at the midpoint of each spread, and a 2D Vs velocity model is created using a spatial interpolation scheme (Luo et al., 2008).

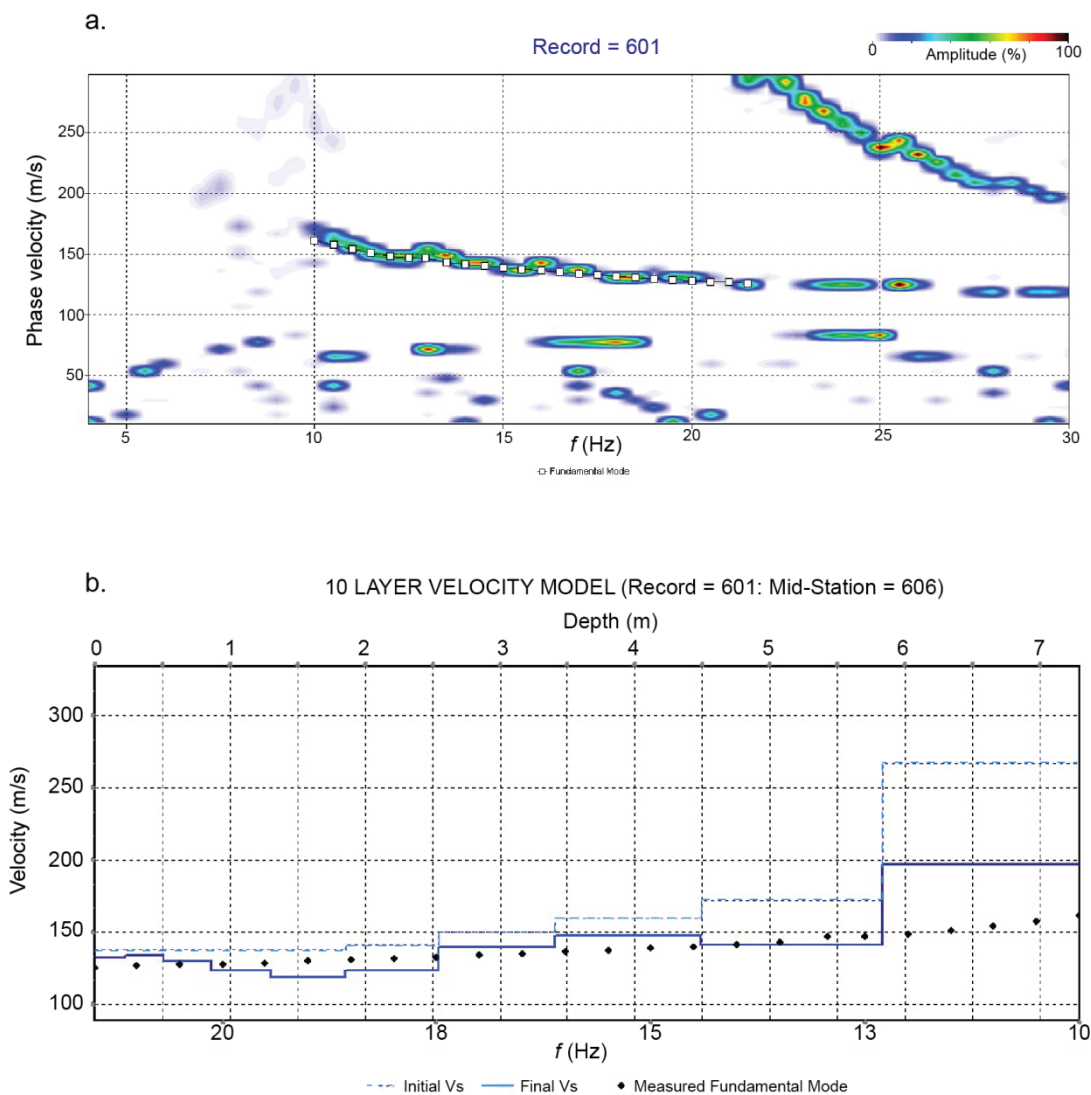


Figure 3-13. (a) Fundamental model picks for the dispersion curve at Station 601, (b) Inversion results, where the black circles show the trend of the measured fundamental mode, the dashed blue line represents V_s of the initial model, and the solid blue line represents V_s of the final inversion results.

The 2D shear velocity-depth model for the top 7 m of the beach line is shown in Figure 3-14 for three different initial models and the results are comparable. The initial model is based on a 10 layer model with increasing layer thickness with depth and a fixed Poisson ratio of 0.4. The initial model was created based on station 601 with a 66%

signal-to-noise ratio. The sensitivity of the results to density in the initial model is examined, with densities of 1700 kg/cm^3 , 2000 kg/cm^3 , and variable density ranging from 1550 to 2000 kg/cm^3 with depth. The initial model with variable density is given in Table 3-2 (with final velocity model shown in Figure 3-14c). Results show S-wave velocities of approximately 130 m/s in the top 3 m , with pockets of slower velocities approaching 100 m/s (as indicated by dark blue coloring). In the $3 - 6 \text{ m}$ range, velocities are shown to be approximately 150 m/s , with S-wave velocity increasing to 175 m/s in some areas. Below 6 m , velocities are shown to rapidly increase to 200 m/s . A localized decrease in velocity is seen at station 615.

Table 3-2. Initial model for 10 layers, variable density, and a fixed Poisson ratio of 0.4

LAYER	BOTTOM (m)	THICKNESS (m)	V _S (m/s)	V _P (m/s)	PR	DENSITY (kg/cm ³)
1	0.226	0.226	138	338	0.4	1550
2	0.509	0.283	138	338	0.4	1600
3	0.862	0.353	138	338	0.4	1650
4	1.304	0.442	138	338	0.4	1700
5	1.856	0.552	138	338	0.4	1750
6	2.546	0.690	141	344	0.4	1800
7	3.409	0.863	150	367	0.4	1850
8	4.487	1.078	160	392	0.4	1900
9	5.835	1.348	172	422	0.4	1950
10	Half Space	Infinity	267	653	0.4	2000

Table 3-3. Initial model for 10 layers, variable density, and a fixed Poisson ratio of 0.15

LAYER	BOTTOM (m)	THICKNESS (m)	V _S (m/s)	V _P (m/s)	PR	DENSITY (kg/cm ³)
1	0.226	0.226	138	215	0.15	1550
2	0.509	0.283	138	215	0.15	1600
3	0.862	0.353	138	215	0.15	1650
4	1.304	0.442	138	215	0.15	1700
5	1.856	0.552	138	215	0.15	1750
6	2.546	0.690	141	219	0.15	1800
7	3.409	0.863	150	233	0.15	1850
8	4.487	1.078	160	249	0.15	1900
9	5.835	1.348	172	268	0.15	1950
10	Half Space	Infinity	267	416	0.15	2000

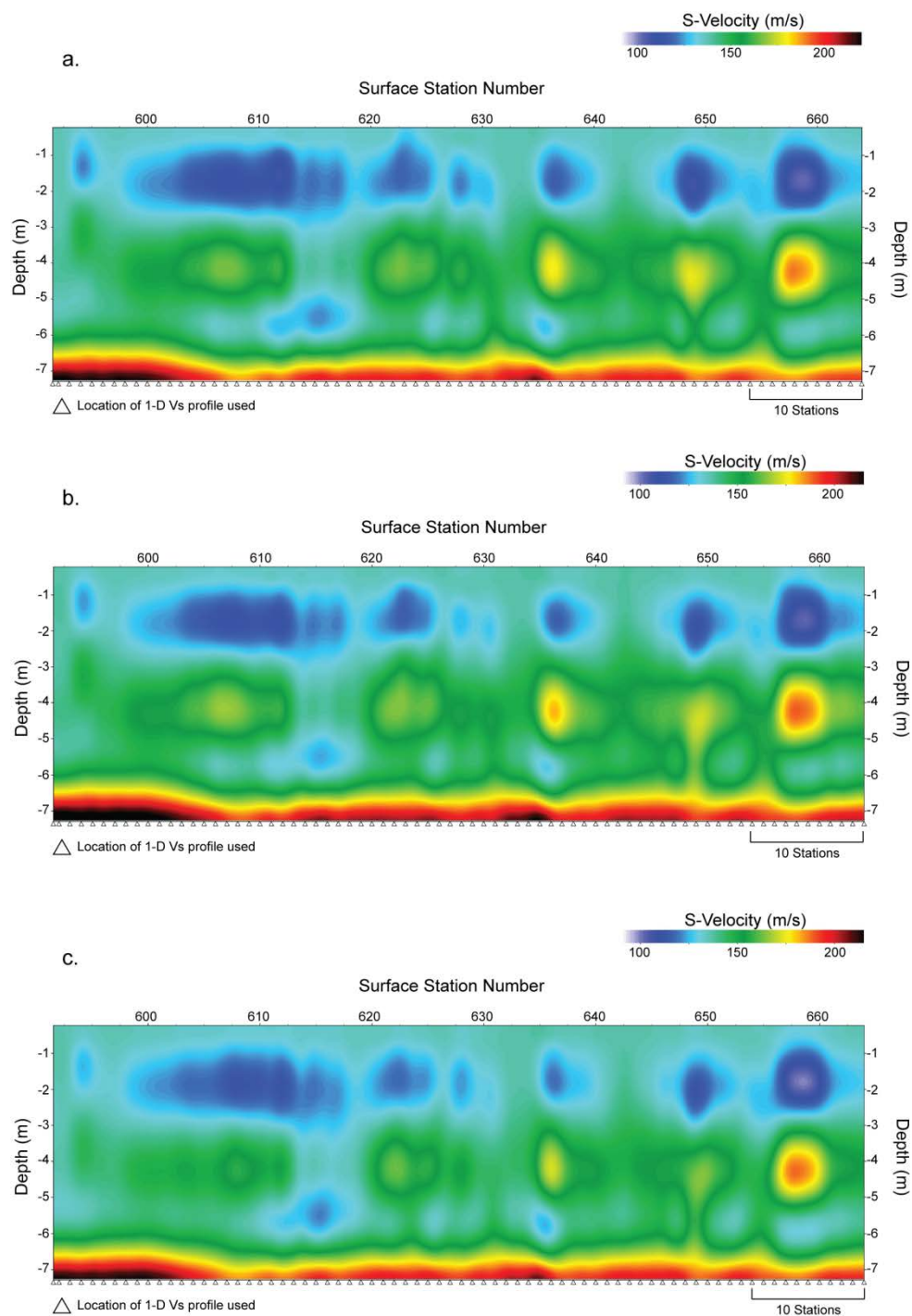


Figure 3-14. New Brighton Beach inversion results with a constant Poisson ratio = 0.4, and different densities provided in the initial model. (a) with $\rho=1700 \text{ kg/cm}^3$ in the initial model, (b) $\rho=2000 \text{ kg/cm}^3$, and (c) variable density.

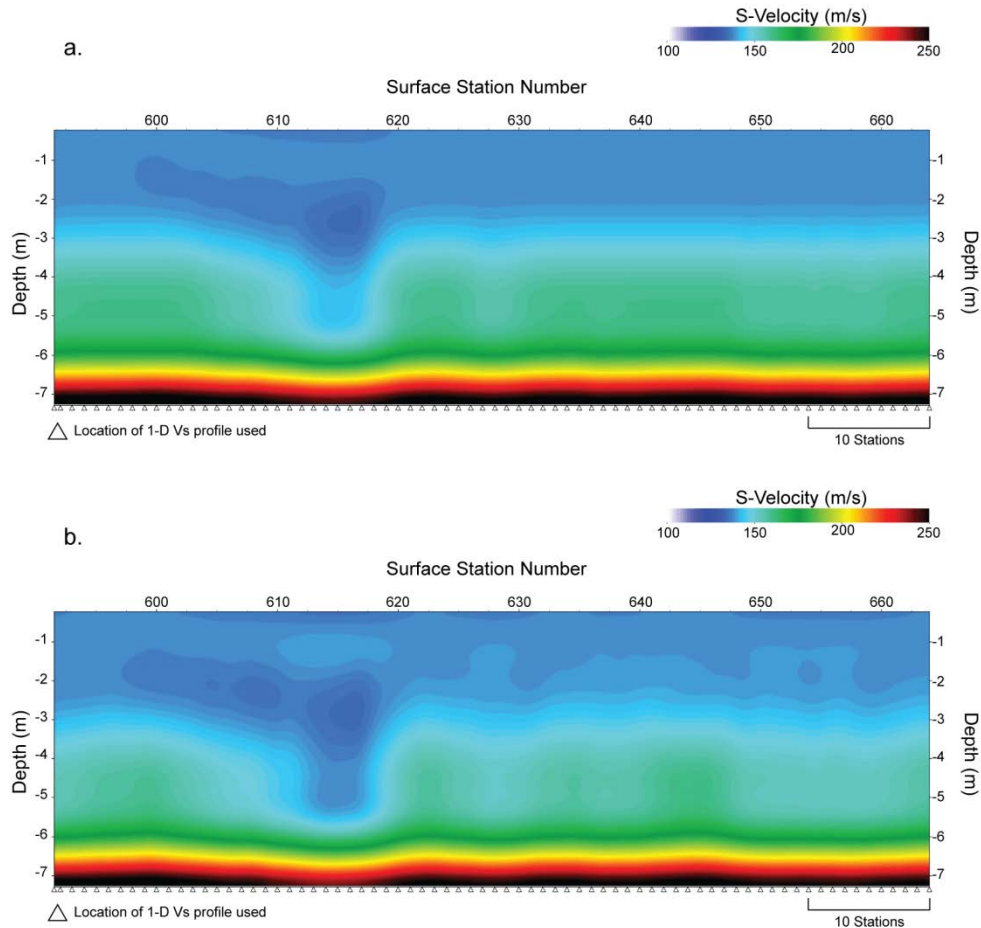


Figure 3-15. New Brighton Beach inversion results with Poisson ratio = 0.15 provided in the initial model. (a) with $\rho=2000 \text{ kg/cm}^3$ in the initial model, (b) variable density.

A fixed Poisson ratio of 0.15 was also tested, shown to be the measure in shallow unconsolidated beach sand (Bachrach et al., 2000). The fixed Poisson ratio was examined with a fixed density of 2000 kg/cm^3 , and a variable density of 1550 to 2000 kg/cm^3 with depth in two separate initial models. By changing the fixed Poisson ratio in the initial model, V_p is also updated (see Table 3-3, initial model parameters with fixed Poisson ratio of 0.15 and variable density). Inversion results (Figure 3-15) shows a more laterally

continuous Vs model with slightly higher velocities (with an increase of approximately 8%) compared to using a fixed Poisson ratio of 0.4. The S-wave velocity in the top 2.5 m is approximately 140 m/s and increased to 150 m/s at 3 m depth. From 3.5 – 6 m, velocities increase to approximately 160 m/s, and then quickly increase to 250 m/s at 7 m depth. A decrease in velocity is seen again near station 615. RMSE remained low for all of the models, in the span of 1 – 2 m/s. After further investigation, the fixed Poisson ratio of 0.4 (results from Figure 3-14) is taken to be a more accurate representation of the true of Poisson ratio, since Poisson ratio of 0.15 is given for dry sand, and the sand at the investigation site is damp to saturated.

3.4.2 Highfield Road (Line 3)

3.4.2.1 Data processing

Records with FFID 306 – 610, comprising 304 shots and a total distance of 3040 m were processed in ProMax for later surface wave analysis in SurfSeis. AGC was applied with a 1000 ms sliding time window. Raw data and data with AGC applied are displayed in Figure 3-16, with a peak frequency of 30 Hz shown in the amplitude spectrums. A maximum frequency 30 Hz low pass RT domain filter (Henley, 2003) with a radial trace velocity of ± 2700 m/s was applied to increase signal-to-noise of the surface waves. Figure 3-17 shows shot record 380 before (Figure 3-17a) and after (Figure 3-17b) RT domain filtering. The airwave and P-wave reflection events are mostly discarded (Figure 3-17c) in the low pass filter. A bandpass filter of 1-4- 25-32 Hz and a top mute was applied, and the shots were sorted to off-end geometry, with receivers on the right side of the shot.

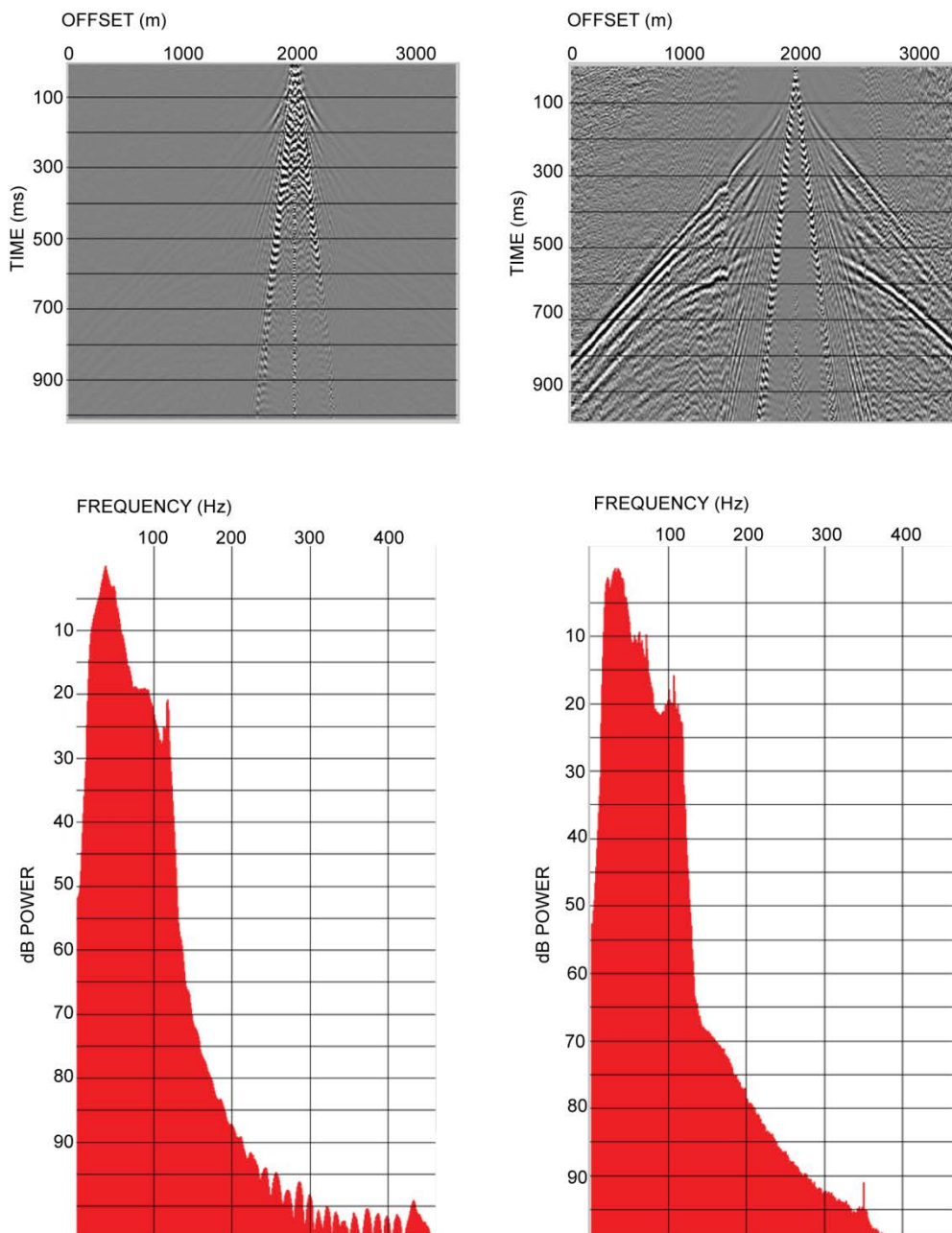


Figure 3-16. Raw shot record and frequency content from Highfield Road on left hand side. With AGC applied on right hand side. This dataset has a peak frequency of 30 Hz.

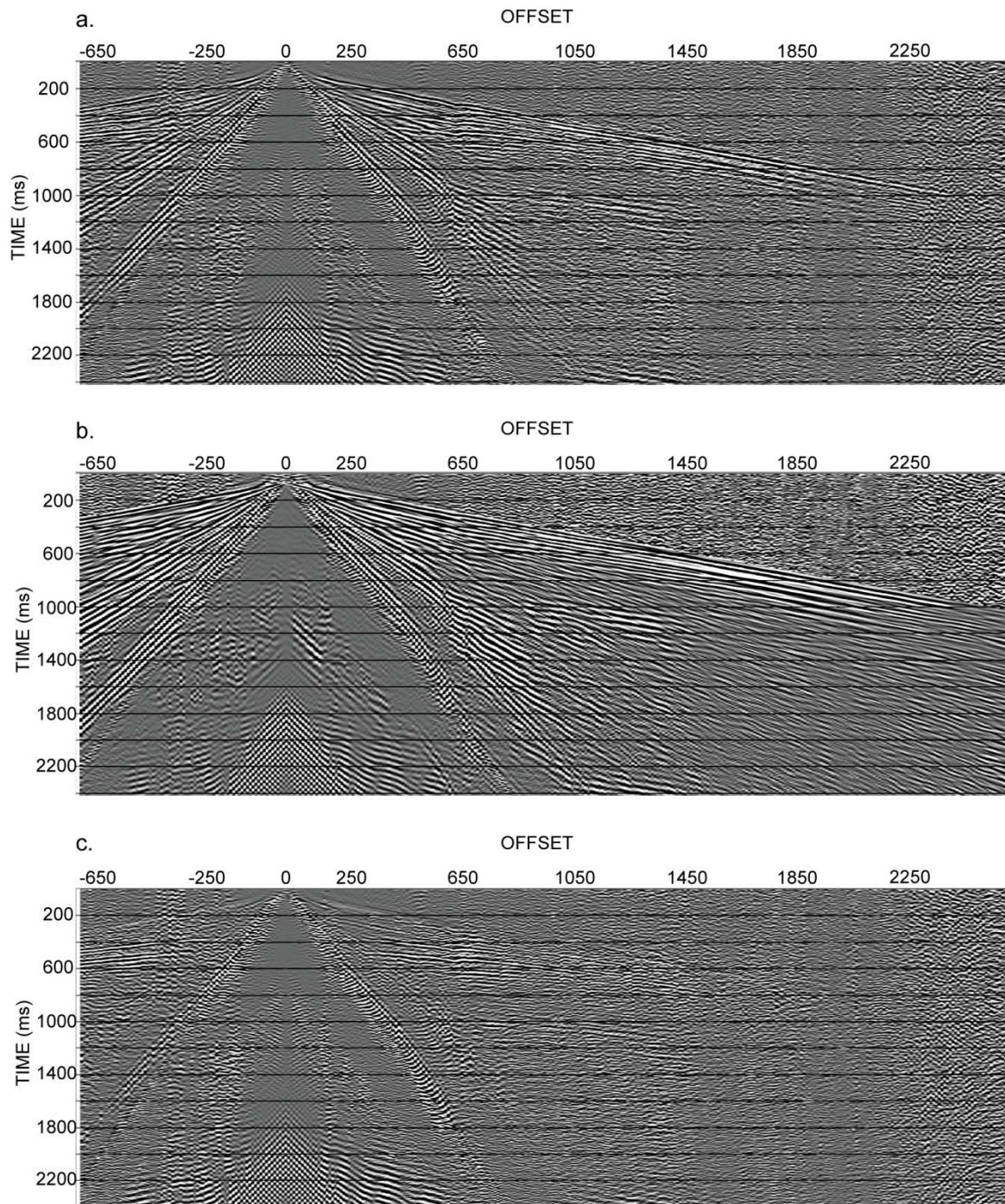


Figure 3-17. (a) Raw shot record before RT domain filtering, (b) after RT domain filtering, and (c) airwave and signal discarded from the RT domain filter.

3.4.2.2 Dispersion Curve Analysis

The processed shot gathers were converted from SEG Y to KGS format in SurfSeis 3.15 and geometry was applied. Dispersion images were refined by selecting the optimum estimation of phase velocity and frequency range. Smaller offsets produced an improved fundamental mode, as the dominance of higher modes increases with offset (Park et al., 1999). Spread lengths of 1940, 1000, 500, and 300 m were tested in producing the dispersion images (Figure 3-18), where fundamental mode resolution was best enhanced with a spread length of 300 m. As an additional analysis, data with a maximum frequency 15 Hz low pass RT domain filter was compared against data with the 30 Hz low pass RT domain filter and transformed to dispersion images. It was found that both datasets resulted in comparable dispersion curves with a fundamental mode ranging from 13 to 28 Hz for 480 to 520 m/s (Figure 3-19).

The fundamental mode was generally straightforward to pick, until seismic traces near the fault were evaluated within the spread length for dispersion image analysis. For example, the fault occurred near station 440. With 10 m station spacing and a spread length of 300 m, traces from the fault would enter the region for analysis at station 410. From stations 410 – 441, the phase velocity of the fundamental mode is highly scattered, resulting in dispersion curves with low signal-to-noise ratios unsuitable for inverting the S-wave velocity profiles. The dispersion image at station 417 is shown in Figure 3-20. A blue trend line with small squares shows where the curve had been previously picked prior to emergence of the fault zone within the analysis area. The dispersion images remain scattered until the fault is cleared of the analysis zone.

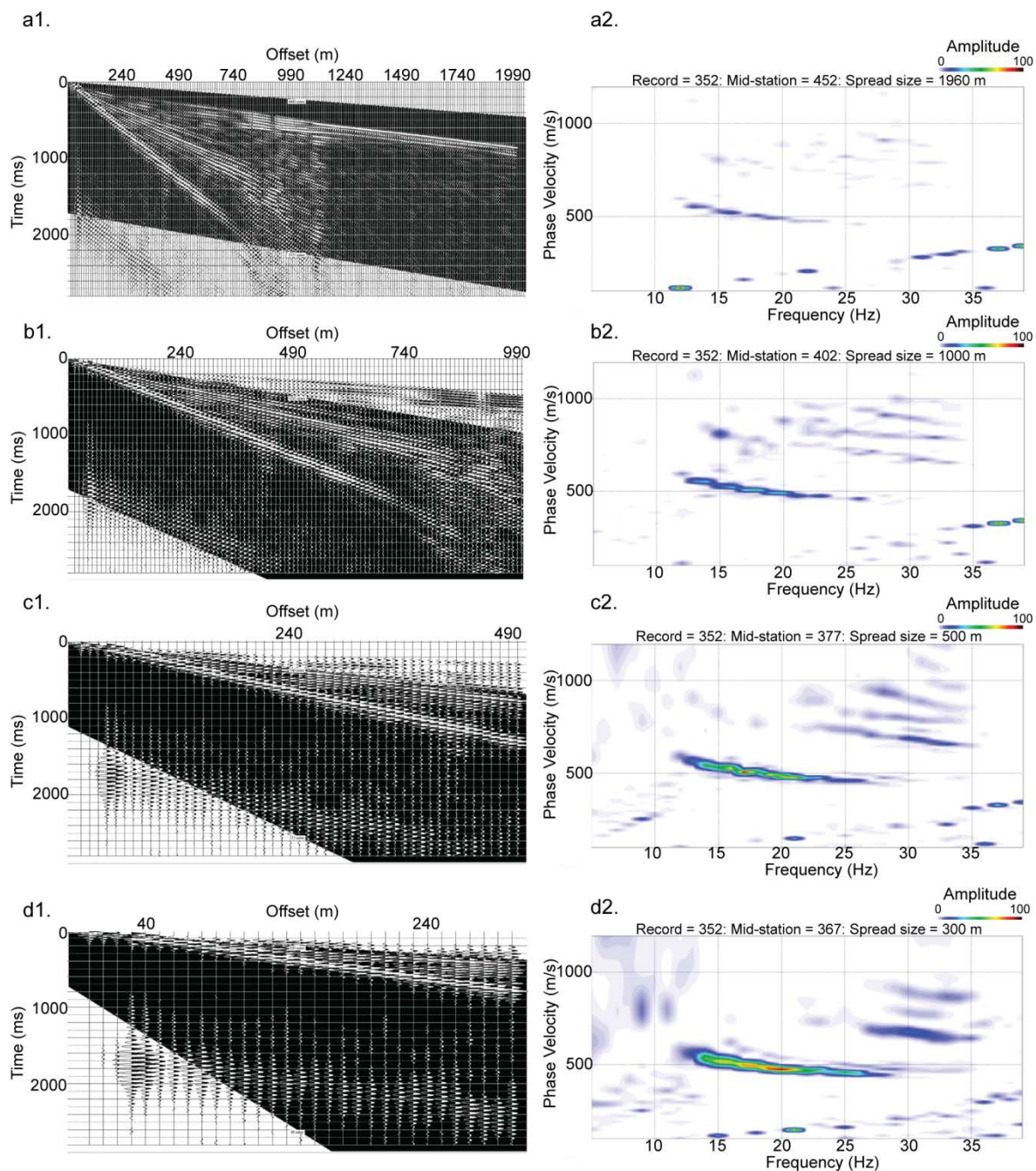


Figure 3-18. Spread lengths of (a) 1940, (b) 1000, (c) 500, and (d) 300 m were tested in producing the dispersion images. The fundamental mode resolution was best enhanced with a spread length of 300 m.

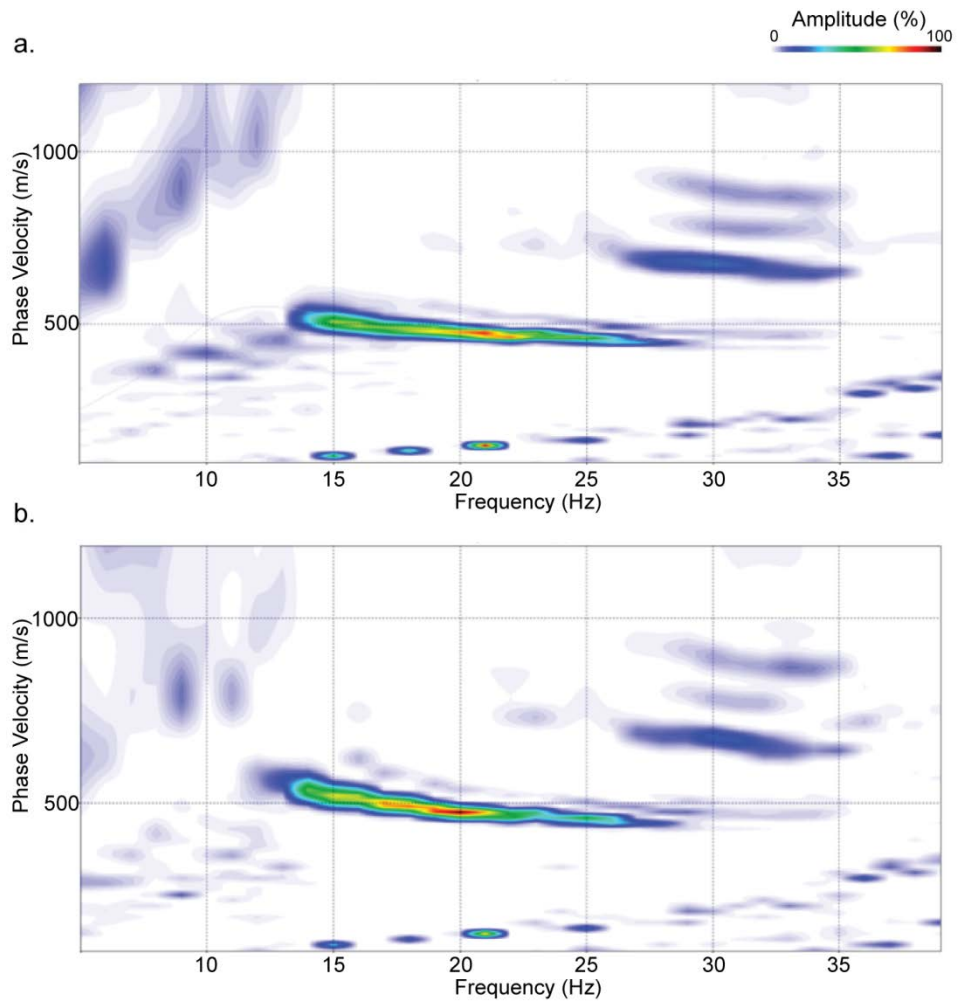


Figure 3-19. Dispersion curve comparison between input data with (a) a maximum frequency 30 Hz low pass RT domain filter, and (b) a maximum frequency 15 Hz low pass RT domain filter. The frequency of the fundamental mode ranges from 13 to 28 Hz.

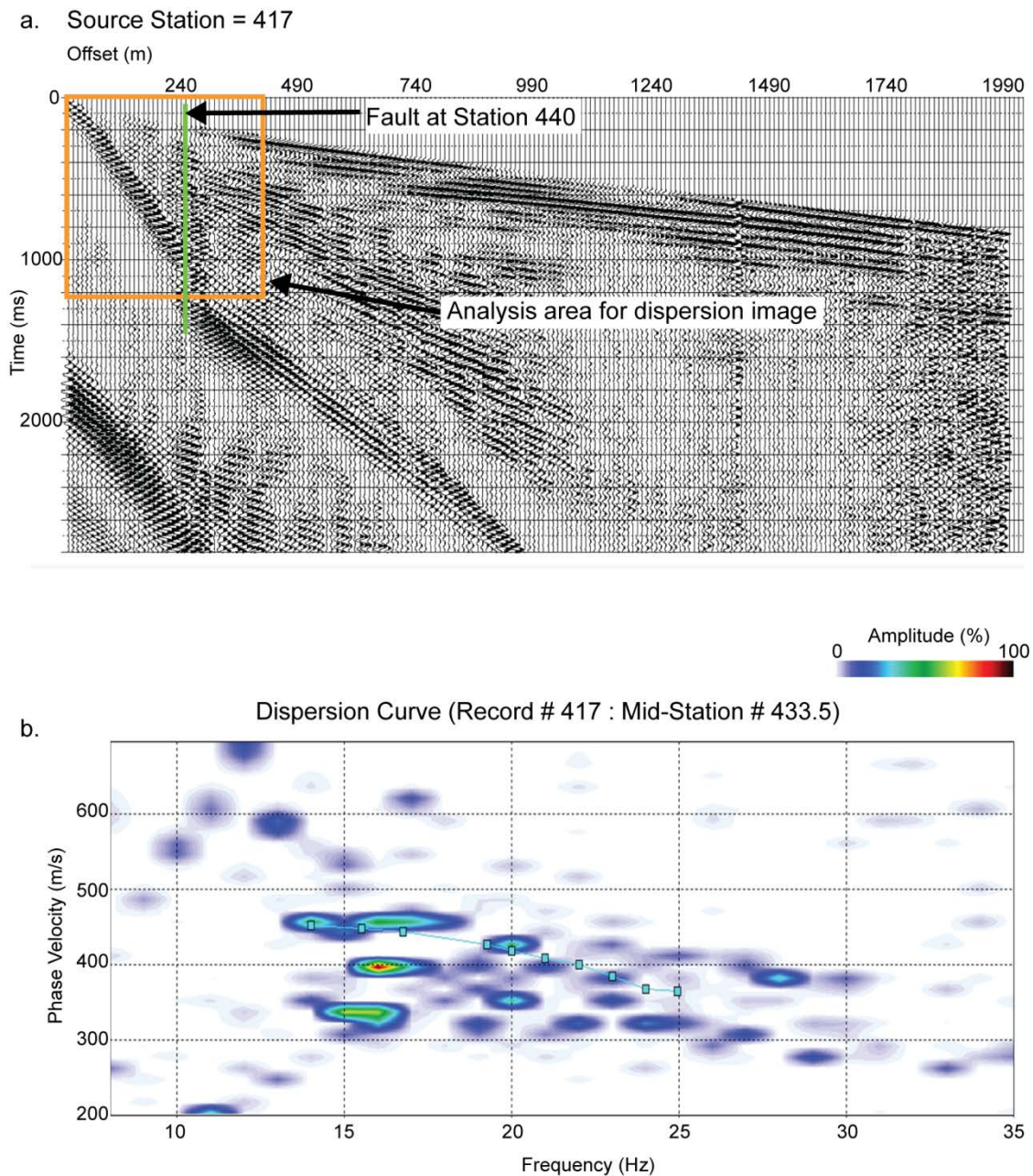


Figure 3-20. (a) Shot record at Station 417 used for dispersion curve analysis. The analysis area and fault location are highlighted (b) Resulting dispersion image approaching the Greendale Fault. Amplitudes are high scattered and have low S/N ratios. The blue trend line with small squares shows where the curve had been previously picked prior to emergence of the fault zone within the analysis area.

3.4.2.3 Inversion Analysis

The final S-wave profiles for three locations before (Record 321), near (Record 417), and after the fault zone (Record 550), are shown in Figure 3-21. The Vs curve (blue dashed line) from the initial model is shown with the Vs curve of the final inversion result (solid blue line). The extracted dispersion curve picks are plotted solid black circles, representing the measured fundamental mode. An initial model was created from a 10 layer fixed Vs model with variable density, and was based on station 369 with a 60% signal-to-noise ratio. The parameters for the initial model are shown in Table 3-4. A fixed Poisson's ratio of 0.4 was chosen, as Poisson's ratios close to the acoustic limit of 0.5 are typical of unconsolidated near-surface sediments (Roth and Holliger, 1999). The Vs curves from the initial and final models are in good approximate agreement with the measured fundamental mode for the nearest record to the layered initial model (Figure 3-21a), with the exception in the lower frequency (< 18 Hz) range, however, there is improvement in the final model. The initial model was updated 9 times until the final model was reached. The initial model provided better results in some areas, specifically in the 20 – 23 Hz range for stations near and past the fault zone increase, as seen in Figure 3-21 b and c. Each of these initial models was updated to the maximum iteration limit set (12 times for this dataset) until the final model was reached. The profiles reach depths of approximately 15 m. The inversion process is described in greater detail in sections 3.2.3 and 3.4.1.3.

Table 3-4. Initial model for 10 layers, variable density, and a fixed Poisson ratio of 0.4

LAYER	BOTTOM (m)	THICKNESS (m)	V _S (m/s)	V _P (m/s)	PR	DENSITY (kg/cm ³)
1	0.505	0.505	503	1233	0.4	1550
2	1.137	0.632	503	1233	0.4	1600
3	1.927	0.790	503	1233	0.4	1650
4	2.915	0.987	503	1233	0.4	1700
5	4.149	1.234	503	1233	0.4	1750
6	5.691	1.543	503	1233	0.4	1800
7	7.620	1.928	518	1269	0.4	1850
8	10.03	2.410	552	1351	0.4	1900
9	13.043	3.013	585	1433	0.4	1950
10	Half Space	Infinity	905	2216	0.4	2000

The final S-wave velocity model and associated RMSE is shown in Figure 3-22. The RMSE provides an indication of where the inversion results are unreliable; that is, a sudden increase in RMSE occurs south to north from Station 410 to 440 as the fault zone is approached. Most of the velocity model (top 12 – 15 m) shows average S-wave velocities of approximately 500 m/s. There is a decrease in velocity (300 -350 m/s) in the region approaching the fault zone, and to the north of the fault past Station 560. Additional initial models were tested including a layer model based on Station 525 (with a 70% signal-to-noise ratio), and a 5-layer model with fixed density, however, final S-wave model results were analogous to the final model shown.

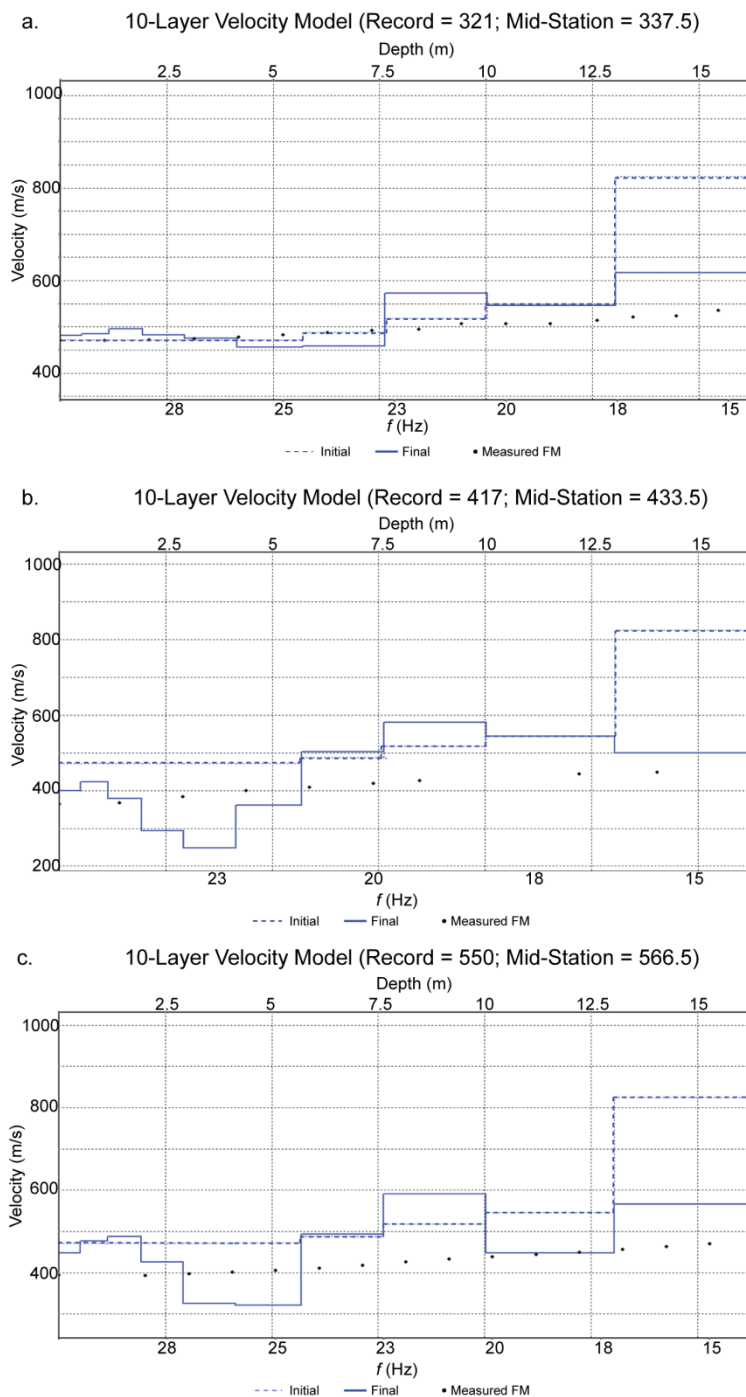


Figure 3-21. The final S-wave profiles for three locations before (Record 321), near (Record 417), and after the fault zone (Record 550). Initial V_s measurements (blue dashed line) from the initial model is shown, with the final V_s inversion result (solid blue line). The extracted dispersion curve picks are plotted solid black circles, representing the measured fundamental mode.

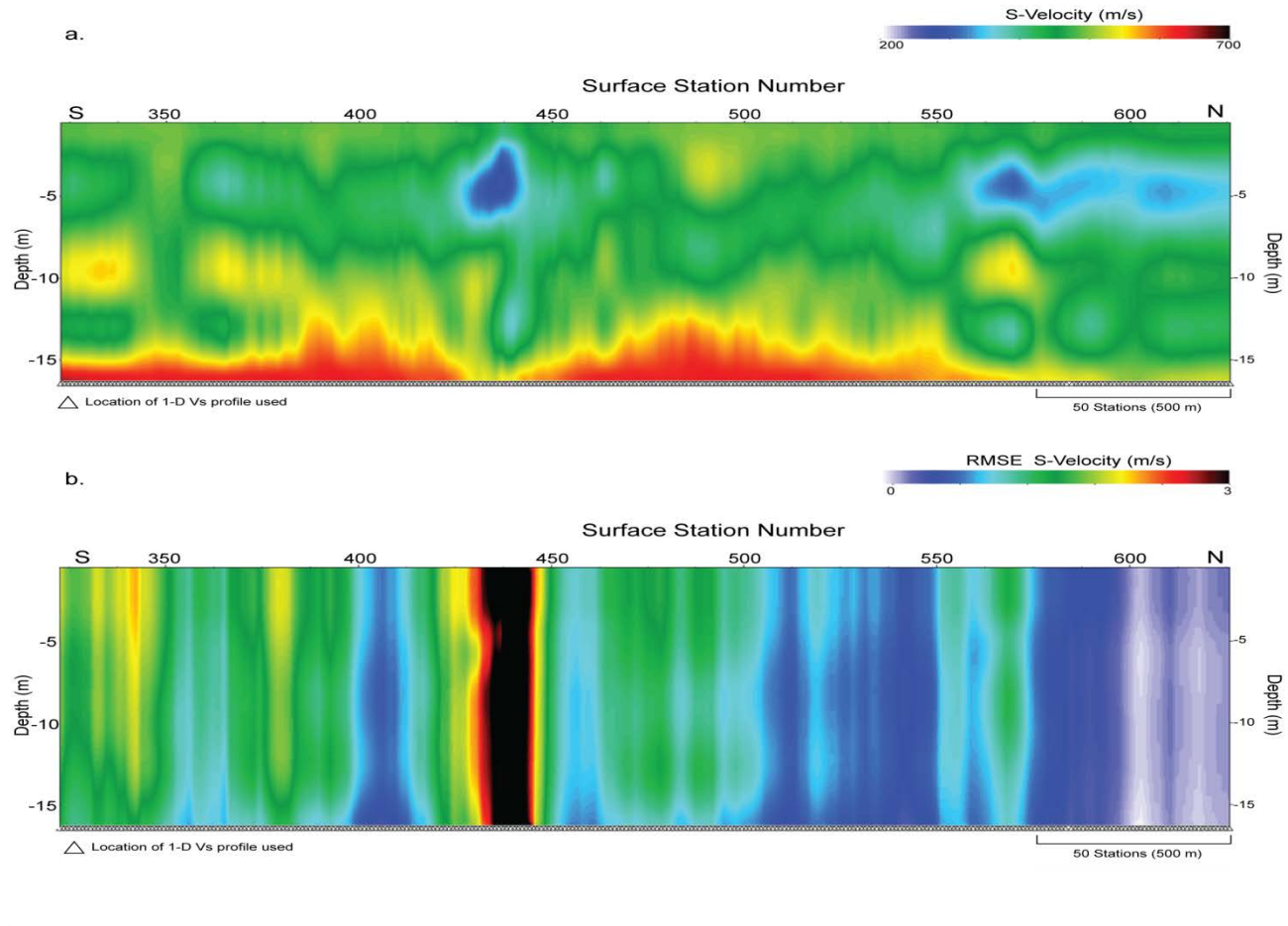


Figure 3-22. (a) The final S-wave velocity model for Highfield Road, and (b) associated RMSE. The RMSE provides an indication of where the inversion results are unreliable.

3.5 . Discussion

The discussion presented here is quantitative in terms of S-wave velocity. The shear strength of a material, also described as stiffness or rigidity, is directly related to S-wave velocity. As V_s increases, material shear strength also increases (Ivanov et al., 2011). Also discussed are properties tested in the initial model for inversion, such as density. More information is required to provide reliable interpretation of the MASW results; therefore this discussion is more or less restricted to observations of the results, with possible interpretations.

3.5.1 Discussion of New Brighton Beach results

The New Brighton Beach results (Figure 3-14) show that experimenting with density in the initial model does not have a great effect on the inversion results. Densities examined are 1700 kg/cm^3 , 2000 kg/cm^3 , and variable density ranging from 1550 to 2000 kg/cm^3 with depth. The minor change between the inversion results is expected. Xia et al. (1999) showed that a 25% error in density results in an average relative change in phase velocity of $< 10\%$. Also, a 25% error in P-wave velocity results in $< 3\%$ change in the phase velocity. The most important property for the inversion of fundamental mode dispersion data is S-wave velocity.

Inversion results of New Brighton Beach (Figure 3-23a) show low ($< 200 \text{ m/s}$) S-wave velocities for the total thickness of 7 m, which indicate very loose soil and validate the geologic setting. A shallow setting is investigated, since velocity is slow and wavelength is proportional to velocity. The top 3 meters show velocities of approximately

130 m/s with pockets of slower velocities approaching 100 m/s, which are underlain by areas of higher velocities. The pockets of lower velocity material in the top 3 m indicate areas of lower shear strength, or lower rigidity and are indicated by the dashed line on the figure. The soil becomes slightly stiffer with depth in the 3 – 6 m range where velocities increase to 175 m/s in some areas. The surface sand was damp, and water table levels are less than 0.9 m, as indicated by Environment Canterbury well M35/7753.

A possible explanation for the pockets of lower velocities approaching 100 m/s in the 1 – 3 m range could be an indication of slightly overpressured sands, and underlying higher velocities could indicate an increase in clay content. If there is an increase in pore pressure along the beach coastal slope, it could be a result of (Xiao et al., 2010):

- i) An earthquake, where progressive pore pressure builds up due to a reduction of pore space caused by cyclic loading.
- ii) Water wave interactions, where transient pore pressure buildup often occurs around coastal sandy slopes.

However, either scenario could result in liquefaction. Even cohesionless materials (i.e. dry or fully saturated sand) have strength as a result of particle interlocking and friction at grain contacts, and are therefore at risk for liquefaction (Owen, 1987).

It is also interesting to acknowledge the results of an MASW investigation entitled Bexley North (Tonkin and Taylor Ltd., 2011) located on the west banks of the

Avon river approximately 800 m to the west from the MASW investigation of New Brighton Beach of this study. The Bexley North MASW survey was acquired by Southern Geophysical Ltd. for Tonkin & Taylor Ltd, and prepared for the Canterbury Earthquake Commission (EQC), a New Zealand Government agency. The top 7 meters of the profile show slow velocities in the 130 m/s range. A band of even slower velocities of approximately 100 m/s is apparent between 4-6 m depth. These are comparable to velocities encountered along New Brighton Beach.

A shallow seismic experiment study in sand by Bachrach et al. (1998) shows the complexity in acquiring shallow seismic data in low-velocity settings with high velocity gradients. The study recommends very small receiver spacing to avoid spatial aliasing of signal and ground roll in shallow low velocity environments. Smaller receiver spacing would also result in a finer sampling of 1D S-wave velocity profiles to provide better resolution in the final velocity model.

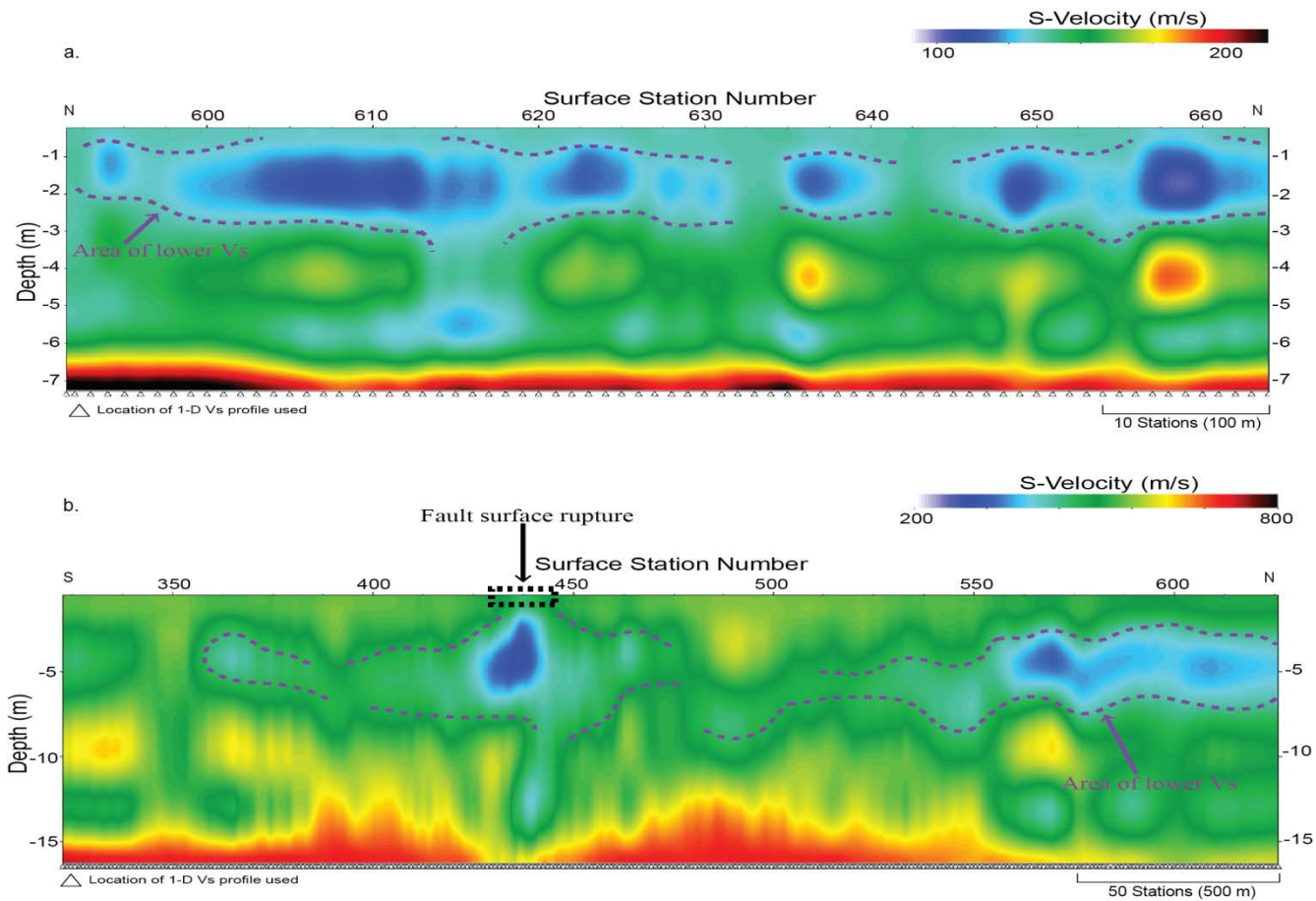


Figure 3-23. S-wave velocity inversion results for (a) New Brighton Beach, and (b) Highfield Road. Dashed lines indicate areas of lower S-wave velocity. Overall lower shear wave velocities are observed at New Brighton Beach.

3.5.2 Discussion of Highfield Road results

The claybound gravels at the Highfield road site resulted in more noise overall in the seismic data. The S-wave velocity is approximately 500 m/s for the top 12 – 15 m of the final model, with lower velocities (300 -350 m/s) in the region approaching the fault zone and to the north of the fault past Station 560. The most notable feature of the MASW investigation at this site was the approach towards the Greendale Fault. A low quality dispersion curve with intense back scattering was shown in Figure 3-20b, and represent the type of low signal-to-noise curve that was encountered in dispersion curves from stations 410 – 441. Low quality dispersion curves continue until the fault is absent from the analysis zone, following station 441.

The scatter or diffractions of seismic waves, or lateral changes in seismic properties can infer the presence of a fault zone (Ivanov et al., 2006). Areas with voids, near-vertical faults, or vertical surface structures can produce reflected ground roll and noise which contaminates Rayleigh wave dispersion curves (Xia et al., 2000a). Backscatter due to a fault zone in MASW dispersion curves have been observed in other studies (Ivanov et al., 2006; Duffy, 2008), however more severe backscattering is shown in this study. Possible reasons for greater backscattering in this case could be that the Greendale Fault was a surface rupture, so lateral variation and backscattering encompassed a larger vertical zone which reached to the surface. Also, the gravels could be contributing to more backscattering. Another point which should be made is that AGC was applied to this dataset prior to dispersion curve analysis. It was thought that applying

AGC would balance trace amplitudes in a sliding window and correct for attenuation; however AGC could have enhanced scattering noise in the gravel environment.

Backscattering from the fault zone would have occurred at fewer stations in the MASW investigation if a shorter spread length was chosen. However, a longer spread length was chosen for this dataset for two reasons: spatial aliasing of ground roll was apparent on the near offsets therefore a longer spread length was selected to include more data for analysis; and receiver station spacing was 10 m which resulted in fewer traces for analysis, so a longer spread length was selected in order to include more traces.

A low velocity lateral trend is observed in Figure 3-23b through most of the line around 4 to 6 meters depth (indicated by a dashed line), with lower velocities near the fault and on the northern end of the seismic line, over 1700 m away from the fault. It is not surprising to see lower velocities or less rigid soil parameters at larger distance from the fault, as the effect of liquefaction, lateral spreading, and damage from the Darfield earthquake was observed to occur in the city of Christchurch, 40 km east of the Darfield earthquake epicenter (Orense, 2011). However, lower velocities expected from the near-vertical fault itself (located near station 440) are subtle.

Chapter Four: **SEISMIC PHYSICAL MODELING OF AN ACTIVE FAULT ZONE**

4.1 Introduction

This chapter investigates fault detectability by seismic physical modeling, and compares the results to seismic field data acquired transversing the surface ruptured Greendale Fault in New Zealand. The deformation of rocks near the fault zone causes changes in lithology, pore pressure, and seismic velocity (Mooney and Ginzburg, 1986).

4.1.1 Physical modeling background

Seismic physical modeling provides scaled simulations of real-world scenarios with the benefit of controlled acquisition geometry and physical model properties (Lawton et al., 1998). Modeling of simple faults and geometries are beneficial to understand seismic sections with faults and structure (Angona, 1960). Hilterman (1970) used wood and paper to model synclines, anticlines, and vertical and low angle faults. An electric spark and a condenser microphone served as a source and receiver in this early experiment. Modeled seismic data collected in a water tank has shown success in comparing data processing and imaging between 2D and 3D datasets of ridge and fault models (French, 1974).

4.1.2 Seismic resolution theory

The quality of seismic imaging over a fault zone is constrained by seismic resolution. Both vertical and lateral resolution is controlled by spectral bandwidth, and describes the ability to distinguish separate features (Yilmaz, 1987, p. 468). Spectral

bandwidth is defined as the standard deviation about the spectral mean, or the center frequency (Barnes, 1993).

4.1.2.1 Vertical resolution

Vertical resolution is important in imaging the vertical throw of a fault. Vertical seismic resolution is defined by Widess (1973) as the thickness equal to one eighth of the dominant seismic wavelength. Dominant wavelength varies with velocity and dominant seismic frequency, and is given by:

$$\lambda = \frac{v}{f} \quad (1)$$

where λ = wavelength, v = velocity, and f = frequency. As an industry standard, one quarter of the predominant wavelength is taken for thin bed vertical resolution as the Widess threshold does not account for noise and wavelet broadening due to attenuation of higher frequencies with depth.

4.1.2.2 Lateral resolution

Lateral resolution threshold is determined by the Fresnel zone (Figure 4-1), an area of constructive reflection accumulation surrounding a reflection point (Lindsey, 1989). The radius of the Fresnel zone is given by the approximation:

$$r \cong \left(\frac{v}{2}\right) \sqrt{\frac{t}{f}} \quad (2)$$

where r = radius of the Fresnel zone, v = velocity, t = time, and f = frequency. Two reflecting points that fall within the Fresnel zone are considered irresolvable, therefore lateral resolution improves as the Fresnel zone narrows. The deformation zone of

shallower faults is more resolvable than deeper faults, as the Fresnel zone increases in area with depth.

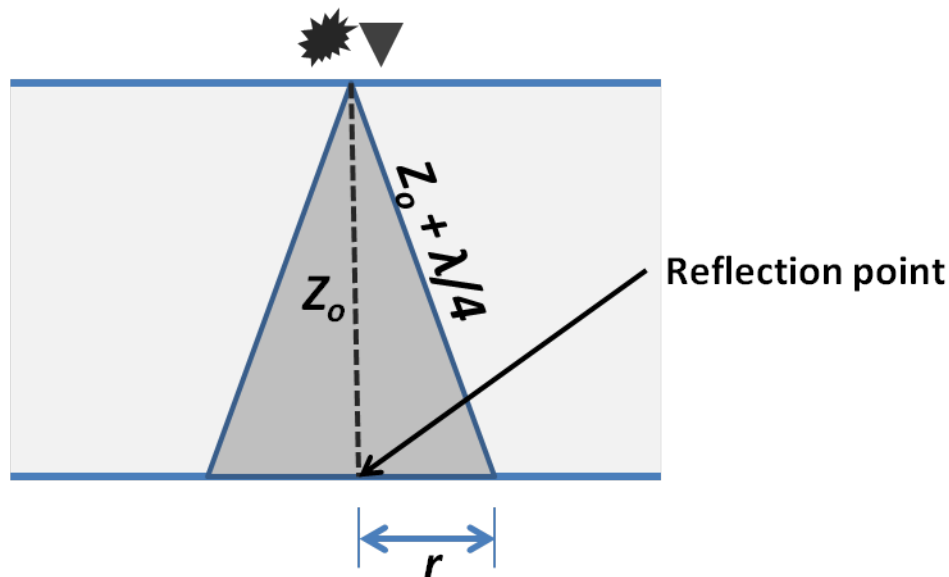


Figure 4-1. The Fresnel zone radius (r) for a coincident source and receiver. Adapted from Yilmaz (1987).

4.2 Physical modeling

4.2.1 The physical models

The displacement and deformation zone of the Greendale Fault, which was ruptured during the 2010 Darfield earthquake, served as the inspiration in creating the fault models. The Greendale Fault surface rupture was mainly dextral strike-slip with 2.5 m average displacement, vertical displacement less than 0.75 m, and a 30 to 300 m wide deformation zone (Van Dissen et al., 2011). Pure strike slip faults are difficult to detect in seismic imaging due to lack of significant vertical displacement (Fossen, 2010, p.356). However, deformed bends associated with strike-slip faults may split and widen upward into flower structures, which may be more detectable in seismic imaging as there is a

wider fault zone in the near surface. Fault zones also show reduced seismic velocities which are associated with densely cracked and fractured rocks, altered rock composition, and near-surface fault gouge material (Mooney and Ginzburg, 1986).

Given these considerations, several physical model prototypes were constructed to best represent a vertical fault that ruptures the surface. A fault zone was created, closed at one end of the model fault length, and widens with fault length distance. Several types of materials are used to create the models and are summarized in Table 4-2. The velocities of the materials were measured with a Tektronix TDS 420A 200 MHz 4 Channel Digital Real-Time Oscilloscope. All of the models had 2D zero-offset seismic reflection surveys acquired as a quality check. Survey parameters are discussed in greater detail in section 4.2.2.

Table 4-1. Summary of physical model prototypes

			Density (g/cm ³)	Measured Velocity (m/s)
Model 1	Model Material	Plaster of Paris	1.3	2035
	Fault Zone Infill	Lard	0.98	1490
Model 2	Model Material	Sandstone	2.6	2965
	Fault Zone Infill	Epoxy	1.7	2680
Model 3	Model Material	Limestone	2.9	5100
	Fault Zone Infill	Wax	1.1	1510
Model 4	Model Material	Limestone	2.9	5100
	Fault Zone Infill	Water	1.0	1480
Model 5	Model Material	Limestone	2.9	5100
	Fault Zone Infill	Liquid acrylic	1.2	2460

The model and seismic acquisition measurements are scaled, where 1 mm in the physical modeling world is equivalent to 10 m in field equivalents (1:10000). Ultrasonic modeling frequencies of 100 kHz to 1,000 kHz are scaled down by the scaling factor of 10,000 to represent real-world seismic frequencies of 10 Hz to 100 Hz. All referred measurements are scaled to represent field values and measurements have an approximate error of 5%.

The Plaster of Paris-Lard model (Model 1) has an average thickness of 285 m. Issues arose with this model as a result of air bubbles setting in as the plaster dried, and

the lifespan of the model was limited as the seismic surveys were acquired in water. The Sandstone-Epoxy model (Model 2) has an average thickness of 248 m and one side was uplifted by 30 m. The epoxy had set too quickly and only a constant width fault gap width of 30 m was created. An additional model was created with Portland cement using coarse grained sand. The model was sturdy; however scaled grain sizes of the rock would be equivalent to 5 m. These unrealistic grain sizes contribute to point scattering in a seismic reflection survey. The limestone model (Model 5) with an average thickness of 300 m, showed greatest promise as potential modeling material.

An assortment of fault-zone infill materials was tested: water, lard, wax, epoxy, and finally acrylic plastic. A material was sought which had a lower velocity than the model material to best represent a fault zone, and a velocity higher than paraffin wax and lard, which was close to the velocity of water. The epoxy used with the sandstone had a higher velocity of 2680 m/s, however, it set much too quickly, making it difficult to work with. The final fault infill material selected was a liquid acrylic (2460 m/s) which sets to a hard resin. The limestone model was fixed in place with putty, and sealed with wax to prevent leakage. The model was also uplifted on one side by approximately 10 m. At this point in the study, the limestone models with both a water-filled and acrylic-filled fault zone were considered optimal, and the results are compared in further analysis.

4.2.2 Physical modeling data acquisition

The University of Calgary Seismic Physical Modeling Facility supports both acoustic and elastic modeling. For this study, only the acoustic modeling is considered.

Dynasen Inc. CA1136-12 piezoelectric pin transducers (305 mm long and 24 mm diameter) acting as an acoustic source and receiver are carried in a carriage attached to a beam which moves along aluminum tracks. The transducers produce and detect vibrations with particle motion in the vertical direction (Wong et al., 2011). The modeling systems are described in further detail by Cheadle et al. (1985), Lawton et al. (1989), Gallant et al. (1991), and Wong et al. (2009a).

The physical models were immersed in a water tank for seismic acquisition modeling. Each model was placed on top of an aluminum plate, which rested on a phenolic resin block. A schematic of the Limestone model in the tank is shown in Figure 4-2. The models were placed in the tank with the fault length parallel to the N-S direction of the room, representing the x-axis, with the thinner end of the fault in the positive x-axis direction (Figure 4-3). A zero-marker was placed on all the models for coordinate reference and was located approximately 120 m East of the fault (Y=+120).

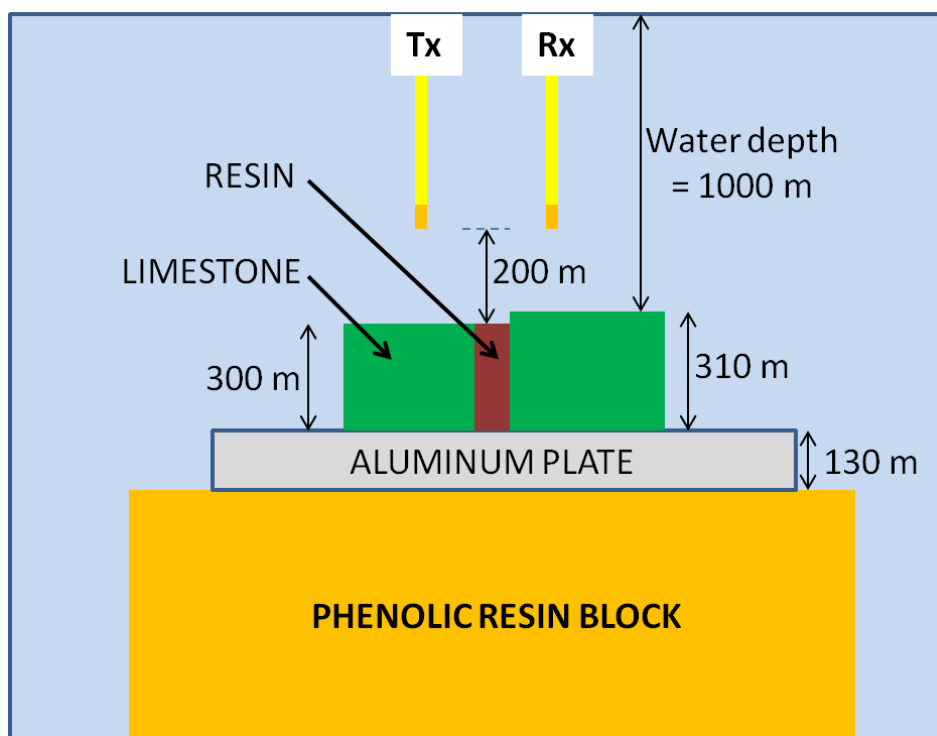


Figure 4-2. Schematic diagram of seismic acquisition over the final limestone model with corresponding field dimensions. The transducers are positioned 200 m over the model.

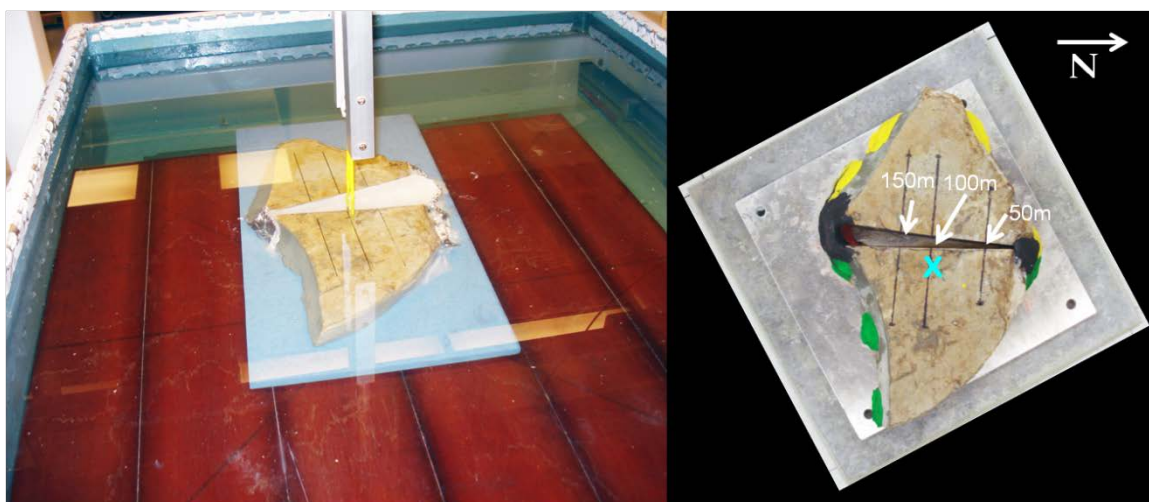


Figure 4-3. The Limestone-Wax model in the physical modeling water tank (left), and the limestone model (right), held in place by putty prior to fault zone infill. The blue 'x' signifies the zero marker location.

A zero-offset section, acquired by a coincident source and receiver which step along the seismic profile, was acquired for quality control of all the models to determine suitability for further investigation. Although the transducers were not exactly coincident due to the carriages, they are near-offset, with a spacing of 5 m (50 m, scaled), and the data are processed assuming a coincident source and receiver. The zero-offset profiles ran perpendicular to the fault length along the y-axis, with the transmitter-receiver pair moving in 5 m increments with a 50 m offset in line with the fault (Figure 4-4). Three profiles were collected over each model at varying fault zone thicknesses. For the final limestone models, the surveys ran from $Y=-700$ to $Y=+900$ (321 traces), and crossed fault zone widths of 50, 100, and 150 metres.

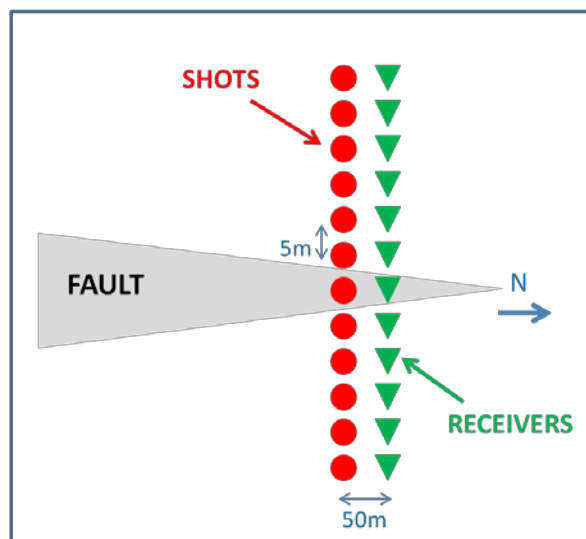


Figure 4-4. Plan view of the zero-offset acquisition. The Tx-Rx pair moved in 5 m increments and have 50 m offset.

Common-source gathers were acquired for the Limestone models over the 50 m fault width. The survey for the Limestone models ran from $Y=-300$ to $Y=+700$. The source increment spacing was 10 m, and 101 shots were collected perpendicular across

the fault length. The receiver spacing was 5 m and 201 traces were collected in each shot gather. A sample rate of 1 ms (scaled units) was used during all acquisition. For comparison with the common-source data, only the zero-offset data from the 50 m fault gap will be discussed.

4.3 Seismic data processing

The seismic data was initially viewed in SeiSee 2.16.1 for quality control, and then processed in GEDCO's VISTA seismic data processing software. Two processing flows were developed: a processing flow for the zero-offset data, and a flow for the common-source data. The flows created in VISTA are shown Appendix E. A general description of the processing flows is discussed in this section; however, there may have been some modification in processing parameters to best fit each dataset.

4.3.1 Zero-offset data processing

A zero offset time section provides an image of data traces which have an equivalent source-to-geophone distance. In this case, the offset distance is 5 mm (or 50 m, scaled) and the source-receiver pair increment is 0.5 mm (5 m, scaled). The benefit of acquiring zero offset data is that minimal processing is required to obtain an image of the subsurface. The general processing flow used to image the zero offset data is given in Figure 4-5, with the goal of providing a clear image of the surface fault. To illustrate examples, this discussion will be limited to the top 1 s of the Limestone-Acrylic model data.

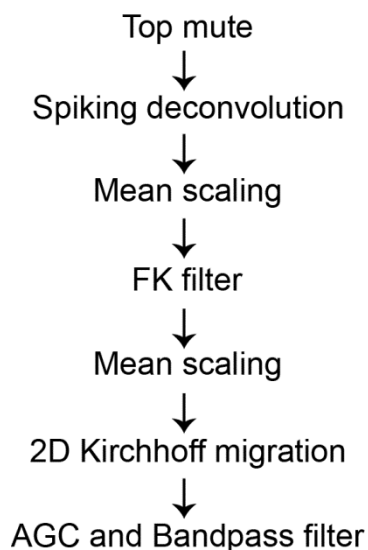
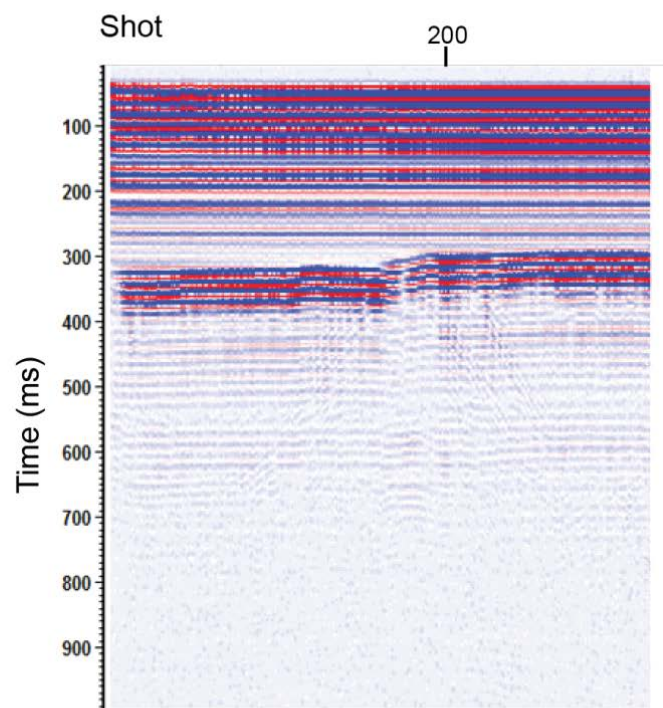


Figure 4-5. General processing flow applied to the zero-offset data.

The raw image of the zero-offset time section, with 321 traces, is shown in Figure 4-6. After performing filter panel tests, a wide bandpass filter of 5-10-80-90 Hz was initially applied followed by spiking deconvolution. Spiking deconvolution shortens the period of the embedded source wavelet, trying to create a spike (Geldart and Sheriff, 2004). Autocorrelation of the deconvolved data was examined for operator lengths of 20, 40, and 60 ms (Figure 4-7). The operator length of 60 ms was chosen, since reverberations in the data are suppressed, and the limestone bottom expected at ~420 ms becomes detectable. The deconvolved data with the tested operator lengths are shown in Figure 4-8. The operator was designed on a 200 to 1000 ms time gate. Predictive deconvolution was also investigated; however it seemed to best repress the reverberations in the much later multiples. At this time, the goal remains to focus on the primary reflection data.

a.



b.

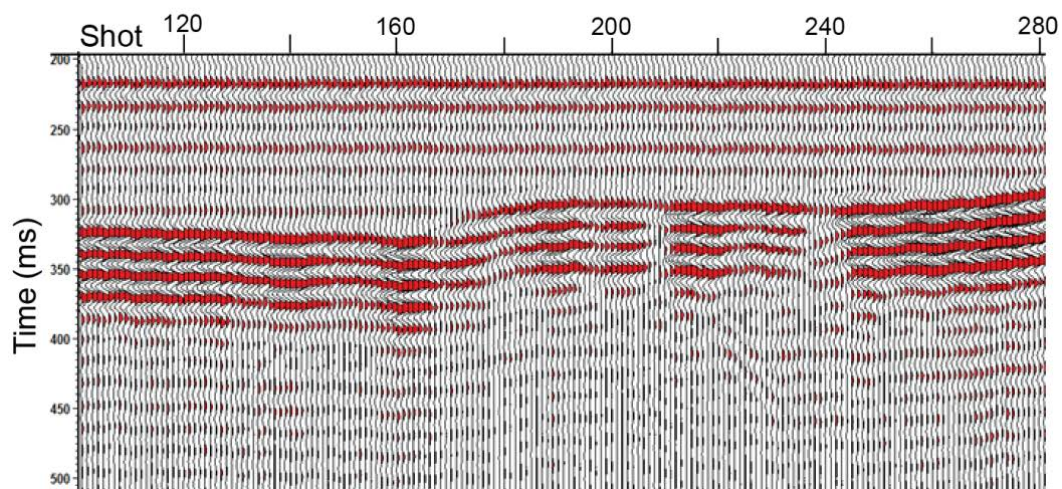


Figure 4-6. (a) Raw image of the zero-offset seismic data. (b) Wiggle trace with a zoom on fault zone.

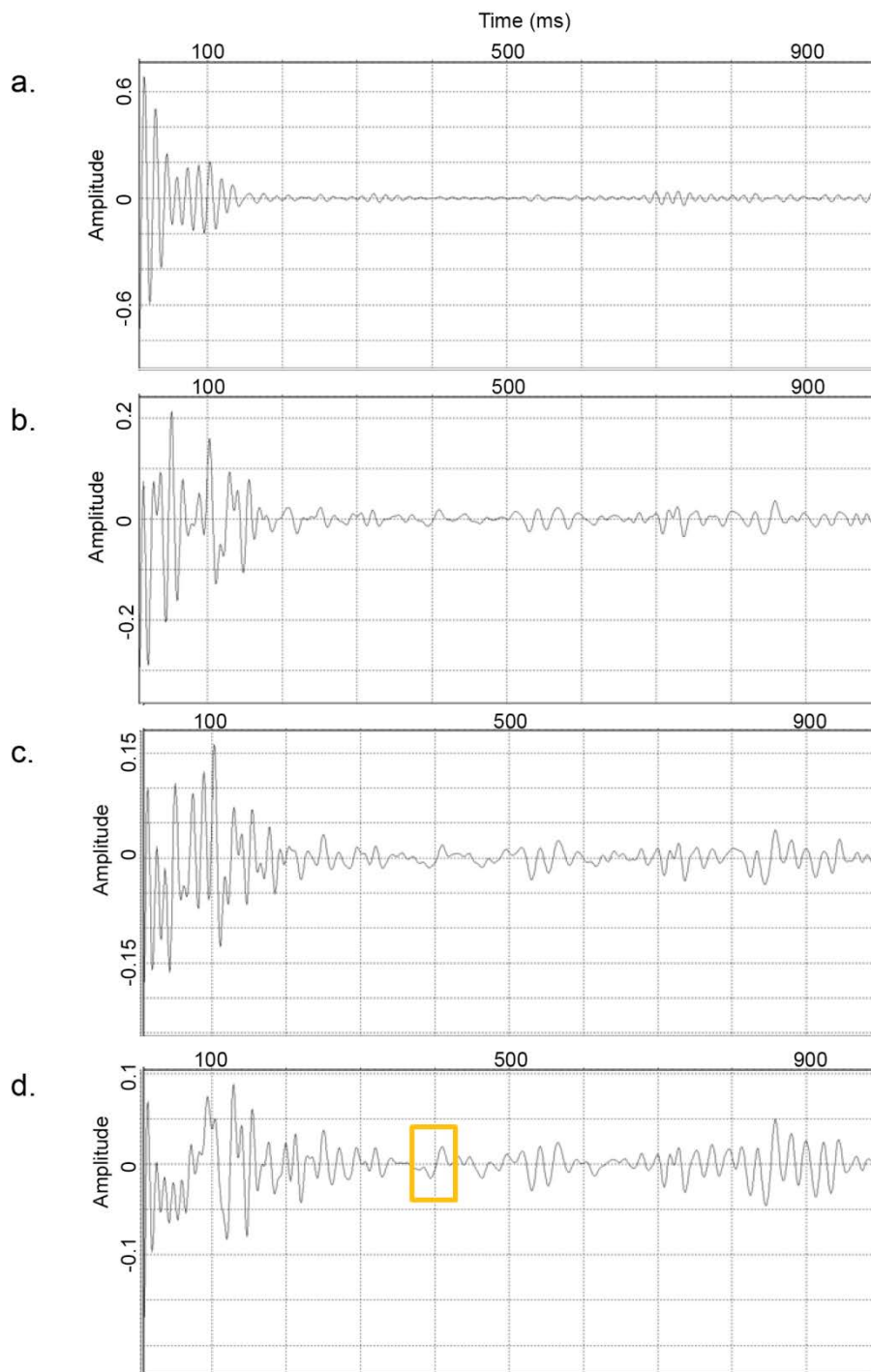


Figure 4-7. Autocorrelation of the deconvolved data is examined. (a) Raw data. Operator lengths of (b) 20 ms; (c) 40 ms; and (d) 60 ms. The yellow box highlights the signal at the bottom of the limestone model.

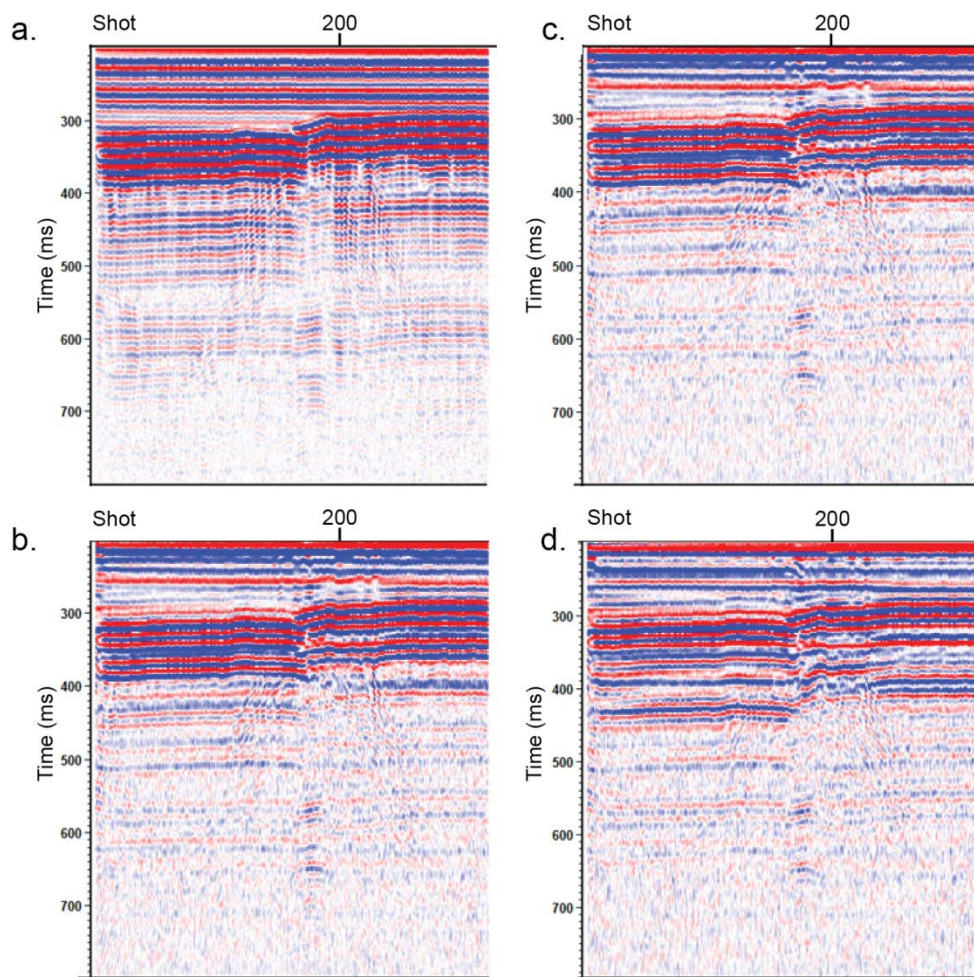


Figure 4-8. (a) Raw data. The deconvolved data with tested operator lengths of b) 20 ms, c) 40 ms, and d) 60 ms.

Prior to migration, random noise and increased noise from spiking deconvolution was attenuated in the frequency-wavenumber (FK) domain with a symmetrical fan filter (Figure 4-9). The migrated data were imaged with a 2D Kirchhoff time migration algorithm with a maximum lateral migration operator (or aperture) of 10 traces. In order to image true reflection amplitude, the migration aperture must be larger than the Fresnel zone (Sun and Bancroft, 2001). Comparisons of the final migrated image with tested

migration apertures are shown in Figure 4-10. A minimum aperture was selected for the final image to agree with the approximated calculation of a Fresnel zone of 48 m. A constant velocity of water (1480 m/s) was used in the migration algorithm. Scaling (AGC) and bandpass filtering were applied to the final migrated images for viewing.

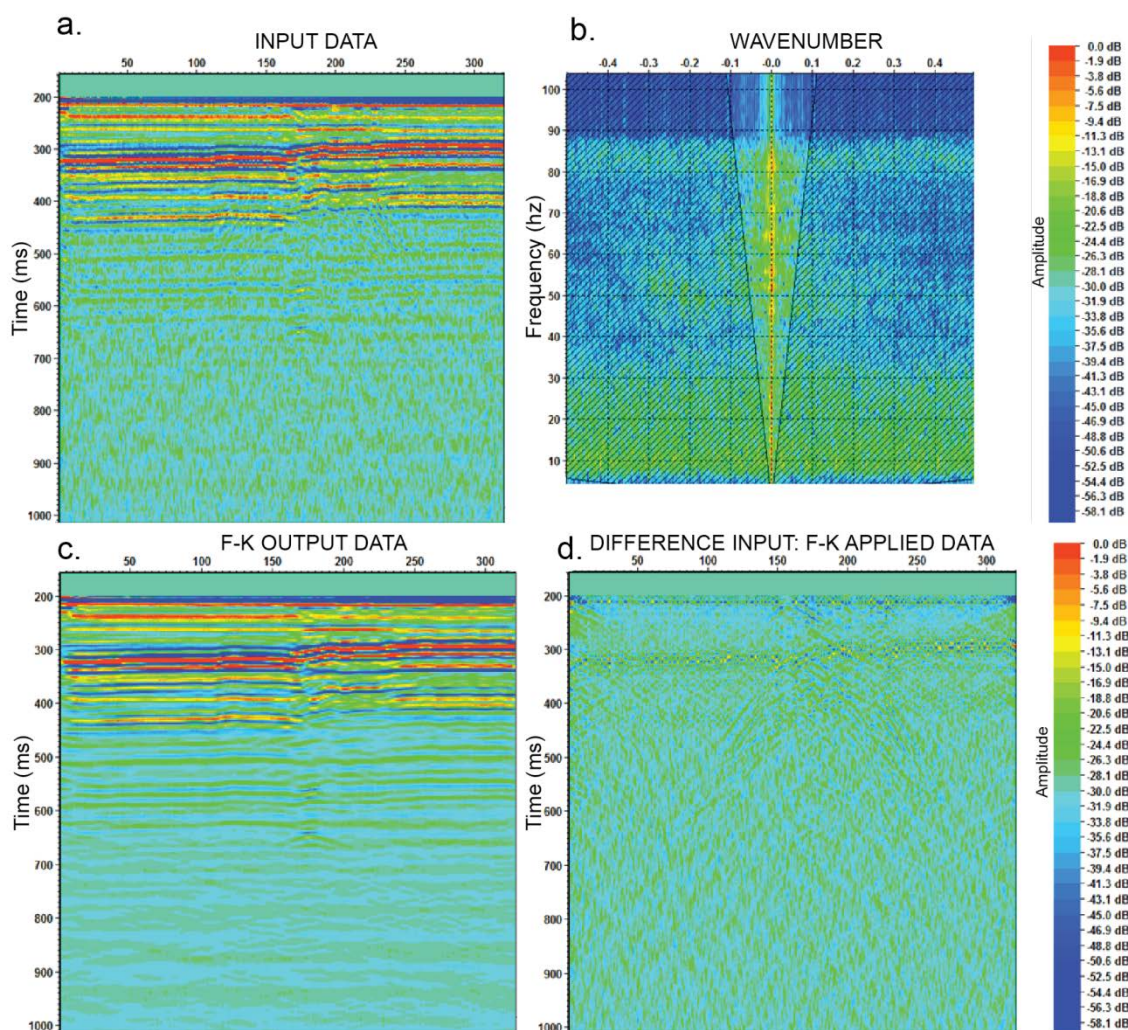


Figure 4-9. Noise attenuated in the FK domain with a symmetrical fan filter. (a) Input, (b) Applied filter, (c) Output, (d) With noise removed.

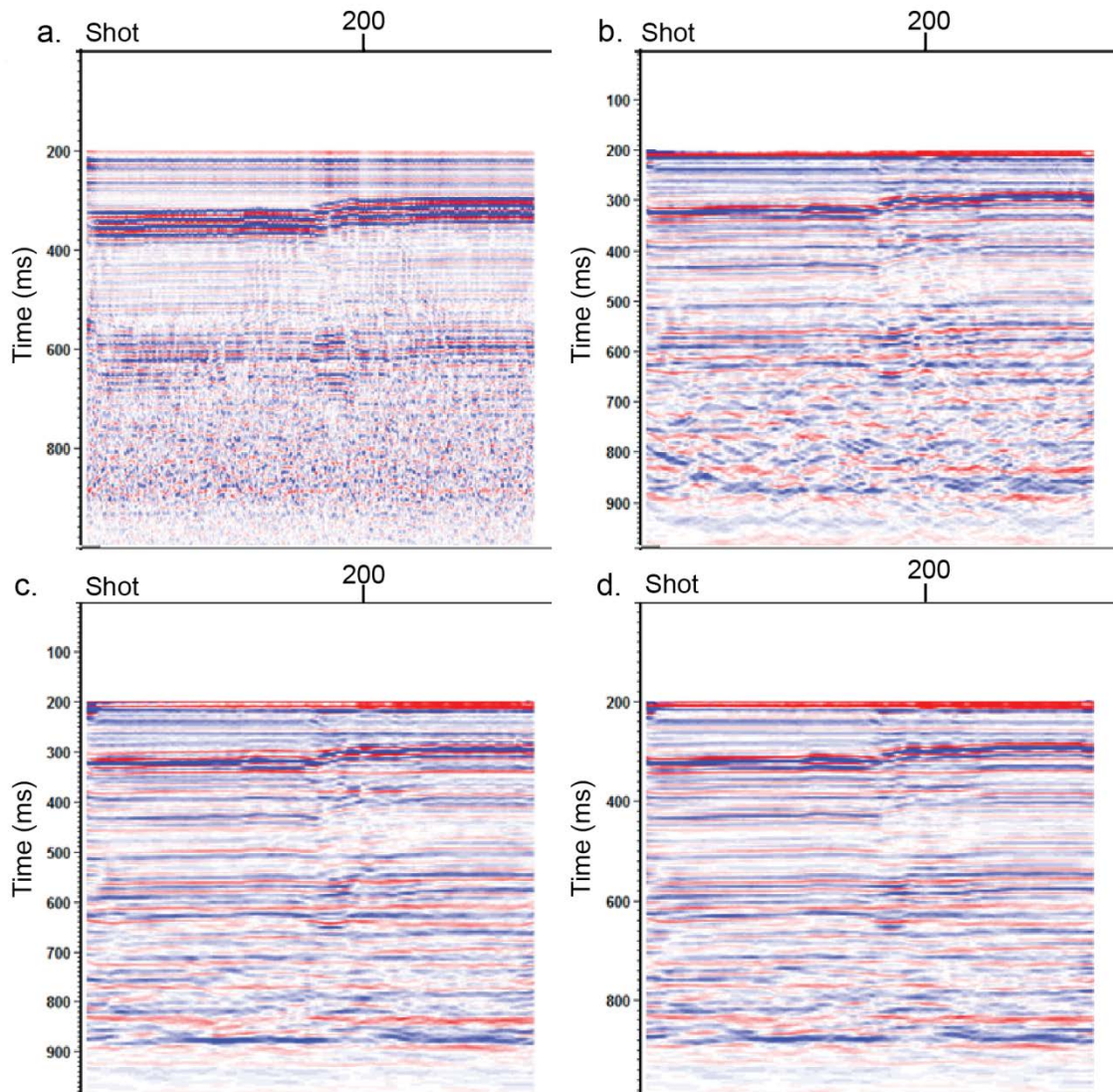


Figure 4-10. Comparisons of the final 2D Kirchhoff migrated image with tested migration apertures. (a) Raw data with scaling, (b) Migration aperture = 50 traces, (c) Migration aperture = 15 traces, (d) Selected migration aperture = 10 traces.

4.3.2 Common source data processing

The general processing flow for the common-shot data is given in Figure 4-11, which was applied to the Limestone-Water and Limestone-Acrylic fault models. The

processing sequence involves sorting and creating geometry, denoising in shot domain, velocity analysis and NMO, stack, and migration.

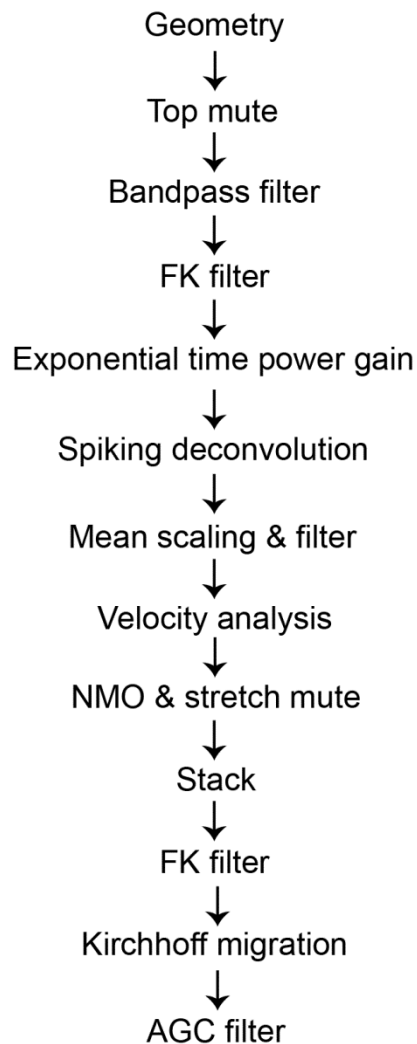


Figure 4-11. General processing flow applied to the common-source data.

The survey geometry was loaded from trace headers, and some edits were applied to ensure the data were in sequential order. Midpoint coordinates and offset vectors were created and saved to the geometry. A conservative surgical top mute was applied to mute the energy of the direct wave.

An average trace calculation was applied to the raw data to investigate the frequency content in an amplitude spectrum (Figure 4-12). Throughout the data, two energy bands are visible in the amplitude spectrum between 30 – 45 Hz and 50-75 Hz. For this dataset, the signal is estimated to be in the higher frequency band, with a dominant frequency of approximately 60 Hz. Further investigation is needed to determine if the two-banded amplitude spectrum is common in this type of seismic modeling data.

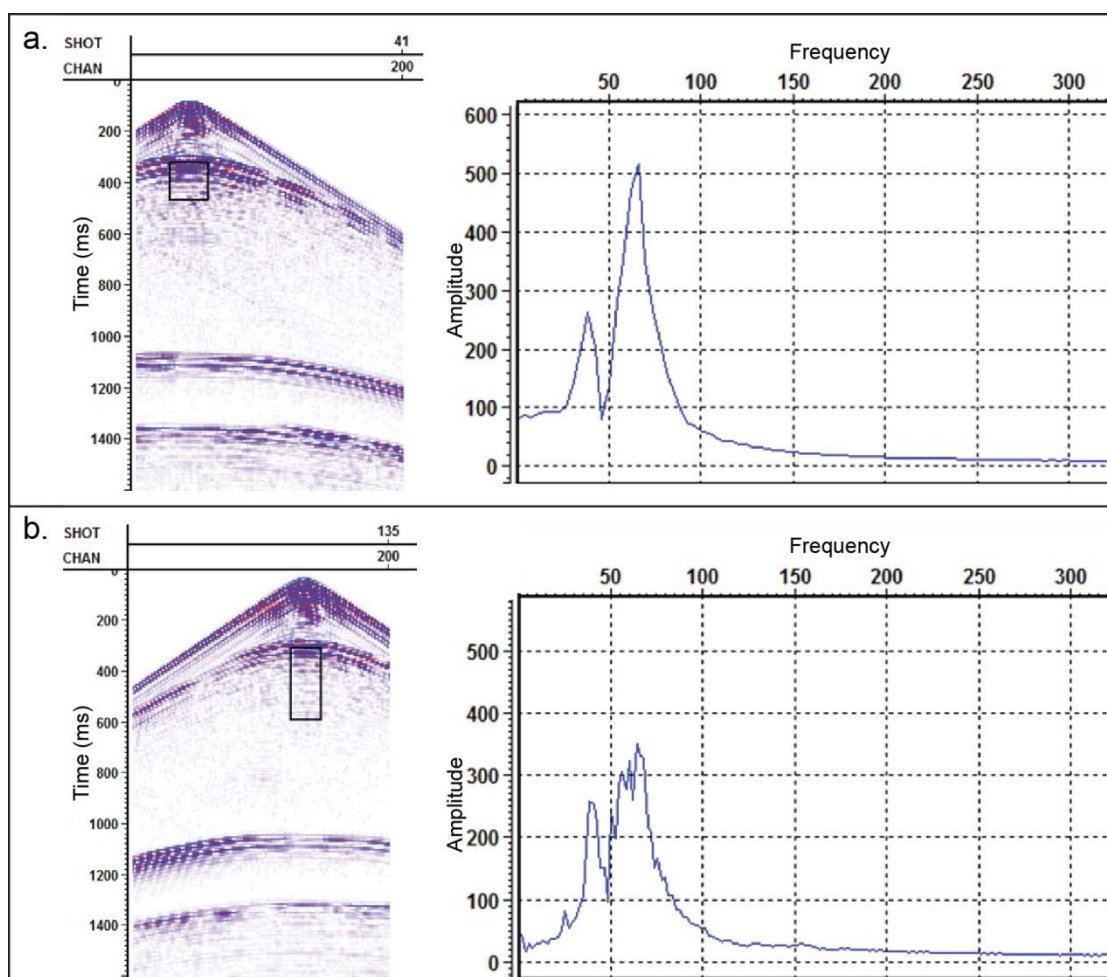


Figure 4-12. Spectral analysis of (a) Shot point 41 of the Limestone-Acrylic model, and (b) Shot point 135 of the Limestone-Water model. Two bands of energy are apparent throughout the data.

While in the shot domain, an FK filter was applied to remove random noise, and more energy from the direct wave (Figure 4-13). An exponential time power function of 1.4 was then applied to gain the data.

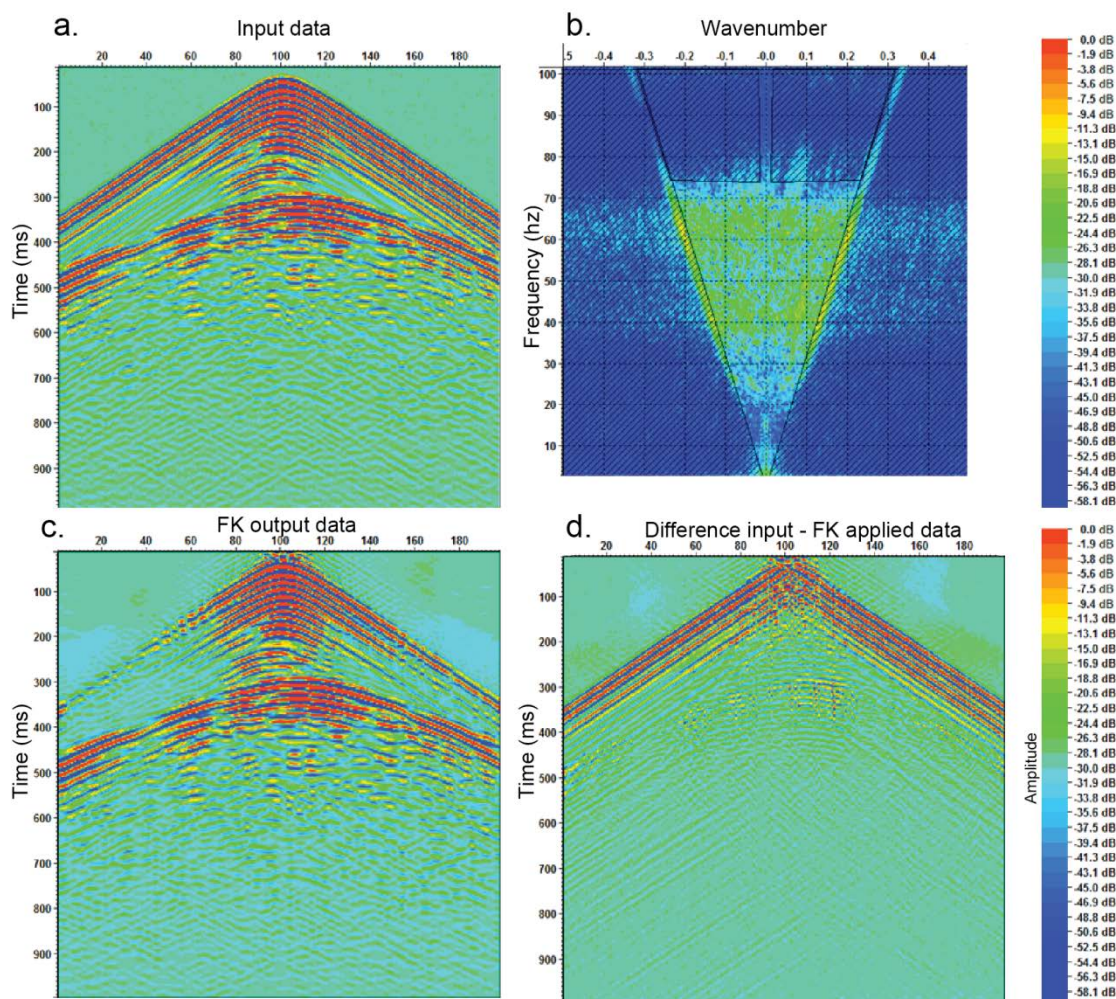


Figure 4-13. Noise attenuated in the FK domain with a symmetrical fan filter on the Limestone-Acrylic model in the shot domain. (a) Input data, (b) Applied filter, (c) Output data, and (d) Noise removed.

Spiking deconvolution was applied with a 20 ms operator, 10 ms taper, and 1% prewhitening. Operator lengths of 20, 40, 90, and 120 ms were tested (Figure 4-14). A comparison of the pre- and post- deconvolved shot point 101 for the Limestone-Acrylic

model is shown in Figure 4-15. Mean scaling was then applied to whiten the spectrum of the data, and a bandpass filter of 5-10-80-90 Hz was applied.

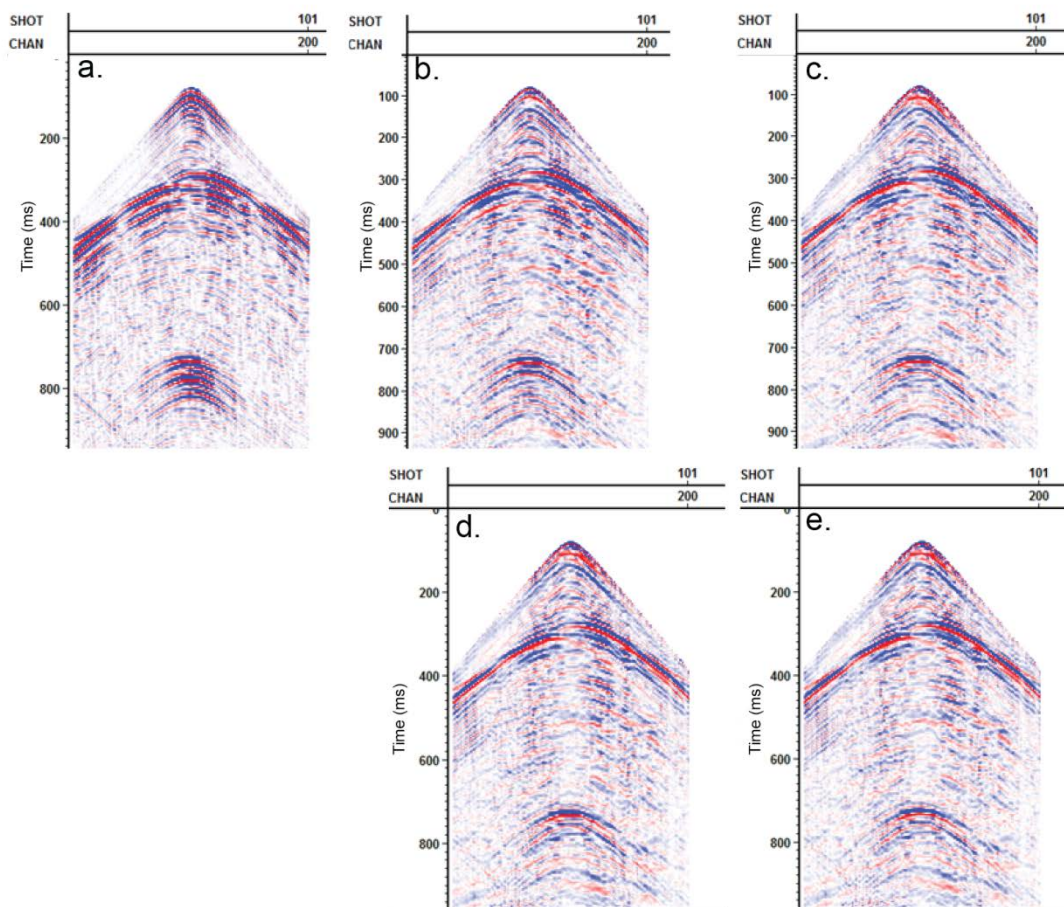


Figure 4-14. Spiking deconvolution testing on SP 101 of the Limestone-Water fault model. (a) Raw shot, (b) Operator length = 20 ms, (c) = 40 ms, (d) = 90 ms, and (e) = 120 ms. The 20 ms operator length was selected.

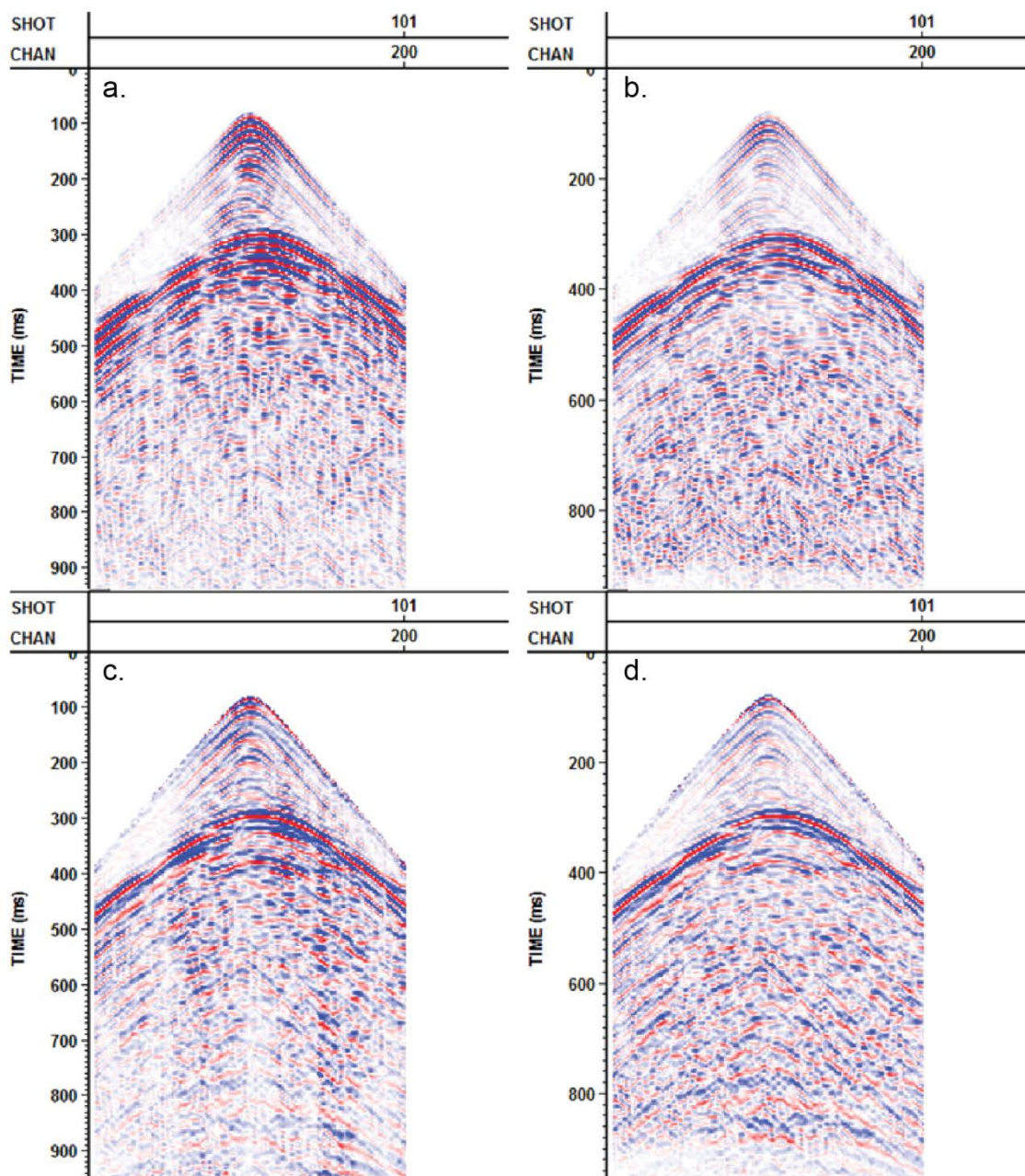


Figure 4-15. A comparison of the pre- and post-deconvolved shot point 101 for the Limestone-Acrylic model. FK-Filter and ExpTPower is applied. (a) No decon, AmpSc = 8, (b) With decon (operator = 20 ms), AmpSc = 8. (c) & (d) are the same, but have AGC applied prior.

Velocity analysis was performed on CMP sorted seismic data to correct for non-zero offsets. Normal moveout (NMO) is the time difference between travel time at zero-offset and a given offset (Yilmaz, 1987, p.155). A supergather of 5 CMP bins per zone was created, and used in semblance analysis. Borrowing traces from nearby midpoints increases signal to noise ratio, and keeping a small mix of CMP gathers ensures resolution is not compromised. Semblance and constant velocity stack analysis was performed on every tenth CMP. The velocity picks at CMP 201, which is where the center of the fault is located, is shown in Figure 4-16 for both the Limestone-Acrylic and Limestone-Water models. A mute was picked on every tenth CMP to cut moveout stretch at far offsets. The final velocity models are shown in Figure 4-17. The velocity models are similar; however, a decrease in velocity is seen in the water filled fault compared to the acrylic filled fault, as expected. The CMP gathers are NMO corrected and the picked stretch mute is applied. All data found within a CMP bin is then compressed to form a stacked section (Figure 4-18).

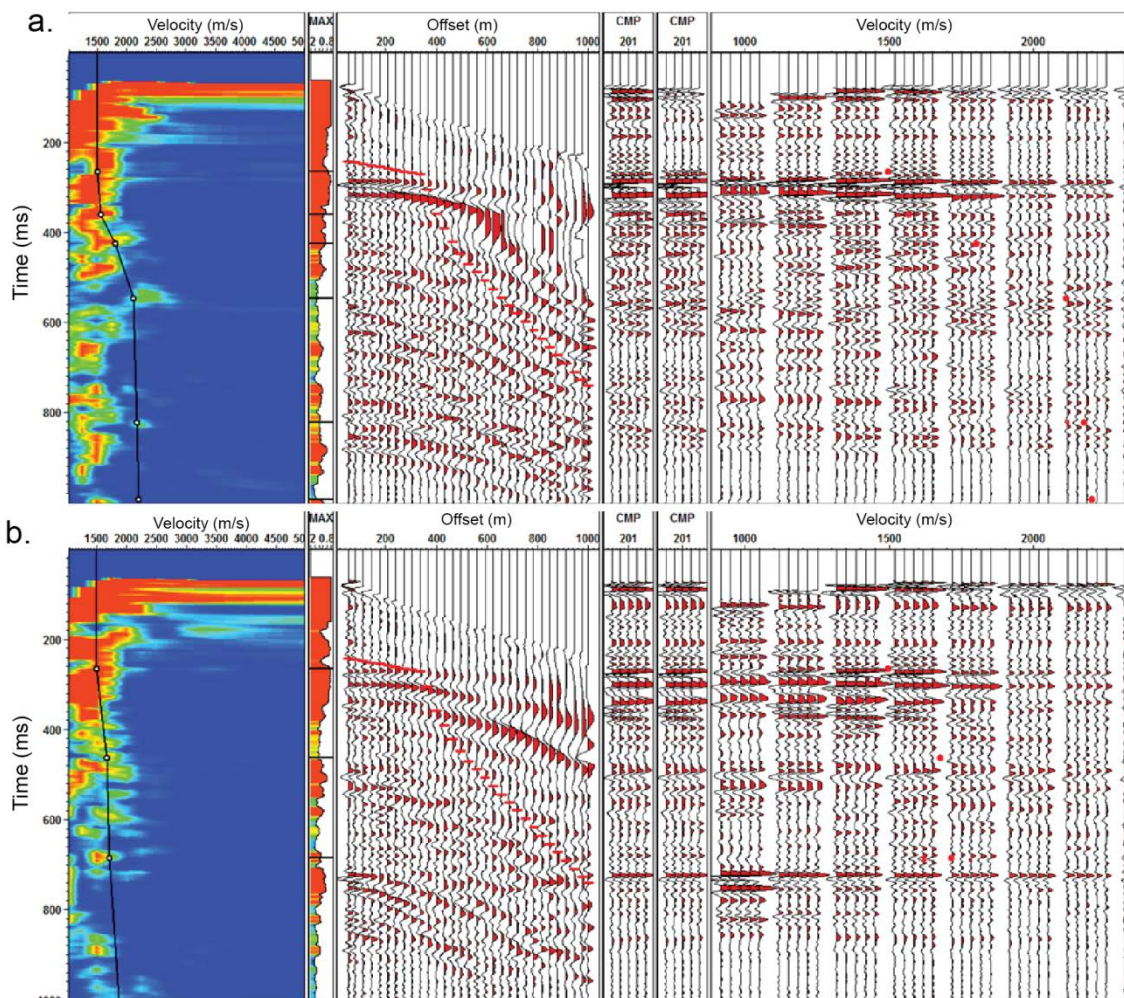


Figure 4-16. Semblance and constant velocity stack analysis for (a) the Limestone-Acrylic model, and (b) the Limestone-Water model. Images show the velocity picks at CMP 201, which is where the center of the fault is located. The velocities and a mute function were picked on every tenth CMP.

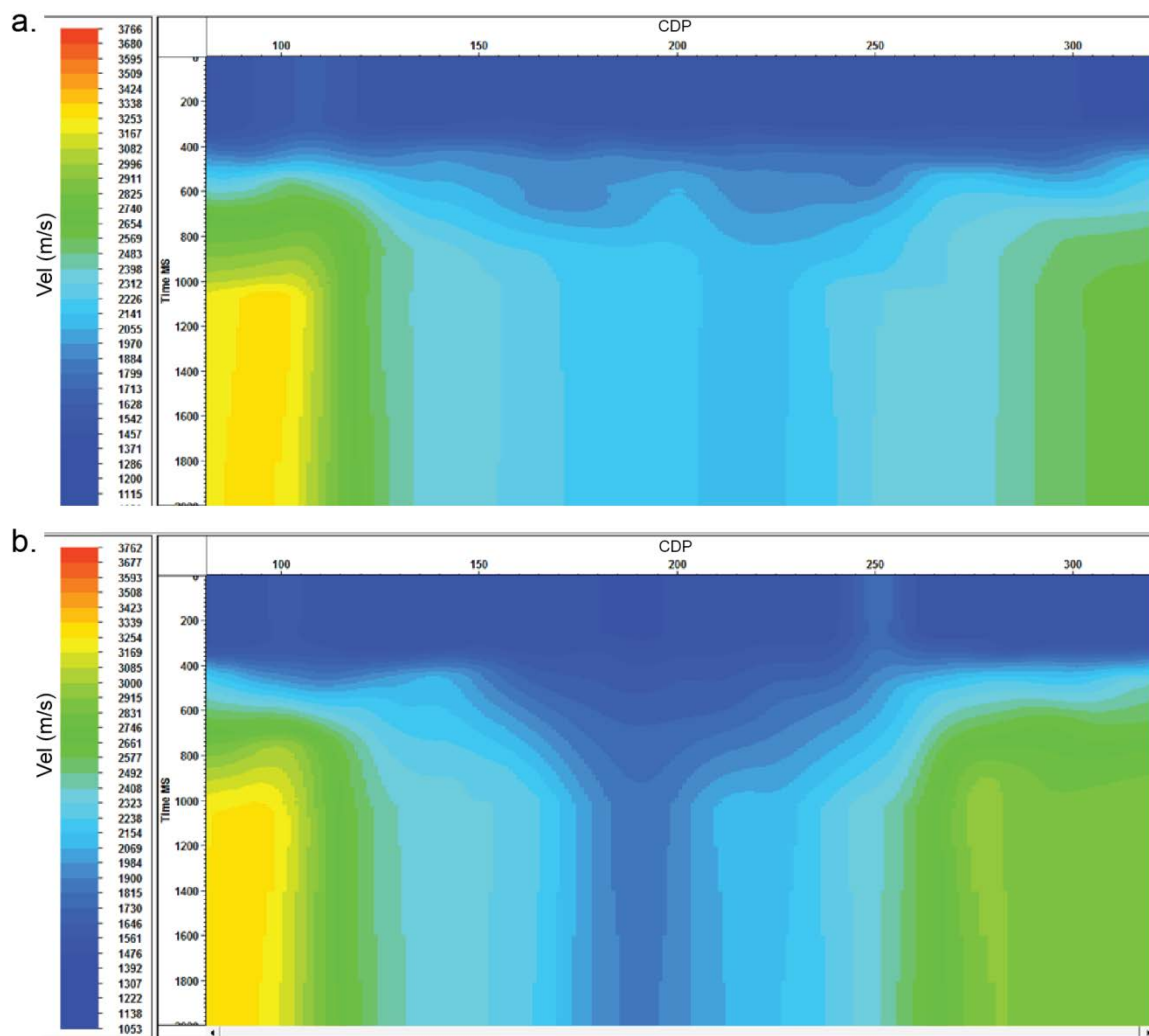


Figure 4-17. The final velocity models for (a) the Limestone-Acrylic model, and (b) the Limestone-Water model. A decrease in velocity is seen in the water filled fault zone compared to the acrylic filled fault zone.

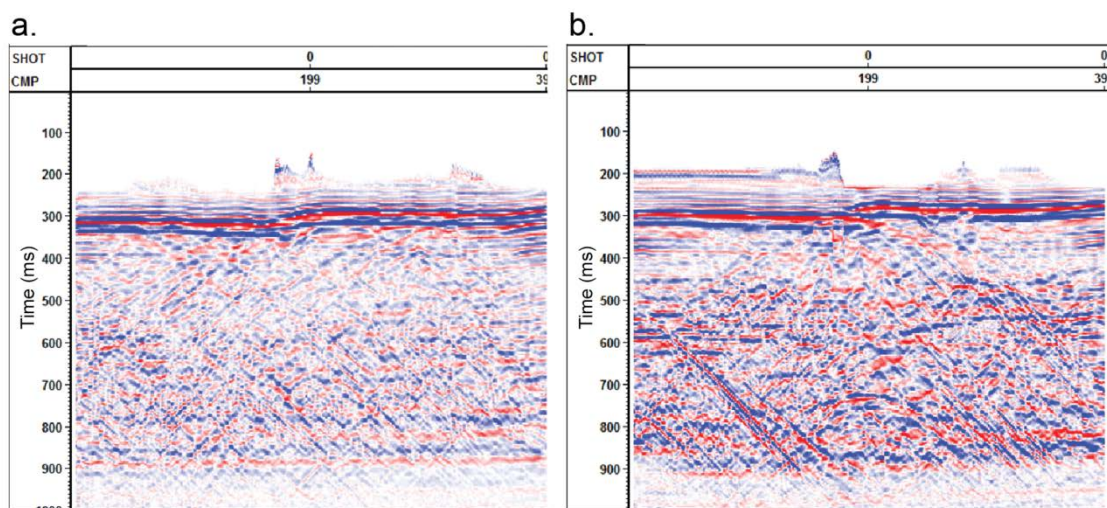


Figure 4-18. (a) Brute stack of the Limestone-Acrylic fault model seismic section, (b) Brute stack of the Limestone-Water fault model seismic section. With AGC.

An additional pass of FK fan filtering was applied to the stacked section of both models in order to remove what appears to be diagonal linear noise, which is much more apparent in the Limestone-Water fault model between 600-900 ms (Figure 4-18b). A possible interpretation of this more prominent linear feature in the Limestone-Water fault model is sideswipe, defined by Sheriff (2002) as “evidence of a structure feature which lies off to the side”. This noise was observed in the shot domain as well, however, it is easily removed from the stacked section in the FK domain (Figure 4-19).

A 2D post-stack Kirchhoff time migration algorithm was applied to the CMP stack data volumes. The goal of migration is to collapse diffractions, and move reflectors to their actual subsurface positions to make the stacked section more similar to the geologic cross section along the seismic line (Yilmaz, 1987, p.241). The migration operator parameters for the common source data sets is the same as the zero offset data

sets, as the CMP stack is equivalent to a zero offset section. A final flat top mute of 200 ms was applied, with an AGC window length of 300ms and bandpass filtering for viewing (Figure 4-20).

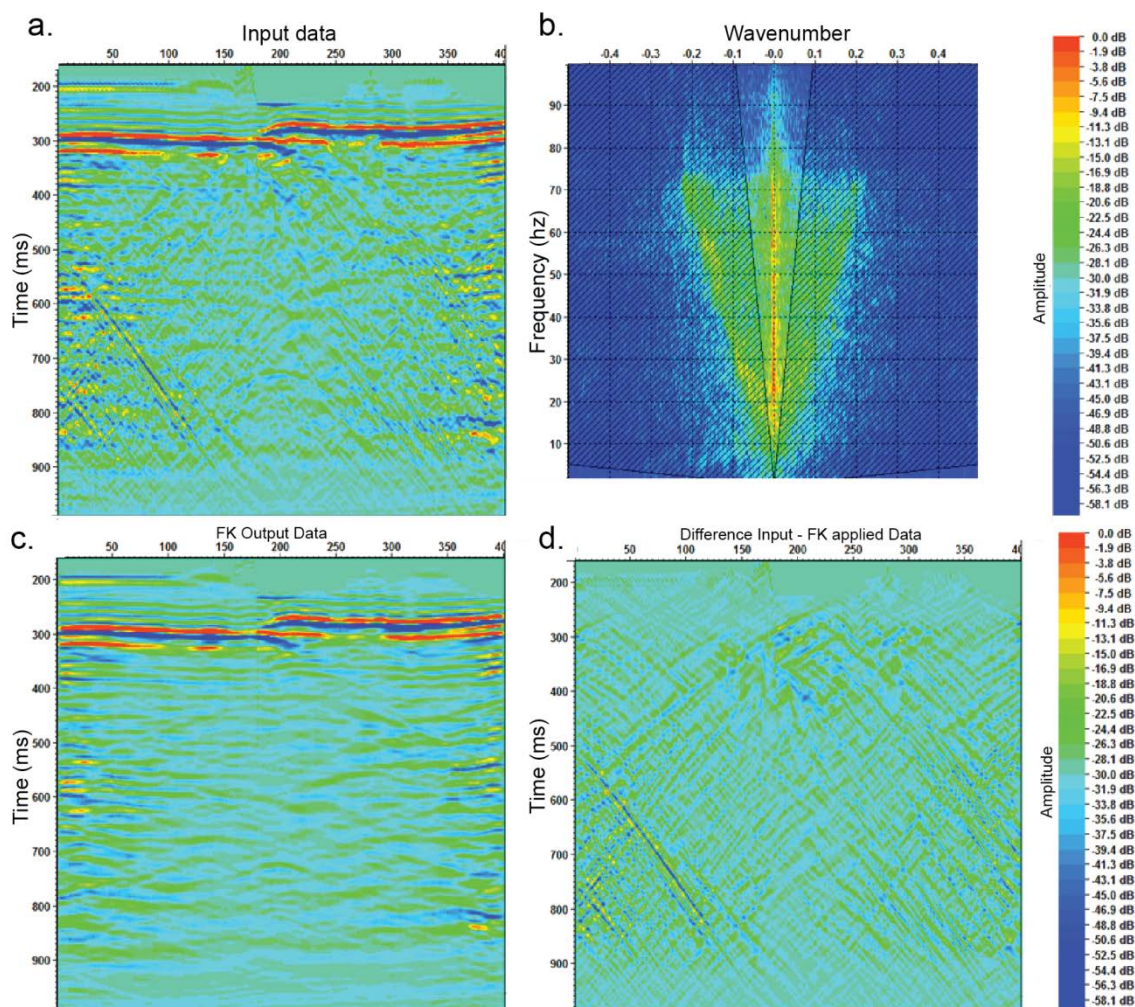


Figure 4-19. Noise attenuated in the FK domain with a symmetrical fan filter on the Limestone-Water model CMP stack. (a) Input data, (b) Applied filter, (c) Output data, and (d) Noise removed.

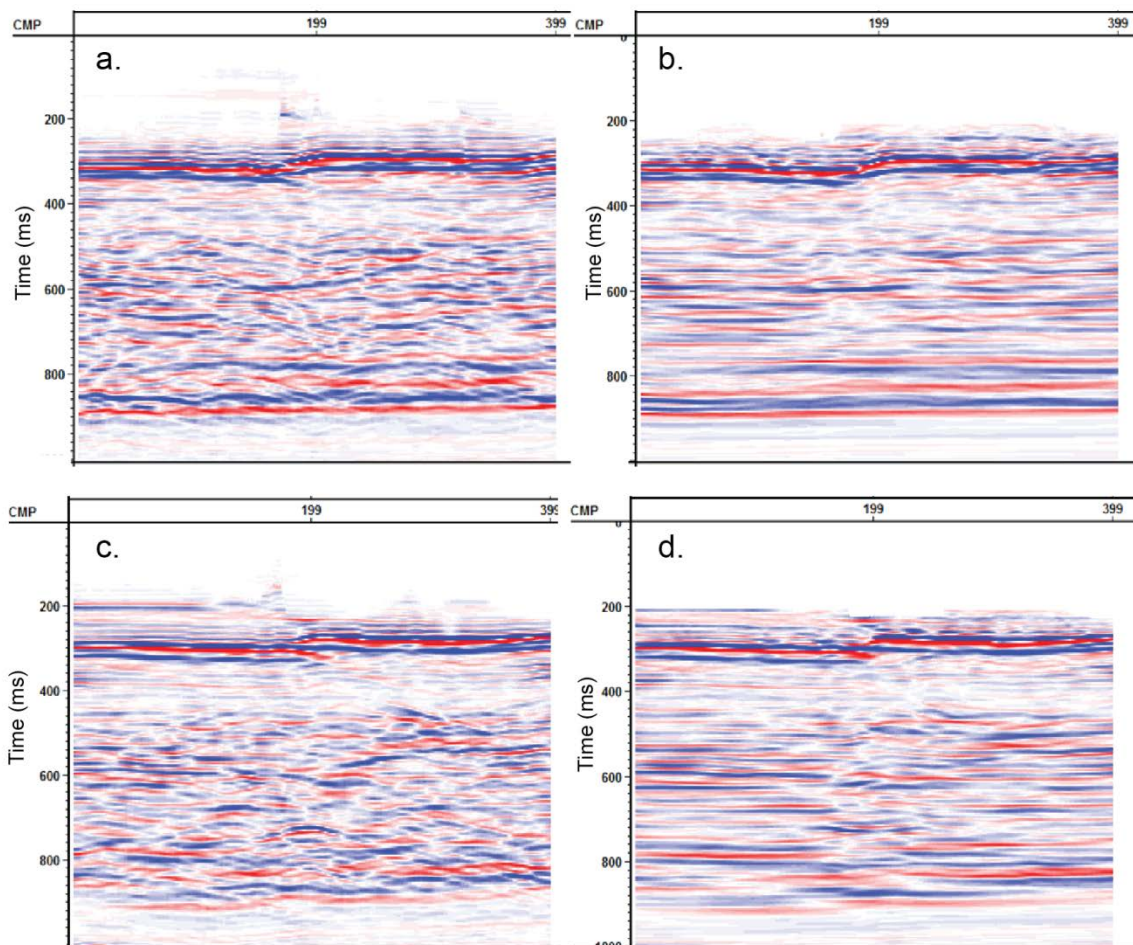


Figure 4-20. (a) CMP stack of the Limestone-Acrylic fault model, followed by (b) Post-stack migration. (c) CMP stack of the Limestone-Water fault model, followed by (d) Post-stack migration.

4.4 Event identification

Event identification by arrival times in the processed results was done by raytracing, which assumes the raypaths obey Snell's law and velocities are known (Sheriff, 1991, p. 242). Reflection events are labeled on raw shot 101 of the Limestone-Water common source model (Figure 4-21). An average trace calculation shows the events more clearly for the same shot record (Figure 4-22). The events were identified by calculating the two-way travel times, for primary and multiple reflections. Figure 4-23

illustrates the ray paths taken of each labeled event, and the summary of expected two-way time which the events are located is given in Table 4-2. The expected time is approximate, and small errors result from measurement of limestone thickness, water depth measurement and evaporation over time in the tank, and the assumption that the model is perfectly homogeneous. Down going events (Event E and F) are ghosts, while the other events listed are up going primaries.

The ghost reflections identified are of interest as they do not interfere with the primary upgoing reflections for this dataset, and may be useful in further imaging as an additional topic. When the water surface acts as a mirror reflecting the subsurface, ‘mirror imaging’ uses receiver ghosts (Grion et al., 2007). In fact, multiples can be imaged separately from primaries to provide a better illumination of the subsurface (Wang et al., 2012).

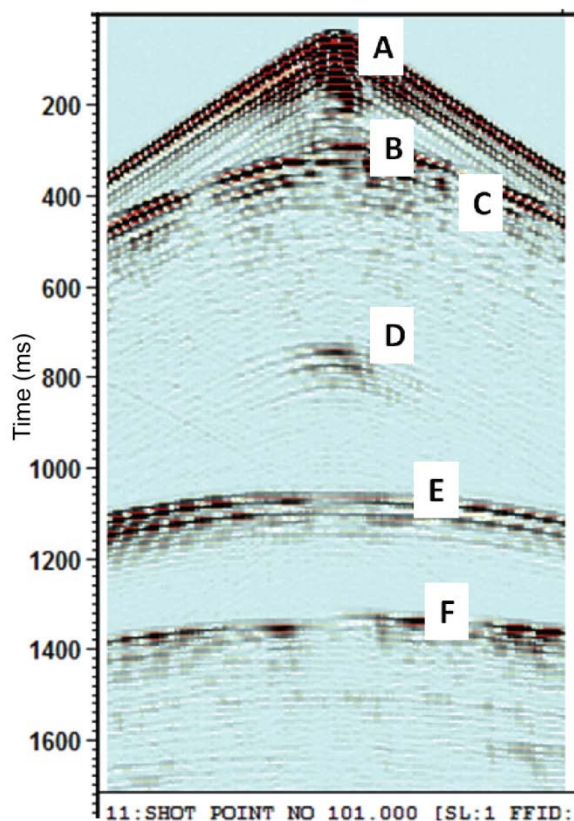


Figure 4-21. Event identification by ray tracing. A: Direct arrival (~32 ms), B: Water bottom/top of fault (~270 ms), C: Bottom of limestone (~380-400 ms), D: Bottom of water filled fault (~720 ms), E: Source ghost (~1020 ms), F: Receiver ghost/multiple of water bottom (~1275 ms).

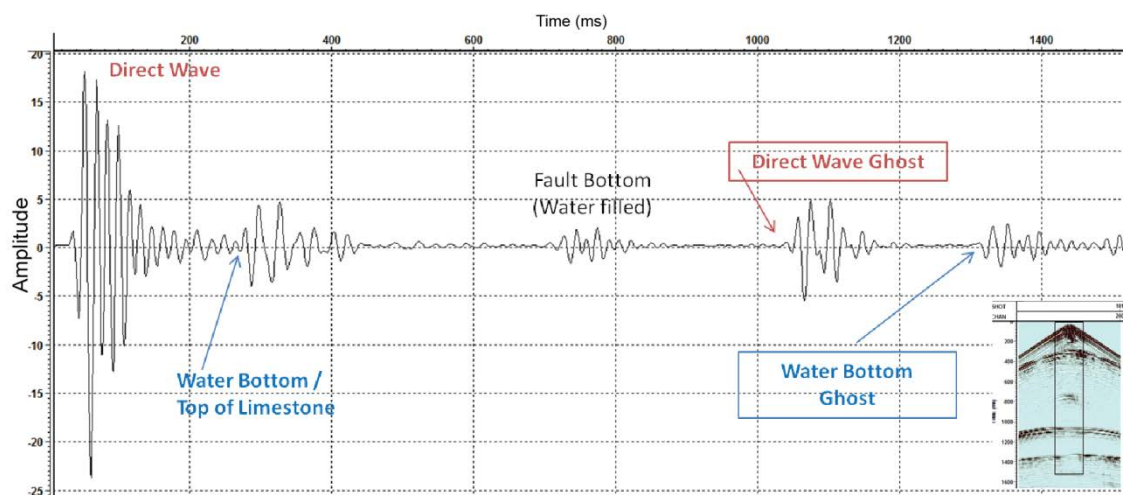


Figure 4-22. Average trace calculation showing identified reflection events in the shot record. The traces calculated in the average are shown in the inset figure.

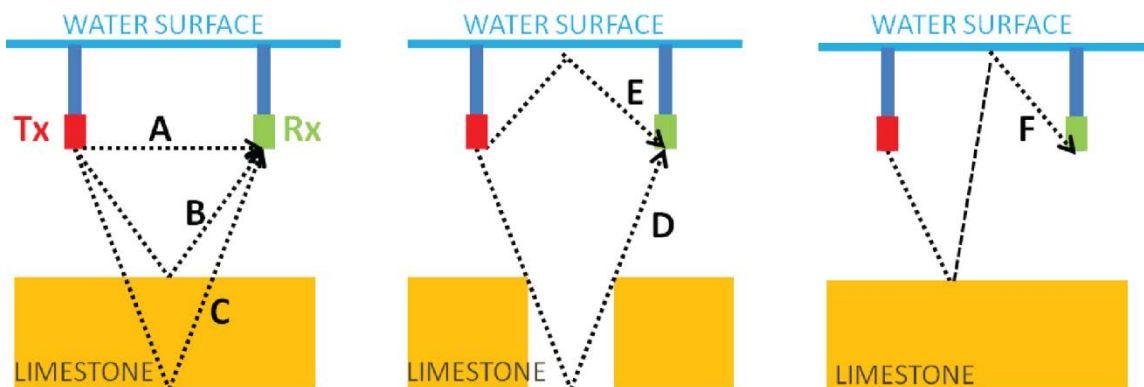


Figure 4-23. Illustration of events transmitted and received by the transducers. The ray paths taken through water and the model are used to calculate expected arrival time.

Table 4-2: Summary of expected two-way arrival times of the identified events.

LABEL	EVENT	EXPECTED 2-WAY TIME
A	Direct arrival	32 ms
B	Water bottom reflection	270 ms
C	Bottom of Limestone	390 ms
D	Water bottom of fault	670 – 720 ms
E	Source multiple (ghost)	~ 1080 ms
F	Receiver ghost	1290 ms

4.5 Discussion

The final processed images of the Limestone model for a water filled and acrylic filled faults are compared in Figure 4-24. The surface of the 50 m fault with 10 m uplift is easily identified in all the images; however, the imaging quality of the deformation zone varies between the common-source and zero-offset data. Errors in velocity analysis of common-shot data can result in lower signal-to-noise in the stack, and mispositioning

in migration. The constant velocity used for migrating the zero-offset data is limiting if complex structure is involved.

The bottom of the limestone is better resolved in the zero-offset sections. This is most likely due to difficulty in picking this event during velocity analysis. The water bottom of the fault is most apparent again, in the zero-offset section, at approximately 720 ms. The bottom of the acrylic fault is calculated to be close to 510 ms, and again, is imaged better in the zero-offset section. All the images show what may be an event near 600 ms which was not previously discussed, and was not obvious in the shot domain of the common-source data. Ray tracing indicates that this event may be a result of peg leg reverberations in the limestone.

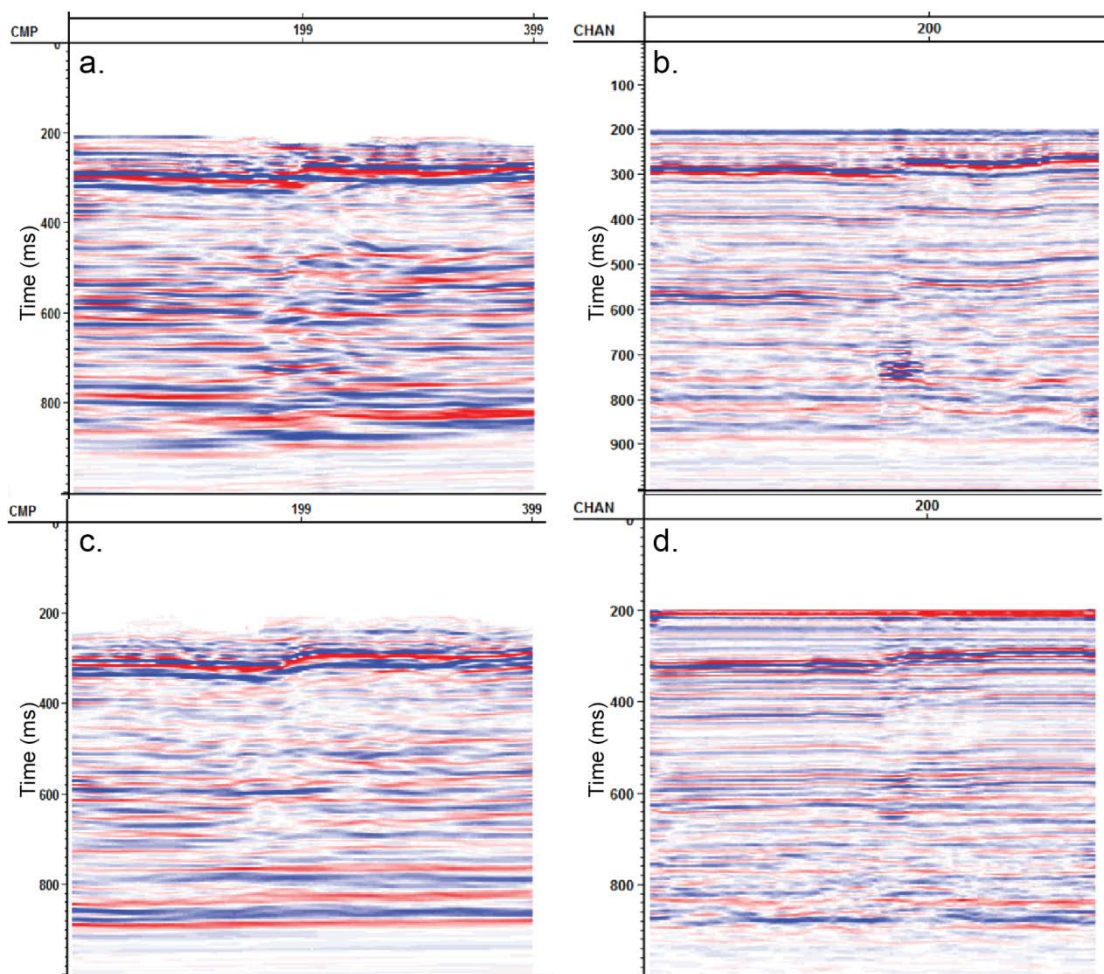


Figure 4-24. Final postmigrated images of the modeled fault zone. (a) Common-source Limestone-Water fault model. (b) Zero-offset Limestone-Water fault model. (c) Common-source Limestone-Acrylic fault model. (d) Zero-offset Limestone-Acrylic fault model.

A 2D post-stack time migrated seismic section of the New Zealand Greendale Fault is shown in Figure 4-25. This seismic land data was collected by CREWES in April, 2011 and processed by Sensor Geophysical. A similar fault throw and wide fault zone is observed in both the physical modeled and field seismic sections.

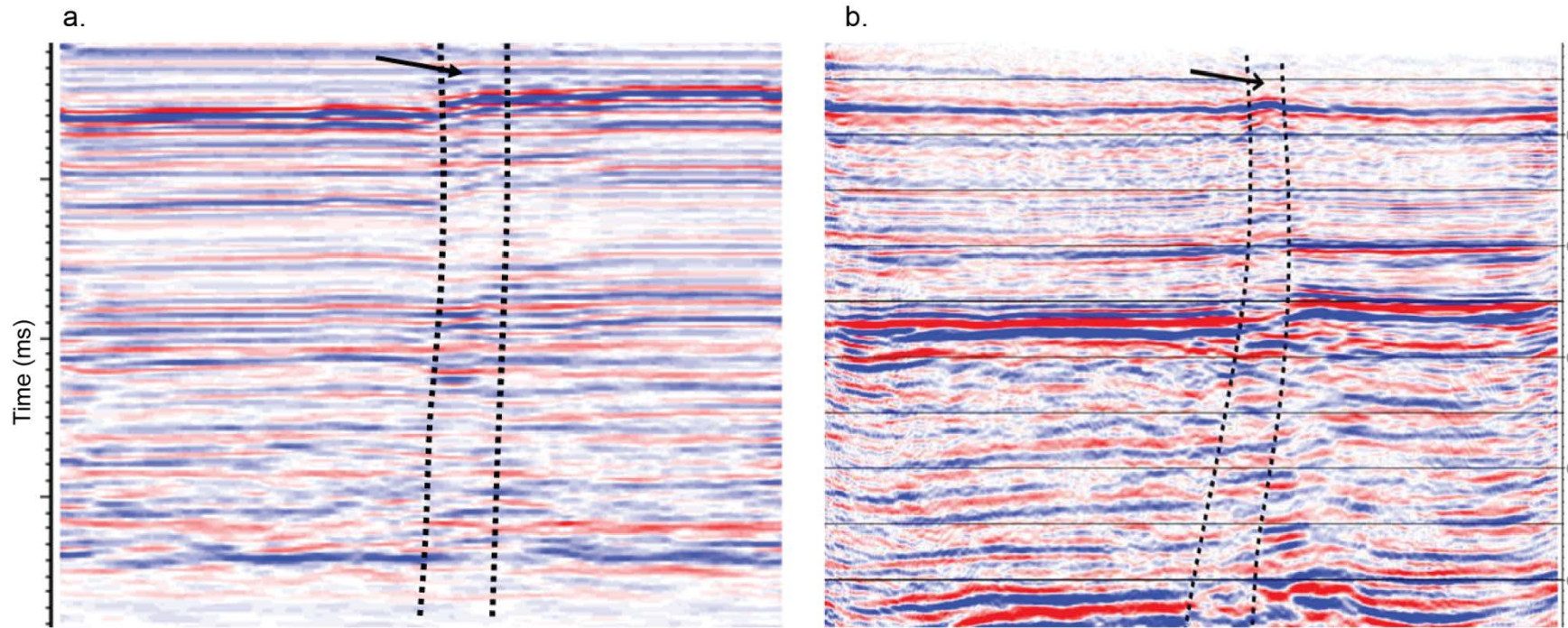


Figure 4-25. Post-stack migrated seismic sections imaging a fault rupturing the surface for (a) the physical model (b) the Greendale Fault zone, New Zealand. The deformed fault zone is outlined by a dashed black line.

Chapter Five: **CONCLUSIONS AND RECOMMENDATION FOR FUTURE WORK**

This research presented diverse approaches on how seismic data can be used to study active faults and seismic risk hazard assessment in Canterbury, New Zealand. Following two major earthquakes in the 2010-2011 Canterbury sequence, 2D seismic reflection data were acquired with the goal of mapping previously unknown faults. The objectives of this thesis were met using a range of methodologies, where the same acquired seismic data set was used to investigate both basement reactivated faults, and near surface characterization. The third component of this research examined seismic physical modeling of a fault zone, inspired by the Greendale Fault in Canterbury, New Zealand. This research may help constrain seismic hazard and risk assessment in the understanding of potential fault rupture locations during large earthquakes.

5.1 Seismic interpretation of the Canterbury Plains

5.1.1. Conclusions

The interpretation of P-wave reflection seismic data is presented in Chapter 2, which shows the presence of faults in the Canterbury Plains, previously suspected in the area, but never mapped. The faults have complex structures, and have the potential to reactivate under current tectonic stresses (Barnes et al., 2011). Seismic interpretation of the 2D seismic reflection data in the city of Christchurch identified the Port Hills Fault in the New Brighton Beach seismic profile, which projects approximately 350 m below surface. Displacement along the Miocene horizon shows approximately 28 m of slip. An additional blind fault was interpreted to occur further north of the Port Hills Fault and

may also be a reactivated reverse fault. The seismic profile along Barbadoes Street in the city center of Christchurch is relatively quiet in terms of active faults. However, a possible infilled channel was identified in the near surface, as well as an area possibly disturbed by liquefaction. The Highfield Road seismic section provided a comprehensive subsurface image of the complexity of the Greendale Fault, which was crossed by the seismic profile. Several fault splays were identified off the main fault, as well as a north dipping normal fault, that may not have been reactivated.

5.1.2 Recommendations for future work

The 2D seismic reflection profiles acquired in the Canterbury Plains of New Zealand was of good quality and used for geologic interpretation in this research. However to better characterize faults with complex structure, which is a three dimensional problem, a high resolution 3D seismic survey is recommended. Success has been shown in imaging active faults zones using 3D seismic in New Zealand (Kaiser et al., 2011).

The geologic interpretations of this research were based on comprehension of the geologic history of the Canterbury Plains, previous geophysical seismic interpretations both offshore and on land, and the 433 m deep Bexley wellbore. Deep wellbores within the city of Christchurch, and closer to the Greendale Fault would help constrain the seismic interpretations.

In addition, integrated geophysical, geologic, and engineering studies are recommended for future monitoring of the region.

5.2 MASW investigation of an active fault zone

5.2.1 Conclusions

Following the 2010-2011 Canterbury earthquake sequence, 2D seismic data acquired for the initial purpose of mapping previously unknown faults were also used to evaluate the MASW method in this region. Although the recommended acquisition parameters for a MASW survey were not adhered to since shallow surface investigation was not the primary intent, the MASW investigation results nonetheless provide valuable information about subsurface soil properties in terms of S-wave velocity. The MASW method was investigated near an active fault zone in two distinct sedimentary depositional environments, each presenting unique results. Low seismic shear-wave velocities were identified in each investigation, a possible indication of reduced soil rigidity which is an important consideration in detecting geologic hazards, such as liquefaction following an earthquake.

5.2.2. Recommendations for future work

To better evaluate soil conditions using MASW analysis, several recommendations are suggested for future data acquisition:

- A deeper investigation would have been permitted with use of low frequency geophones (Foti, 2005). As recorded low frequency waves penetrate into deeper layers, higher phase velocities of the fundamental mode would also be more apparent (Rix, 2005). A lower frequency sweep start of the seismic source is also recommended to capture low frequencies.

- Receiver spacing should be reduced if greater resolution of the near-surface layers are of interest, while bearing in mind that spatial ground roll aliasing can be prevented only if the geophone spacing is less than half of the shortest wavelength measured (Park et al., 1999).
- If lateral velocity and density variations in the near surface are suspected, spread length should be as short as possible since MASW assumes a layered earth model with no lateral variation in elastic properties (Park et al., 1999). Higher mode contamination at low frequencies may also be avoided by reducing spread length (Ivanov et al., 2011).
- Optimum acquisition parameters may be investigated by examining near-field and far-field effects in swept-frequency records obtained by uncorrelated Vibroseis records for quality control (Park et al., 1999).

As this dataset was not originally intended for MASW investigation, enhancements were made in data processing to augment the surface waves. Further analysis could be made on the pre-processing parameters made prior to dispersion curve analysis. This would be site and acquisition dependent. Analysis of dispersion curves could also be improved. A system of grading dispersion curves for integrity should be used prior to inversion. Grading dispersion curves based on signal-to-noise (S/N) may prove beneficial, as dispersion curves with $S/N < 0.5$ may result in unreliable results

(Park, 2003). Other methodologies worth mentioning but are beyond the scope of this thesis include: combining dispersion images processed from active and passive datasets to enlarge the frequency range of dispersion (Park et al., 2007), and incorporating higher modes to improve resolution of the inverted S-wave velocities (Xia et al., 2000b).

Results from the MASW study have provided robust S-wave velocity models, which are dependent on the shear modulus and density of a material. The next step would be to investigate the correlation between S-wave velocity and an estimation of liquefaction resistance potential. Intrusive tests such as downhole seismic surveys or cone penetrometer surveys could also be included to ground truth the results with S-wave velocity measurements.

5.3 Seismic physical modeling of an active fault zone

5.3.1. Conclusions

There is a compelling need for fault and subsequent deformation zone research. Physical modeling provides a method to test seismic acquisition parameters for detecting faults. A great deal of consideration must be taken when designing a physical model to best represent a realistic geologic model. Selection of materials is important especially when considering attenuation, scaled geologic properties, and the ability to withstand long durations in water. Processed model data yielded images that resolved a shallow fault with a small vertical throw and a deformed fault zone, similar to a field survey across a recent active fault in New Zealand. Resolution of seismic data is controlled not only by bandwidth, but additionally by acquisition and data processing parameters.

5.3.2 Recommendations for future work

Now knowing the limitations of physical modeling, future work includes constructing a new model with a more complex fault deformation zone, and a greater depth. Numerical modeling would also be an asset to this project. As well, an interesting side topic which came to light in this project includes mirror imaging of the ghost reflections to better image the zone of interest.

REFERENCES

- Anbazhagan, P., K.K.S. Thingbaijam, S.K. Nath, J.N. Narendara Kumar, and T.G. Sitharam, 2010, Multi-criteria seismic hazard evaluation for Bangalore city, India, *Journal of Asian Earth Sciences*, **38**, 186–198, doi:10.1016/j.jseaes.2010.01.001
- Andrus, R.D. and K.H. Stokoe, 1997, Liquefaction resistance based on shear wave velocity, In: National Center for Earthquake Engineering Research (NCEER) Workshop, Proceedings of the NCEER workshop on evaluation of liquefaction resistance of soils, Youd, T. L., and Idriss, I.M., ed., Salt Lake, Utah., U.S. Jan. 1996, 89-128.
- Andrus, R.D. and H. Stokoe, 1999, A liquefaction evaluation procedure based on shear wave velocity, Technical memorandum of PWRI 3653, Proceedings of Wind and Seismic Effects: U.S./Japan Natural Resources Development Program Tsukuba, Japan. May 11-14, 11-78.
- Andrus, R.D., P. Piratheepan, B.S. Ellis, J. Zhang, and C.H. Juang, 2004, Comparing liquefaction evaluation methods using penetration-VS relationships, *Soil Dynamics and Earthquake Engineering*, **24**, 713-721. doi:10.1016/j.soildyn.2004.06.001
- Angona, F.A., 1960, Two-dimensional modeling and its application to seismic problems: *Geophysics*, **25**, 468-482, doi: 10.1190/1.1438719.
- Bachrach, R., J. Dvorkin, and A.M. Nur, 1998, High-resolution shallow-seismic experiments in sand, Part II: Velocities in unconsolidated sand, *Geophysics*, **63**, 4, 1234-1240. doi: 10.1190/1.1444424
- Bachrach, R., J. Dvorkin, and A.M. Nur, 2000, Seismic velocities and Poisson's ratio of shallow unconsolidated sands, *Geophysics*, **65**, 2, 559-564. doi: 10.1190/1.1444751
- Bagheri, M., M.A. Riahi, Z.O. Khazar, M. Hosseini, and R. Mohseni, Ground roll attenuation in the radial trace domain, International earthquake symposium Kocaeli, 22-26 October, 2007.

- Bal, A.A., 1996, Valley fills and coastal cliffs buried beneath an alluvial plain: evidence from variation of permeabilities in gravel aquifers, Canterbury Plains, New Zealand, *Journal of Hydrology (NZ)*, **35**, 1, 1-27.
- Banab, K.K. and D. Motazedian, 2010, On the efficiency of the multi-channel analysis of surface wave method for shallow and semideep loose soil layers, *International Journal of Geophysics*, 2010, Article ID 403016, 13 pages. doi:10.1155/2010/403016
- Banister, S. and K. Gledhill, 2012, Evolution of the 2010-2012 Canterbury earthquake sequence, *New Zealand Journal of Geology and Geophysics*, **55**, 3, 296-304. doi: 10.1080/00288306.2012.680475
- Barley, M.E., 1987, Origin and evolution of mid-Cretaceous, garnet-bearing, intermediate and silicic volcanics from Canterbury, New Zealand, *Journal of Volcanology and Geothermal Research*, **32**, 1-3, 247-267.
- Barnes, C., 1993, Instantaneous spectral bandwidth and dominant frequency with applications to seismic reflection data: *Geophysics*, **58**, 419-428, doi: 10.1190/1.1443425.
- Barnes, P., C. Castellazzi, A. Gorman, and S. Wilcox, 2011, Submarine faulting beneath Pegasus Bay, Offshore Christchurch. Short-term Canterbury Earthquake Recovery Project 2: Offshore Faults. Prepared for the New Zealand Natural Hazards Research Platform. Contract reference 2011-NIW-01-NHRP. NIWA Client Report No. WLG2011-28. 46 pp.
- Bay, J. A. and B.R. Cox, 2001, Shear wave velocity profiling and liquefaction assessment of sites shaken by the 1999 Kocaeli, Turkey earthquake, PEER Project Report SA3017-18336, Pacific Earthquake Engineering Research, Berkeley, CA.
- Beaven, J., E. Fielding, M. Motagh, S. Samsonov, N. Donnelly, 2011, Fault location and slip distribution of the 22 February 2011 Mw 6.2 Christchurch, New Zealand, Earthquake from geodetic data, *Seismological Research Letters*, **82**, 6, 789-799

- Beaven, J., M. Motagh, E.J. Fielding, N. Donnelly, D. Collett, 2012, Fault slip models of the 2010-2011 Canterbury, New Zealand, earthquakes from geodetic data and observations of postseismic ground deformation, *New Zealand Journal of Geology and Geophysics*, **55**, 3, 207-221.
- Beaven, J., S. Samsonov, M. Motagh, L. Wallace, S. Ellis, and N. Palmer, 2010, The Darfield (Canterbury) earthquake: Geodetic observations and preliminary source model, *Bulletin of the New Zealand society for earthquake engineering*, **43**, 4, 228-235.
- Beetham R.D. and W.A. Waters, 1985, Geology of Torlesse and Waipapa terrane basement rocks encountered during the Tongariro Power Development project, North Island, New Zealand, *New Zealand Journal of Geology and Geophysics*, **28**, 575-594.
- Bertram, M., 2013, Personal communication, University of Calgary, Canada.
- Bishop, D.G., J.D. Bradshaw, C.A. Landis, 1985, Provisional terrane map of the South Island, New Zealand, in Howell, D.G., ed., *Tectonostratigraphic terranes of the Circum-Pacific region: Circum-Pacific Council for Energy and Mineral Resources, Earth Science Series*, **1**, 515-521.
- Brackley, H.L., 2005, Review of liquefaction hazard information in eastern Canterbury, including Christchurch City and parts of Selwyn, Waimakariri and Hurunui Districts: Appendix 5. Prepared for Environment Canterbury. GNS Science Consultancy Report 2012/218.
- Bradshaw, J.D., S.D. Weaver, R.J. Muir, 1996, Mid-Cretaceous oroclinal bending of New Zealand terranes, *New Zealand Journal of Geology and Geophysics*, **39**, 461-468.
- Brown, L.J., D.D. Wilson, N.T. Moar, and D.C. Mildenhall, 1988, Stratigraphy of the late Quaternary deposits of the northern Canterbury Plains, New Zealand, *New Zealand Journal of Geology and Geophysics*, **31**, 3, 305-335. doi: 10.1080/00288306.1988.10417779.

- Browne, G.H., B.D. Field, D.J.A. Barrell, R. Jongens, K.N. Bassett, R.A. Wood, 2012, The geological setting of the Darfield and Christchurch earthquakes, *New Zealand Journal of Geology and Geophysics*, **55**, 3, 193-197.
- Campbell, H., A. Malahoff, G. Browne, I. Graham, R. Sutherland, 2012a, *New Zealand Geology*, Episodes Journal of International Geoscience, **35**, 1, 57-71.
- Campbell, J.K., J.R. Pettinga, and R. Jongens, 2012b, The tectonic and structural setting of the 4 September 2010 Darfield (Canterbury) earthquake sequence, New Zealand, *New Zealand Journal of Geology and Geophysics*, **55**, 3, 155-168.
- Carpentier, S.F.A., A.G. Green, J. Doetsch, C. Dorn, A.E. Kaiser, F. Campbell, H. Horstmeyer, and M. Finnemore, 2012, Recent deformation of Quaternary sediments as inferred from GPR images and shallow P-wave velocity tomograms: Northwest Canterbury Plains, New Zealand, *Journal of Applied Geophysics*, **81**, 2-15. doi: 10.1016/j.jappgeo.2011.09.007.
- Cheadle, S.P., M.B. Bertram, and D.C. Lawton, 1985, Development of a physical seismic modelling system, University of Calgary: Current research part A, Geological Survey of Canada, Paper no. 85-1A, 499-504.
- Cooper, A.F., B.A. Barreiro, D.L. Kimborough, and J.M. Mattinson, Lamprophyre dike intrusion and the age of the Alpine fault, New Zealand, 1987, *Geology*, **15**, 941-944.
- Cox, S.C, R. Sutherland, 2007, Regional geological framework of South Island, New Zealand, and its significance for understanding the active plate boundary, in Okaya, D., T. Stern, F. Davey, eds, *A continental plate boundary: Tectonics at South Island, New Zealand: Geophysical Monograph Series 175*, American Geophysical Union, 19-46.
- Davey, F. J., et al., 1998, Preliminary results from a geophysical study across a modern, continent-continent collisional plate boundary—The Southern Alps, New Zealand, *Tectonophysics*, **288**, 221– 235. doi: 10.1016/S0040-1951(97)00297-7

- DeMets, C., R.G. Gordon, D.F. Argus, and S. Stein, 1990, Current plate motions, *Geophysical Journal International*, **101**, 425-478.
- Dikmen, U., M.O. Arisoy, and I. Akkaya, 2010, Offset and linear spread geometry in the MASW method, *Journal of Geophysics and Engineering*, **7**, 2, 211-222.
doi:10.1088/1742-2132/7/2/S07
- Dobrin, M.B., 1976, *Introduction to geophysical prospecting*, 3rd edition. McGraw-Hill.
- Dorn, C., S. Carpentier, A.E. Kaiser, A.G. Green, A. Horstmeyer, F. Campbell, J. Campbell, R. Jongens, M. Finnemore, and D.C. Nobes, 2010, First seismic imaging results of tectonically complex structures at shallow depths beneath the northwest Canterbury Plains, New Zealand, *Journal of Applied Geophysics*, **70**, 317-331. doi:
10.1016/j.jappgeo.2009.06.003
- Duffy, B.G., 2008, *Development of multichannel analysis of surface waves (MASW) for characterizing the internal structure of active fault zones as a predictive method of identifying the distribution of ground deformation*, M.Sc. Thesis, University of Canterbury.
- Eberhart-Phillips, D. And S.Bannister, 2010, 3-D imaging of Marlborough, New Zealand, subducted plate and strike-slip fault systems, *Geophysical Journal International*, **182**, 73–96.
- Environment Canterbury, 2013a, *Environment Canterbury Regional Council: Your Region*. Retrieved from: <http://ecan.govt.nz/about-us/your-region/Pages/Default.aspx>
- Environment Canterbury, 2013b, *Environment Canterbury Regional Council: Maps of the Canterbury Region*. Retrieved from: <http://ecan.govt.nz/services/online-services/Pages/maps-canterbury-region.aspx>
- Field, B.D., G.H. Browne, and others, 1989, *Cretaceous and Cenozoic sedimentary basins and geological evolution of the Canterbury Region, South Island, New Zealand*. New Zealand Geological Survey Basin Studies 2.

- Finnemore, M., 2004, The Application of Seismic Reflection Surveying to the Characterisation of Aquifer Geometry and Related Active Tectonic Deformation, North Canterbury, Unpublished doctoral dissertation, University of Canterbury, Christchurch, New Zealand.
- Forsyth, P.J., D.J.A. Barrell, and R. Jongens (compilers), 2008, Geology of the Christchurch area: Institute of Geological and Nuclear Sciences 1:250,000 geological map and report 16: GNS Science, Lower Hutt, New Zealand.
- Fossen, H., 2010, Structural Geology: Cambridge University Press.
- Foti, S., 2005, Surface waves in dissipative media: Forward and inverse modelling, In: Lai, C.G, Wilmanski, K (eds) Surface waves in geomechanics: direct and inverse modelling for soils and rocks, CISM Series, Number 481. Springer-Verlag, Wien-Newyork (2005), p. 47–71.
- French, W.S., 1974, Two-Dimensional and three-dimensional migration of model-experiment reflection profiles: *Geophysics*, **39**, 265-277, doi: 10.1190/1.1440426.
- Gallant, E.V., D.C. Lawton, and M.B. Bertram, 1991, Development of a physical modelling system for 3-C x 3-D experiments. CREWES Research Report, **33**, 524-528.
- Geldart, L.P., and R.E. Sheriff, 2004, Problems in Exploration Seismology and their solutions: Society of Exploration Geophysicists, p. 332.
- GeoNet, 2013, <http://www.geonet.org.nz/quakes/region/canterbury/statistics> (accessed 30 May 2013).
- Ghisetti, F.C., and R.H. Sibson, 2012, Compressional reactivation of E-W inherited normal faults in the area of the 2010-2011 Canterbury earthquake sequence, New Zealand *Journal of Geology and Geophysics*, **55**, 3, 177-184.
- Glaser, S.D. and R.M. Chung, 1995, Estimation of liquefaction potential by in situ methods, *Earthquake Spectra*: August 1995, **11**, No. 3, 431-455. doi: 10.1193/1.1585822

- Gledhill, K., J. Ristau, M. Reyners, B. Fry, and C. Holden, 2011, The Darfield (Canterbury, New Zealand) Mw 7.1 Earthquake of September 2010: A Preliminary Seismological Report, *Seismological Research Letters*, **82**, 3, 378-386.
- Google Earth, 2013, Google Earth Version 7.0.3.8542, software downloaded and installed from <http://www.google.com/earth/index.html>, images accessed 30 May 2013 and 29 June 2013.
- Grion, S., E. Russell, M. Manin, X. Miao, A. Pica, Y. Wang, P. Granger, and S. Ronen, 2007, Mirror imaging of OBS data, *First Break*, **25**, 37-42, doi:10.3997/1365-2397.2007028.
- Hall, K., K. Bertram, M. Bertram, and D. Lawton, 2011, New Zealand acquisition, Spring 2011, CREWES Research Report, **23**, University of Calgary.
- Hampton, S.J. and J.W. Cole, 2009, Lyttelton Volcano, Banks Peninsula, New Zealand: Primary volcanic landforms and eruptive centre identification, *Geomorphology*, **104**, 3-4, 284-298.
- Henley, D., 2003, Coherent noise attenuation in the radial trace domain, *Geophysics*, **68**, **4**, 1408-1416. doi: 10.1190/1.1598134
- Hicks, S.R., 1989, Structure of the Canterbury Plains, New Zealand, from Gravity Modelling, Research Report Issue 222 (Geophysics Division), Department of Scientific and Industrial Research, Wellington.
- Hilterman, F.J., 1970, Three-dimensional seismic modeling: *Geophysics*, **35**, 1020-1037, doi: 10.1190/1.1440140.
- Holden, C., J. Beaven, B. Fry, M. Reyners, J. Ristau, R. Van Dissen, P. Villamor, M. Quigley, 2011, Preliminary source model of the Mw 7.1 Darfield earthquake from geological, geodetic and seismic data, In: Proceedings of the Ninth Pacific Conference on Earthquake Engineering, Building an Earthquake-Resilient Society, 14-16 April, 2011, Auckland, New Zealand.

- Howell D.G., D.L. Jones, and E.R. Schermer, 1985, Tectonostratigraphic terranes of the Circum-Pacific region, in Howell, D.G., ed., Tectonostratigraphic terranes of the Circum-Pacific region: Circum-Pacific Council for Energy and Mineral Resources, Earth Science Series, **1**, 3-31.
- Inazaki, T., 2004, In Situ measurement of the liquefaction potential of soils using a shear-wave vibrator, The Proceedings of 1st International Workshop on Active Monitoring in Solid Earth Geophysics (IWAM04), 347-354.
- Ivanov, J., R.D. Miller, P. Lacombe, C.D. Johnson, and J.W. Jr. Lane, 2006, Delineating a shallow fault zone and dipping bedrock strata using multichannel analysis of surface waves with a land streamer, *Geophysics*, **71**, 5, p. A39-A42. doi: 10.1190/1.2227521
- Ivanov, J., R.D. Miller, S. Peterie, C. Zeng., J. Xia, and T. Schwenk, 2011, Multi-channel analysis of surface MASW (MASW) of models with high shear-wave velocity contrast, 2011 SEG Annual Meeting, September 18 - 23, 2011 , San Antonio, Texas.
- Iwasaki, T., F. Tatsuoka, K., Tokida, and S. Yasuda, 1978, A practical method for assessing soil liquefaction potential based on case studies at various sites in Japan, Proc., 2nd Int. Conf. on Microzonation, San Francisco, 885–896.
- Jongens, R., D.J.A. Barrell, J.K. Campbell, J.R. Pettinga, 2012, Faulting and folding beneath the Canterbury Plains identified prior to the 2010 emergence of the Greendale Fault, *New Zealand Journal of Geology and Geophysics*, **55**, 3, 169-176. doi: 10.1080/00288306.2012.674050.
- Jongens, R., J.R. Pettinga, and J.K. Campbell, 1999, Stratigraphic and structural overview of the onshore Canterbury basin: North Canterbury to the Rangitata river, Prepared for Indo-Pacific Energy (NZ) Ltd., Ministry of Economic Development Unpublished Petroleum Report PR4067.
- Kaiser , A.E., H. Horstmeyer, A.G. Green, F.M. Campbell, R.M. Langridge, and A.F. McClymont, 2011, Detailed images of the shallow Alpine Fault Zone, New Zealand,

- determined from narrow-azimuth 3D seismic reflection data: *Geophysics*, **76**, no. 1, B19-B31, doi: 10.1190/1.3515920.
- Katz, H.R, and G. Kliewer, 1970, Petroleum developments in the Southwest Pacific region during 1969, *The American Association of Petroleum Geologists Bulletin*, **54**, 8, 1581-1586.
- Kayabali, K., 1996, Soil liquefaction evaluation using shear wave velocity, *Engineering Geology*, **44**, 121-127.
- King, P., 2000, New Zealand's changing configuration in the last 100 million years: plate tectonics, basin development, and depositional setting, *New Zealand Oil Exploration Conference Proceedings*: 132-146. Wellington, Ministry of Economic Development.
- Kirkaldy, P.H.S , M.F. Ridd, and E.G. Thomas, 1963, 'Seismic Survey, Canterbury Plains. Operator: BP Shell and Todd Petroleum Development Ltd. Reprocessed data from Indo-Pacific.' Unpublished open file Petroleum Report PR328.
- Kleffmann , S., F. Davey , A. Melhuish , D. Okaya , T. Stern, and SIGHT Team, 1998, Crustal structure in the central South Island, New Zealand, from the Lake Pukaki seismic experiment, *New Zealand Journal of Geology and Geophysics*, **41**, 39-49.
- Lai, C.G., 2005, Surface waves in dissipative media: Forward and inverse modelling, In: Lai,C.G, Wilmanski, K (eds) *Surface waves in geomechanics: direct and inverse modelling for soils and rocks*, CISM Series, Number 481. Springer-Verlag, Wien-Newyork (2005), 74-163.
- Laird, M.G., and J.D. Bradshaw, 2004, The Break-up of a Long-term Relationship: the Cretaceous Separation of New Zealand from Gondwana, *Gondwana Research*, **7**, 1, 273-286.
- Lamarche, G. and J.F. Lebrun, 2000, Transition from strike-slip faulting to oblique subduction: active tectonics at the Puysegur Margin, South New Zealand, *Tectonophysics*, **316**, 67-89.

- Landis, C.A. and D.S. Coombs, 1967, Metamorphic belts and orogenesis in southern New Zealand, *Tectonophysics*, **4**, 4, 501-518.
- Lawton, D.C., G.F. Margrave, and E.V. Gallant, 1998, Physical modeling of an anisotropic thrust, *CREWES Research Report*, **10**, no. 15, 1-9.
- Lawton, D.C., S.P. Cheadle, E.V. Gallant, and M.B. Bertram, 1989, Elastic physical modeling, *CREWES Research Report*, **19**, 273-288.
- Lin, C.P., C.C. Chang, and T.S. Chang, 2004, The use of MASW method in the assessment of soil liquefaction potential, *Soil Dynamics and Earthquake Engineering*, **24**, 689–698. doi:10.1016/j.soildyn.2004.06.012
- Lindsey, J., 1989, The Fresnel zone and its interpretative significance: The Leading Edge, **8**, 33–39, doi: 10.1190/1.1439575.
- Luo, Y., J. Xia, J. Liu, Y. Xu, and Q. Liu, 2008, Generation of a pseudo-2D shear-wave velocity section by inversion of a series of 1D dispersion curves, *Journal of Applied Geophysics*, **64**, 115-124. doi: 10.1016/j.jappgeo.2008.01.003
- MacKinnon, T.C., 1983, Origin of the Torlesse terrane and collevial rocks, South Island, New Zealand, *Geological Society of America Bulletin*, **94**, 967-985.
- Miller, R.D., J. Xia, C.B. Park, 1999, MASW to investigate subsidence in the Tampa, Florida area, *Kansas Geological Survey: Open-file Report 99-33*.
- Molnar, P, T. Atwater, J. Marrerickx, and S.M. Smith, 1975, Magnetic Anomalies, Bathymetry and the Tectonic Evolution of the South Pacific since the Late Cretaceous, *Geophys. J. R. astr. SOC*, (1 975) 40, 383-320.
- Mooney, W.D., and A. Ginzburg, 1986, Seismic measurements of the internal properties of fault zones: *Pure and Applied Geophysics*, **124**, 141-157, doi: 10.1007/BF00875723.

- Mortimer, N., 2004, New Zealand's geologic foundations, *Gondwana Research*, **7**, **1**, 261-272.
- Nazarian, S., K.H. Stokoe, II, and W.R. Hudson, 1983, Use of spectral analysis of surface wave method for determining moduli and thickness of pavement systems, *Transportation Research Record 930, Pavement Design, Performance, and Rehabilitation*, Washington, D.C., 38-45.
- Nichol, A., C. Mazengarb, F.Chanier, G. Rait, C.Uruski, and L. Wallace, 2007, Tectonic evolution of the active Hikurangi subduction margin, New Zealand, since the Oligocene, *Tectonics*, **26**, 24p.
- Nichol, A., and J. Beaven, 2003, Shortening of an overriding plate and its implications for slip on a subduction thrust, central Hikurangi Margin, New Zealand, *Tectonics*, **22**, **6**, 1070, doi:10.1029/2003TC001521
- Norris, R.J., and A.F. Cooper, 2001, Late quaternary slip rates and slip partitioning on the Alpine Fault, New Zealand, *Journal of Structural Geology*, **23**, 507-520.
- Norris, R.J., P.O. Koons, and A.F. Cooper, 1990, The obliquely-convergent plate boundary in the South Island of New Zealand: implications for ancient collision zones, *Journal of Structural Geology*, **12**, 5/6, 715-725.
- Orense, R.P., 2011, Soil liquefaction during the 2010 Darfield and 1990 Luzon Earthquakes: A comparative study, *Proc. 9th Pacific Conference on Earthquake Engineering*, Auckland, 14 April - 16 April, 2011, Paper 043, 8 pp.
- Owen, G., 1987, Deformation processes in unconsolidated sands, *Geological Society, London, Special Publications*, **29**, 11-24. doi: 10.1144/GSL.SP.1987.029.01.02
- Park, C.B., J. Xia, and R.D. Miller, 1998, Imaging dispersion curves of surface waves on multi-channel record; *SEG Expanded Abstracts*, 1377-1380. doi: 10.1190/1.1820161

- Park, C.B., R.D. Miller, and J. Xia, 1999, Multichannel analysis of surface waves, *Geophysics*, **64**, 3, 800-808. doi: 10.1190/1.1444590
- Park, C.B., 2003, SurfSeis © Multichannel Analysis of Surface Waves User's Manual v. 1.5, Brohammer, M. (Ed.), Kansas Geological Survey.
- Park, C.B., R.D. Miller, J. Xia, and J. Ivanov, 2007, Multichannel analysis of surface waves (MASW) —active and passive methods, *The Leading Edge (TLE)*, **26**, 1, 60-64. doi: 10.1190/1.2431832
- Park, C.B. and M. Carnevale, 2010, Optimum MASW Survey – Revisit after a decade of use, *GeoFlorida 2010: Advances in Analysis, Modeling & Design, Soil and Geotechnical System Characterization*, 1303-1312. doi: 10.1061/41095(365)130
- Pease, J.W. and T.D. O'Rourke, 1997, Seismic response of liquefaction sites, *Journal of Geotechnical Geoenvironmental Engineering*, **123**, 37-45. doi: 10.1061/(ASCE)1090-0241(1997)123:1(37)
- Pelekis, P.C. and G.A. Athanasopoulos, 2011, An overview of surface wave methods and a reliability study of a simplified inversion technique, *Soil Dynamics and Earthquake Engineering*, 31, 1654-1668. doi:10.1016/j.soildyn.2011.06.012
- Pelton, J.R., 2005, Near-surface seismology: Surface-based methods, in *Near-Surface Geophysics*, edited by D.K. Butler, *Investigations in Geophysics*, No. 13, Society of Exploration Geophysicists, Tulsa, OK, 219-263.
- Pettinga, J., M.D. Yetton, R.J. Van Dissen, and D. Downes, 2001, Earthquake source identification and characterization for the Canterbury Region, South Island, New Zealand, *Bulletin for the New Zealand society for earthquake engineering*, **34**, 4, 282-317.
- Pillans, B., 1991, New Zealand Quaternary stratigraphy: an overview, *Quaternary Science Reviews*, **10**, 405-418.

- Quigley, M., R. Van Dissen, P. Villamor, N. Litchfield, D. Barrell, K. Furlong, T. Stahl, B. Duffy, E. Bilderback, D. Noble, D. Townsend, J. Begg, R. Jongens, W. Ries, J. Claridge, A. Klahn, H. Mackenzie, A. Smith, S. Hornblow, R. Nicol, S. Cox, R. Langridge, K. Pedley, 2010, Surface rupture of the Greendale Fault during the Mw 7.1 Darfield (Canterbury) earthquake, New Zealand: Initial findings, *Bulletin of the New Zealand Society for Earthquake Engineering*, 43, 4, 236-242.
- Reyners, M., 1998, Plate coupling and the hazard of large subduction thrust earthquakes at the Hikurangi subduction zone, New Zealand, *New Zealand Journal of Geology and Geophysics*, 41, 343-354.
- Richart, F.E., R.D. Woods, and J.R. Hall, 1970, *Vibrations of Soils and Foundations*, Prentice-Hall Inc., New Jersey.
- Rix, G.J., 2005, Near site characterization using surface waves, In: Lai, C.G, Wilmanski, K (eds) *Surface waves in geomechanics: direct and inverse modelling for soils and rocks*, CISM Series, Number 481. Springer-Verlag, Wien-New York (2005), 1-46.
- Roth, M. and K. Holliger, 1999, Inversion of source generated noise in high-resolution seismic data, *The Leading Edge*, 18, 12, 1402-1406. doi: 10.1190/1.1438230
- Schwab, F.A. and L. Knopoff, (1972), Fast surface wave and free mode computations, In: *Methods of computational physics*, 11, ed. B.A. Bolt: Academic Press, 87-180.
- Sheriff, R.E., 1991, *Encyclopedic Dictionary of Exploration Geophysics*, Geophysical References Series, Vol. 1, 3rd edition: Society of Exploration Geophysicists
- Sibson, R.H., F.C Ghisetti, R.A. Crookbain, 2012, Andersonian wrench faulting in a regional stress field during the 2010-2011 Canterbury, New Zealand, earthquake sequence, *Geological Society, London, Special Publications*, 367, 7-18, doi: 10.1144/SP367.2.

- Smith, E.G.C., T. Stern, and B. O'Brien, 1995, A seismic velocity profile across the central South Island, New Zealand, from explosion data, *New Zealand Journal of Geology and Geophysics*, **38**, 565-570.
- Srbulov, M., 2008, *Geotechnical Earthquake Engineering: Simplified Analysis with Case Studies and Examples*, Vol. 9, Ed. Ansal, A., Springer, New York.
- Stacey, F.D., 1992, *Physics of the Earth*, 3rd edition, Brookfield Press, Queensland, Australia.
- Stirling, M., J. Pettinga, K. Berryman, and M. Yetton, 2001, Probabilistic seismic hazard assessment of the Canterbury region, New Zealand, *Bulletin of the New Zealand society for earthquake engineering* **34**, 4, 318-334.
- Stokoe K.H., J.M. Roesset, J.G. Bierschwale, and M. Aouad, 1988, Liquefaction potential of sands from shear wave velocity, *Proceedings of the Ninth World Conference on Earthquake Engineering*, August 2-8, 1988, Tokyo-Kyoto, Japan, **3**, 213 – 218.
- Stokoe, K.H. II, S.G. Wright, J.A. Bay, and J.M. Roesset, 1994, "Characterization of Geotechnical Sites by SASW Method," ISSMFE Technical Committee #10 for XIII ICSMFE, *Geophysical Characterization of Sites*, A. A. Balkema Publishers/Rotterdam & Brookfield, Netherlands, \ 15-25.
- Sun, S., and J.C. Bancroft, 2001, How much does the migration aperture actually contribute to the migration result?, *CREWES Research Report 2001*, **37**.
- Sundararajan, N., and T. Seshunarayana, 2011, Liquefaction hazard assessment of earthquake prone area: A study based on shear wave velocity by multichannel analysis of surface waves (MASW), *Geotechnical and Geological Engineering*, **29**, 267–275. doi: 10.1007/s10706-010-9360-2
- Teichert, C., 1959, Australia and Gondwana, *Geologische Rundschau*, **47**, 2, 562-590.

- Tokimatsu, K., S. Tamura, and H. Kojima, 1992, Effects of multiple modes on Rayleigh wave dispersion characteristics, *Journal of Geotechnical Engineering*, **118**, 10, 1529-1543.
- Tonkin and Taylor Ltd., 2011, Darfield Earthquake Recovery Geotechnical Factual Report Bexley and Aranui, prepared January 2011 for the Earthquake Commission, T&T Ref. REP-BAX-FAC. Retrieved online from: <http://eqc-canterbury.web4biz.co.nz/publications/geotech-bexley-aranui?page=0,4>
- Townend, J., S. Sherburn, R. Arnold, C. Boese, and L. Woods, 2012, Three-dimensional variations in present day tectonic stress along the Australia-Pacific plate in New Zealand, *Earth and Planetary science letters*, **353-354**, 47-59.
- Trupti, S., K.N.S.S.S. Srinivas, P. Pavan Kishore, and T. Seshunarayana, 2012, Site characterization studies along coastal Andhra Pradesh—India using multichannel analysis of surface waves, *Journal of Applied Geophysics*, **79**, 82–89. doi: 10.1016/j.jappgeo.2011.12.006
- Van Dissen, R., D. Barrell, N. Litchfield, P. Villamor, M. Quigley, A. King, K. Furlong, J. Begg, D. Townsend, H. Mackenzie, T. Stahl, D. Noble, B. Duffy, E. Bilderback, J. Claridge, A. Klahn, R. Jongens, S. Cox, R. Langridge, W. Ries, R. Dhakal, A. Smith, S. Hornblow, R. Nicol, K. Pedley, H. Henham, R. Hunter, A. Zajac, and T. Mote, 2011. Surface rupture displacement on the Greendale Fault during the Mw 7.1 Darfield (Canterbury) earthquake, New Zealand, and its impact on man-made structures. In: Ninth Pacific Conference on Earthquake Engineering: Building an Earthquake-Resilient Society, Auckland, New Zealand 14-16 Apr 2011. Accessed 9 October 2011; <http://db.nzsee.org.nz/2011/186.pdf>.
- Villamore, P., N. Litchfield, D. Barrell, R. Van Dissen, S. Hornblow, M. Quigley, S. Levick, W. Ries, B. Duffy, J. Begg, D. Townsend, T. Stahl, E. Bilderback, D. Noble, K. Furlong, and H. Grant, 2012, Map of the 2010 Greendale Fault surface rupture,

- Canterbury, New Zealand: application to land use planning, *New Zealand Journal of Geology and Geophysics*, **55**, 3, 223-230. doi: 10.1080/00288306.2012.680473
- Wallace, L.M., M. Reyners, U. Cochran, S. Bannister, P.M. Barnes, K. Berryman, G. Downes, D. Eberhart-Phillips, A. Fagereng, S. Ellis, A. Nichol, R. McCaffrey, R.J. Beaven, S. Henrys, R. Sutherland, D. Barker, N. Litchfield, J. Townend, R. Robinson, R. Bell, K. Wilson, and W. Power, 2009, Characterizing the seismogenic zone of a major plate boundary subduction thrust: Hikurangi Margin, New Zealand, *Geochemistry Geophysics Geosystems*, **10**, 32 pp., doi:10.1029/2009GC002610
- Wandres, A.M., and J.D. Bradshaw, 2005, New Zealand tectonostratigraphy and implications from conglomerate rocks for the configuration of the SW Pacific margin of Gondwana. doi: 10.1144/GSL.SP.2005.246.01.06 Geological Society, London, Special Publications 2005, **246**, p. 179-216
- Wandres, A.M., J.D. Bradshaw, S. Weaver, R. Maas, T. Ireland, and N. Eby, 2004, Provenance of the sedimentary Rakaia sub-terrane, Torlesse Terrane, South Island, New Zealand: the use of igneous clast compositions to define the source, *Sedimentary Geology*, **168**, 193–226.
- Wang, X., C. Xia, and X. Liu, 2012, A case study: imaging OBS multiples of South China Sea, *Marine Geophysical Research*, **33**, 1, 89-95, doi:10.1007/s11001-012-9148-2.
- Widess, M.B., 1973, How thin is a thin bed?: *Geophysics*, **38**, 1176-1180, doi: 10.1190/1.1440403.
- Wilson, D.D., 1976, Hydrogeology of metropolitan Christchurch, *Journal of Hydrology (N.Z.)*, **15**, 2, 101-120.
- Wilson, D.D., 1985, Erosional and depositional trends in rivers of the Canterbury Plains, New Zealand, *Journal of Hydrology (N.Z.)*, **24**, 1, p. 32-44.
- Wong, J., R. Maier, E. Gallant, and D. Lawton, 2009a, Physical modeling of a 3D marine seismic survey, CREWES Research Report, 21, 1-10.

- Wong, J., K.W. Hall, E.V. Gallant, R. Maier, M.B. Bertram, and D.C. Lawton, 2009b, Seismic Physical Modelling at the University of Calgary, CSEG Recorder, **34**, p. 37-43.
- Wong J., F. Mahmoudian, and G. Margrave, 2011, Physical modeling III: acquiring modeled data for VVAZ/AVAZ analysis, CREWES Research Report, **23**, 1-17.
- Xia, J., R.D. Miller, and C.B. Park, 1999, Estimation of near-surface shear-wave velocity by inversion of Rayleigh waves, Geophysics, **64**, 3, 691-700. doi: 10.1190/1.1444578
- Xia, J., R.D. Miller, C.B. Park, J.A. Hunter, and J.B. Harris, 2000a, Comparing shear-wave velocity profiles from MASW with borehole measurements in unconsolidated sediments, Fraser River Delta, B.C., Canada, Journal of Environmental & Engineering Geophysics, **5**, 3, 1-13. doi: 10.4133/JEEG5.3.1
- Xia, J., R.D. Miller, and C.B. Park, 2000b, Advantages of calculating shear-wave velocity from surface waves with higher modes, SEG Expanded Abstracts, 70th Annual Meeting, Calgary, Alberta, Canada, 1295-1298. doi: 10.1190/1.1815633
- Xiao, H., Y.L. Young, and J.H. Prevost, 2010, Parametric study of breaking solitary wave induced liquefaction of coastal sandy slopes, Ocean Engineering, **35**, 1546-1553. doi: 10.1016/j.oceaneng.2010.09.014
- Yilmaz, O., 1987, Seismic data processing: Society of Exploration Geophysicists.
- Yoon, S. and G.J. Rix, 2009, Near-Field Effects on Array-Based Surface Wave Methods with Active Sources, Journal of Geotechnical and Geoenvironmental Engineering, **135**, 3, 399-406. doi: 10.1061/(ASCE)1090-0241(2009)135:3(399)
- Yunmin, C., K. Han, and C. Ren-peng, 2005, Correlation of shear wave velocity with liquefaction resistance based on laboratory tests, Soil Dynamics and Earthquake Engineering, **25**, 461-469. doi: 10.1016/j.soildyn.2005.03.003

APPENDIX A: GEOLOGIC TIMESCALE

GEOLOGIC TIME SCALE (Modified from Forsyth et al., 2008)

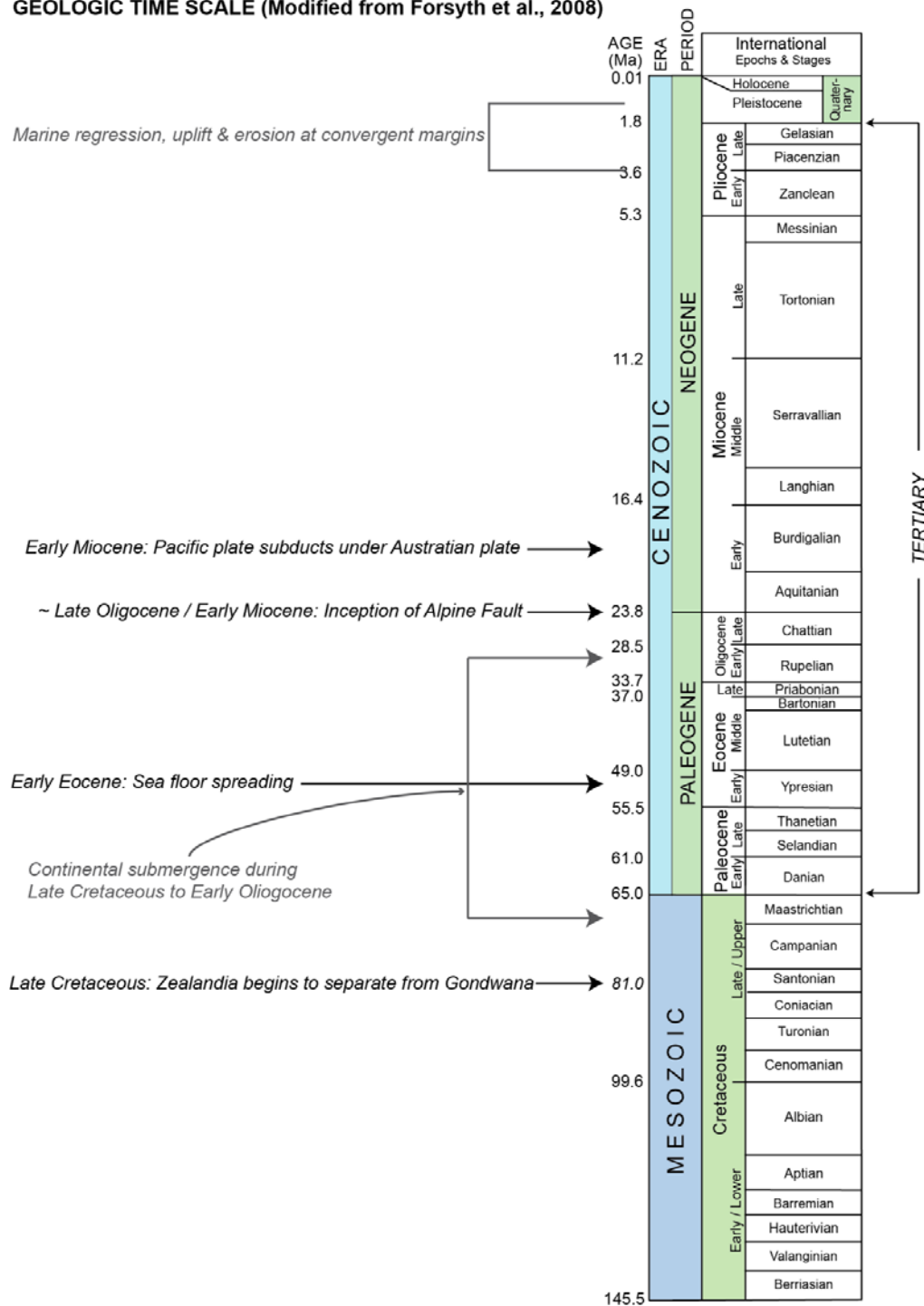


Figure A1. Geologic time scale listing events focused on New Zealand.

APPENDIX B: ENVIRONMENT CANTERBURY BEXLEY BOREHOLE

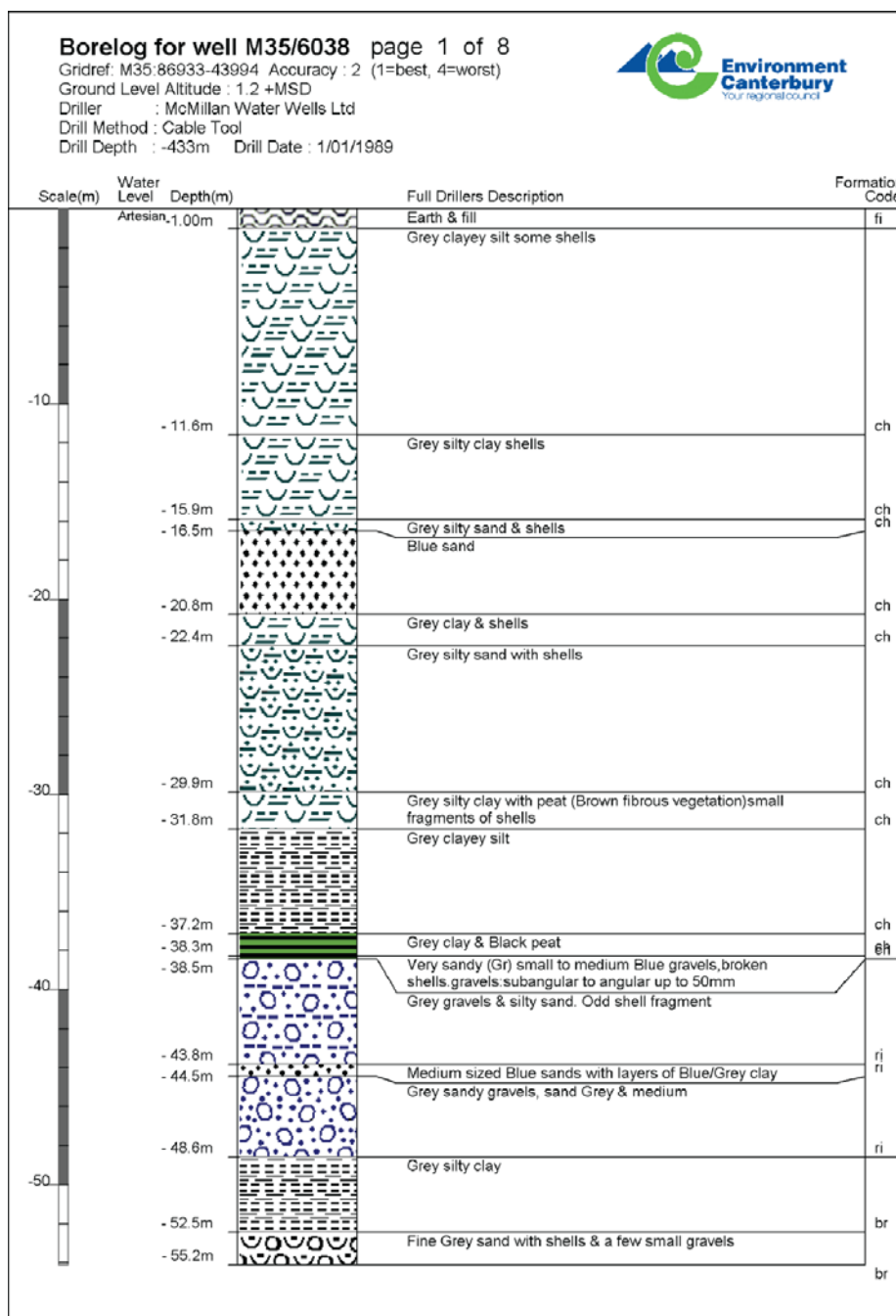


Figure B1-1. Environment Canterbury Well Log M35/6068 Bexley Borehole Page 1 of 8.

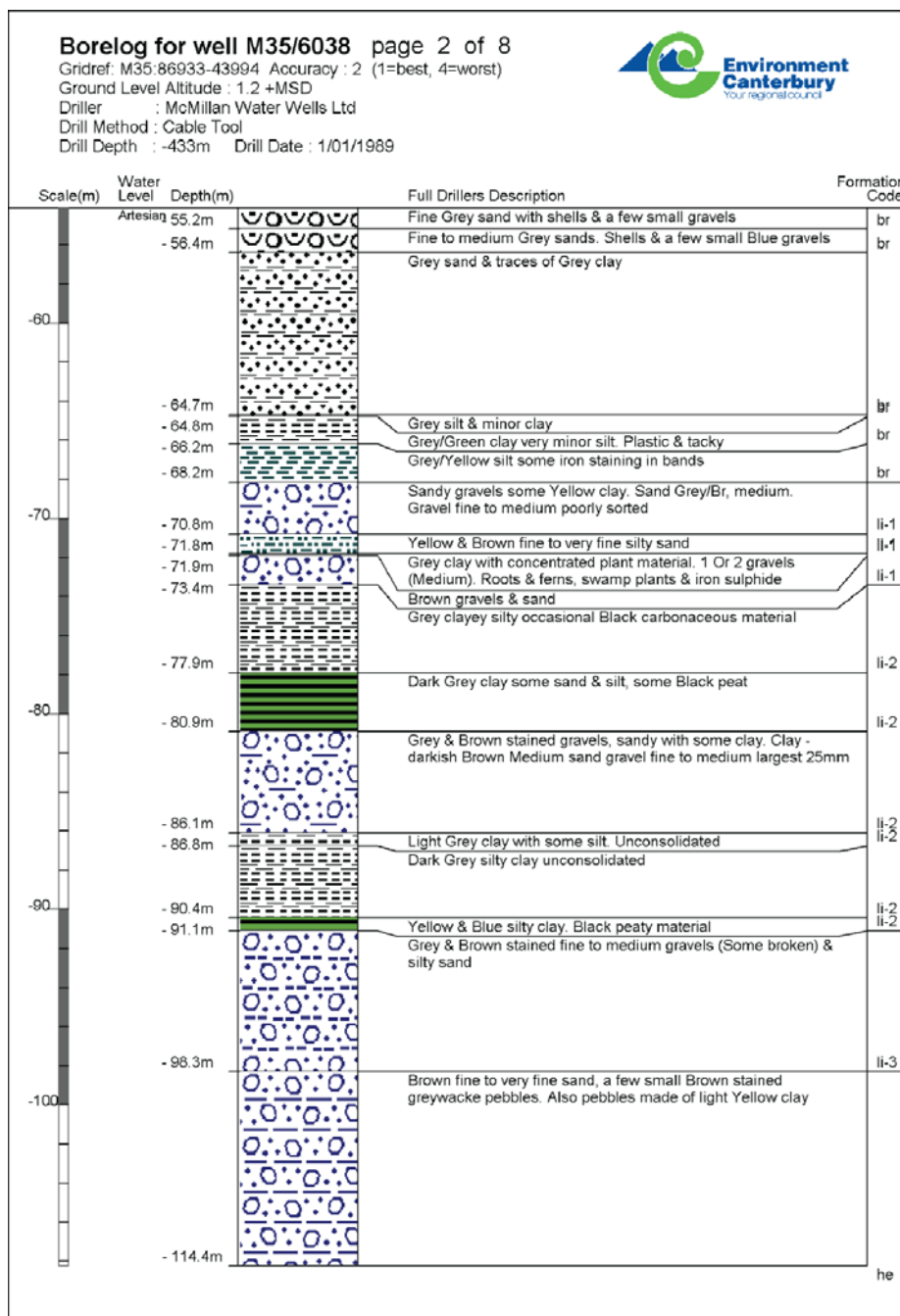


Figure B1-2. Environment Canterbury Well Log M35/6068 Bexley Borehole Page 2 of 8.

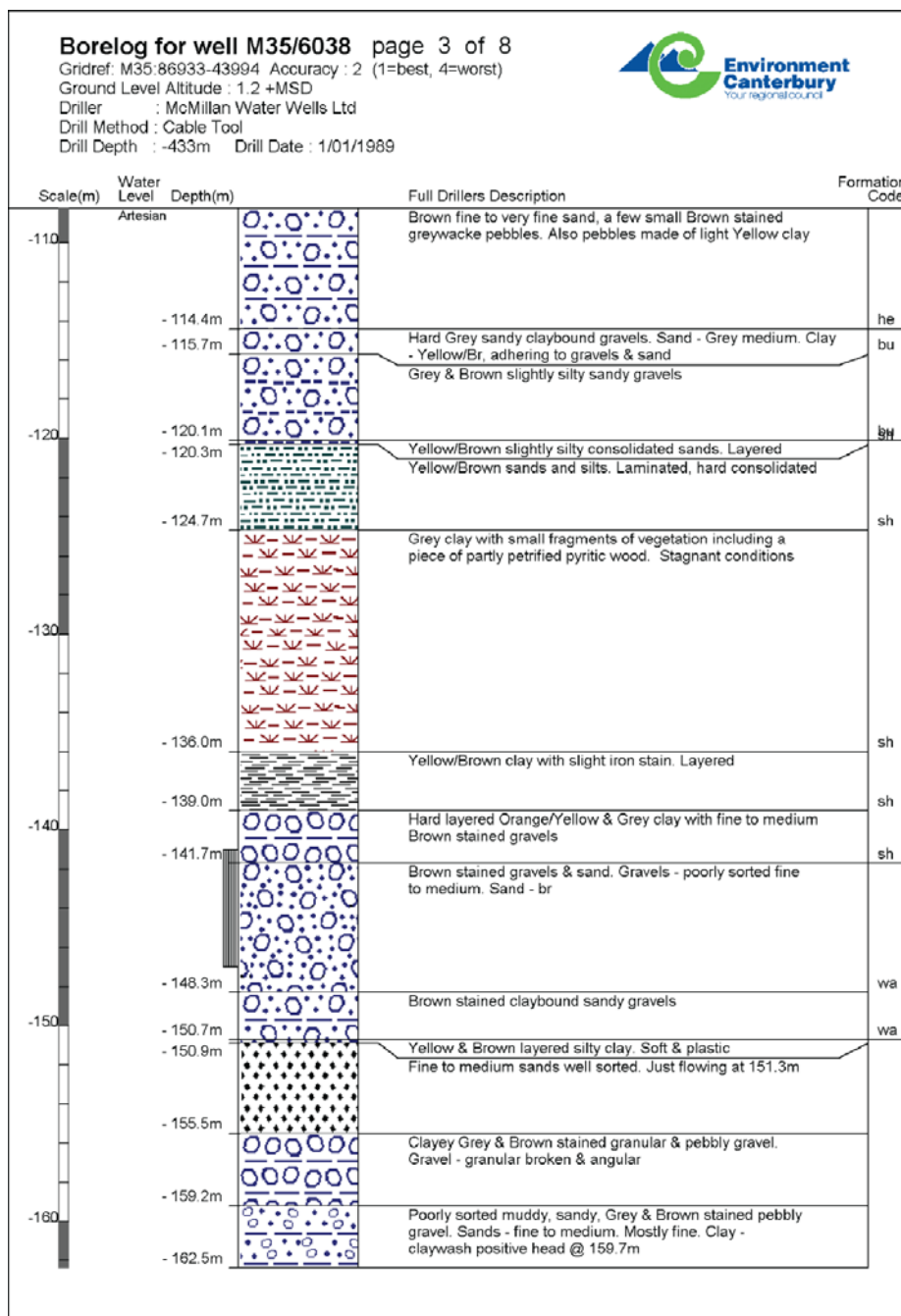


Figure B1-3. Environment Canterbury Well Log M35/6068 Bexley Borehole Page 3 of 8.

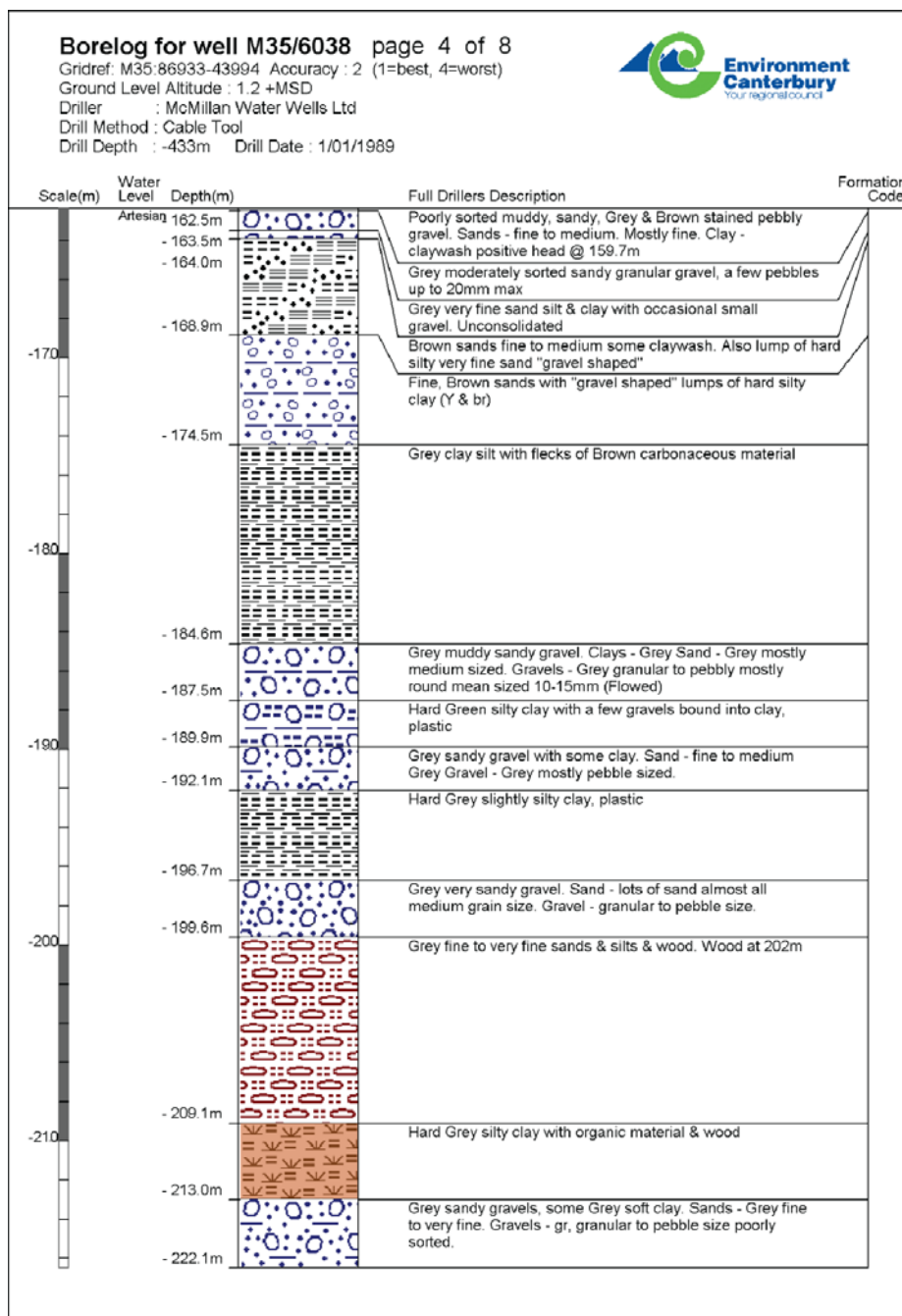


Figure B1-4. Environment Canterbury Well Log M35/6068 Bexley Borehole Page 4 of 8.

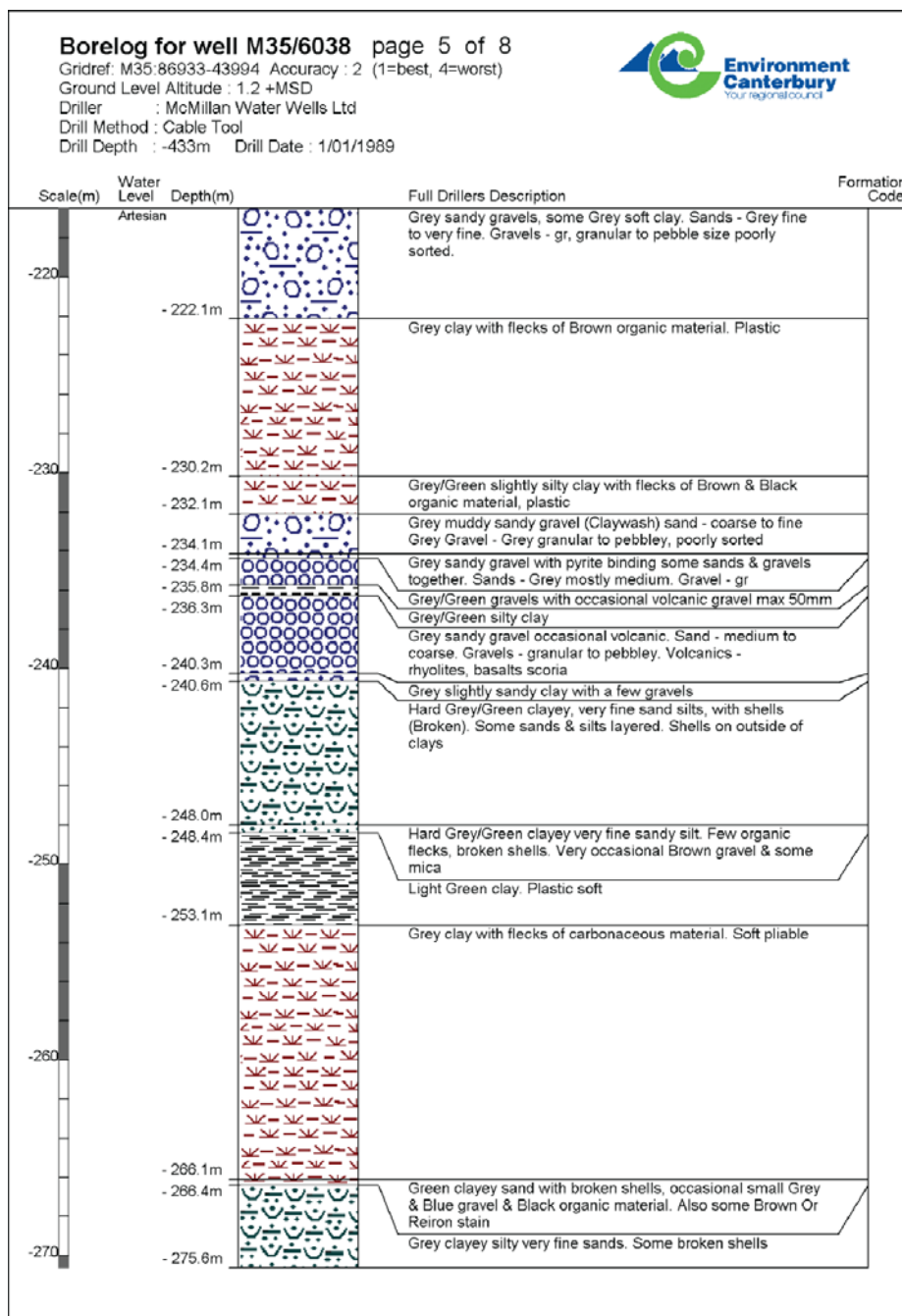


Figure B1-5. Environment Canterbury Well Log M35/6068 Bexley Borehole Page 5 of 8.

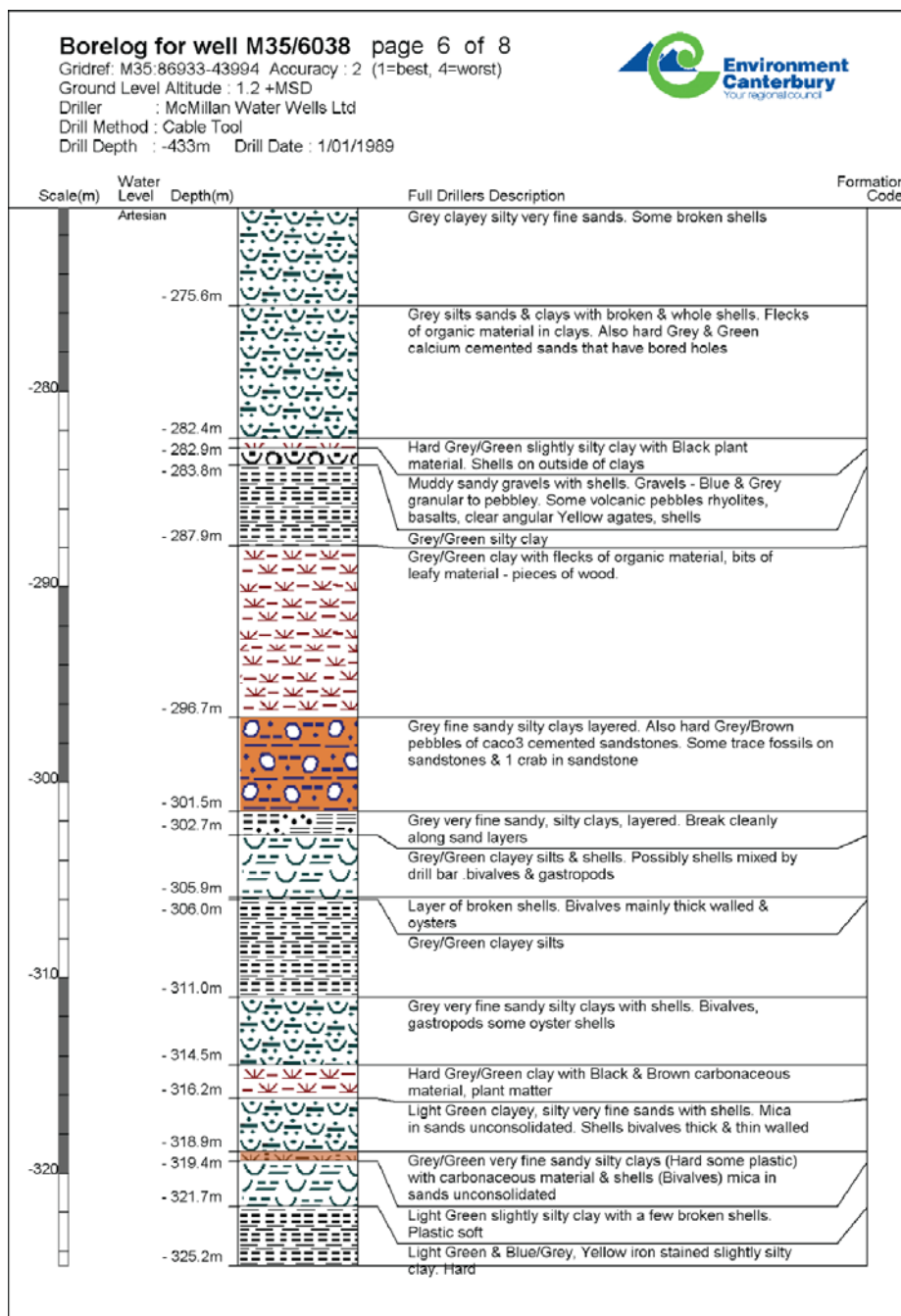


Figure B1-6. Environment Canterbury Well Log M35/6068 Bexley Borehole Page 6 of 8.

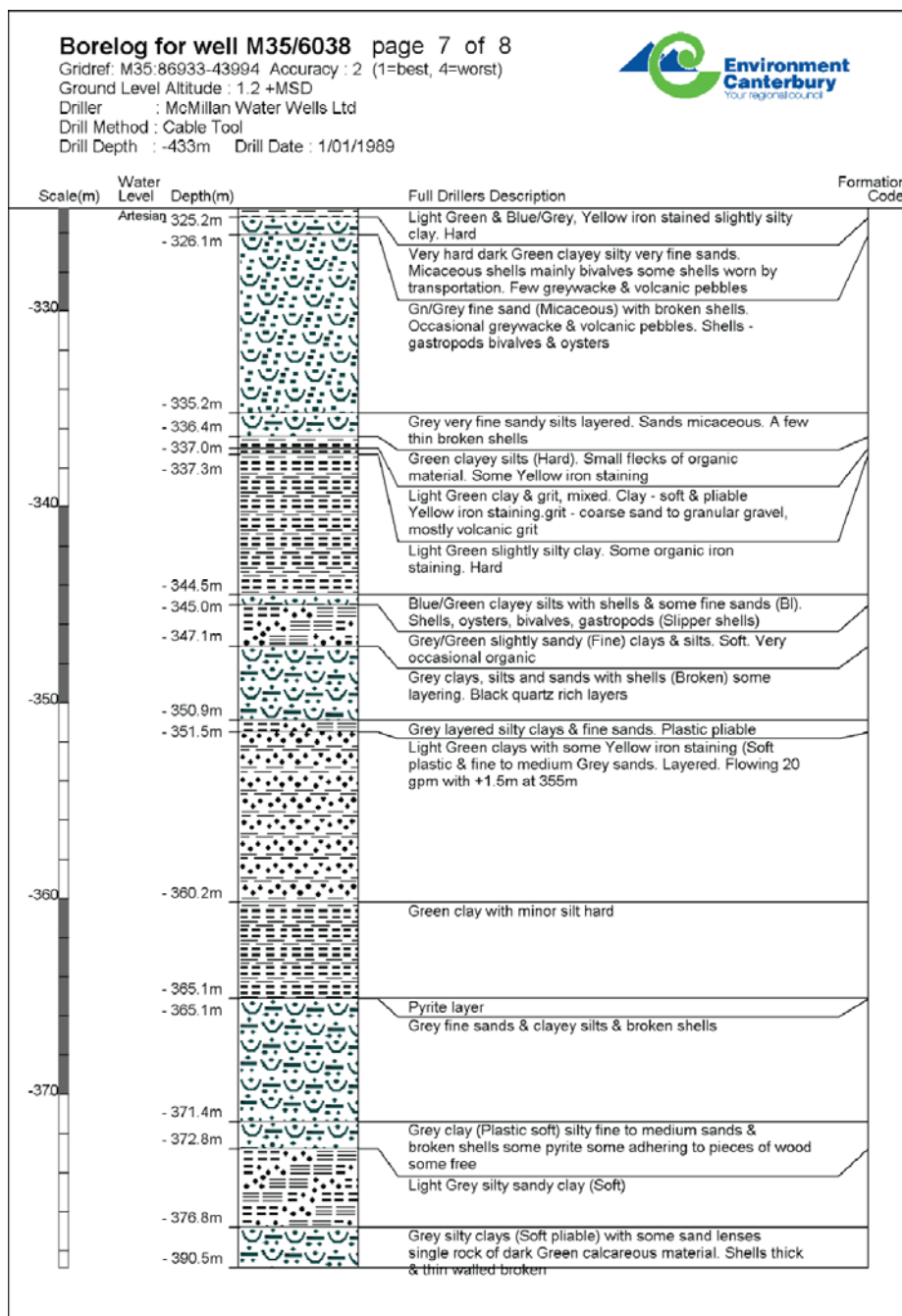


Figure B1-7. Environment Canterbury Well Log M35/6068 Bexley Borehole Page 7 of 8.

APPENDIX C: STACKING VELOCITIES OF SEISMIC DATA

C.1. Velocity structure beneath New Brighton Beach (Line 1)

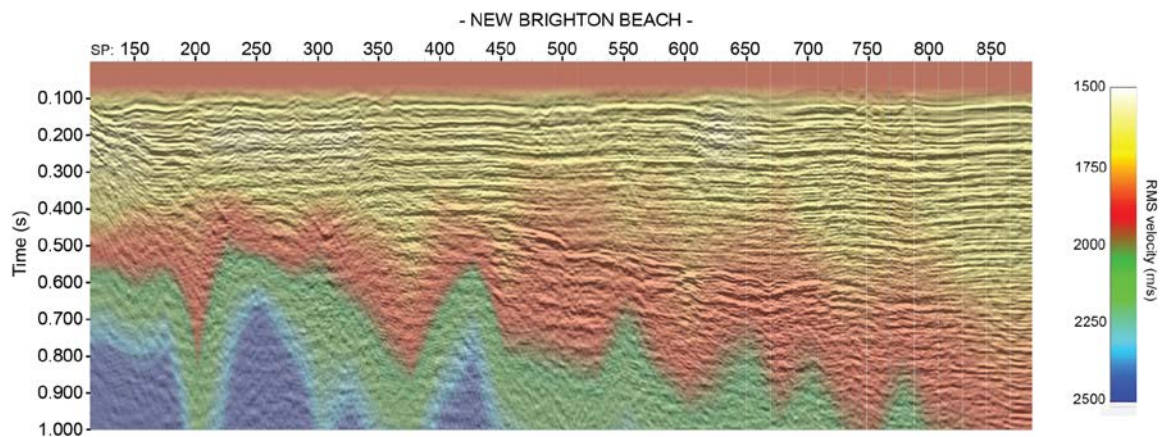


Figure C1. RMS velocities provided by Sensor Geophysical Ltd. and overlain on processed seismic data acquired at New Brighton Beach, Christchurch, New Zealand. Vertical exaggeration x2, for 2000 m/s.

C.2. Velocity structure beneath Barbadoes Street (Line 2)

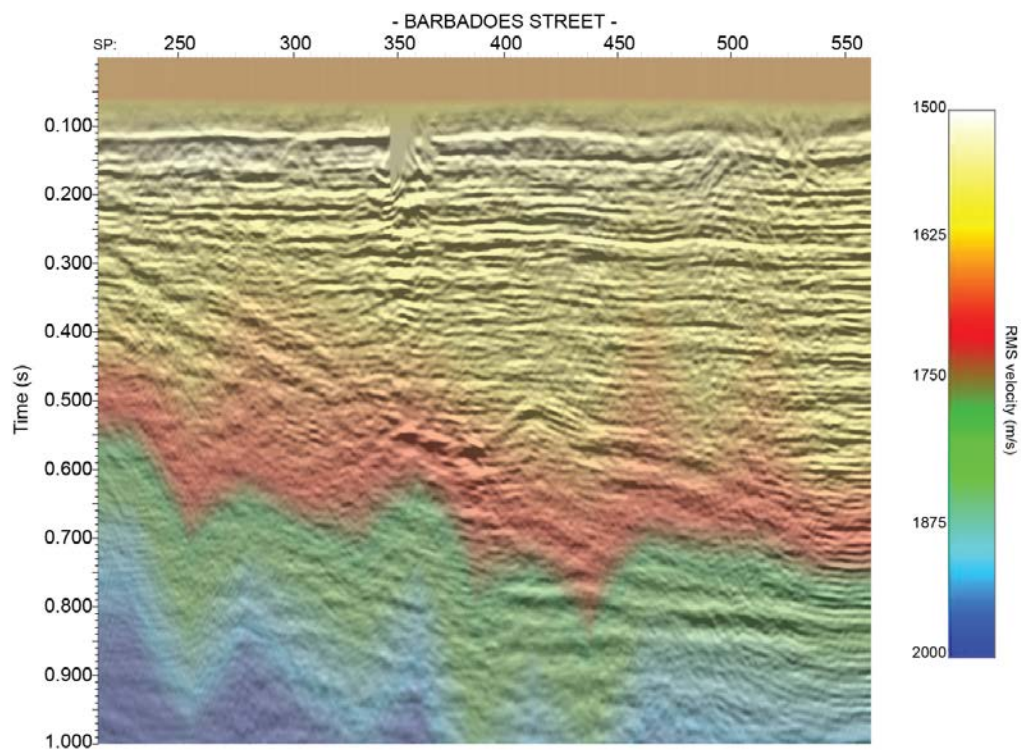


Figure C2. RMS velocities provided by Sensor Geophysical Ltd. and overlain on processed seismic data acquired at Barbadoes Street, Christchurch, New Zealand. Vertical exaggeration x2, for 2000 m/s.

C.3. Velocity structure beneath Highfield Road (Line 3)

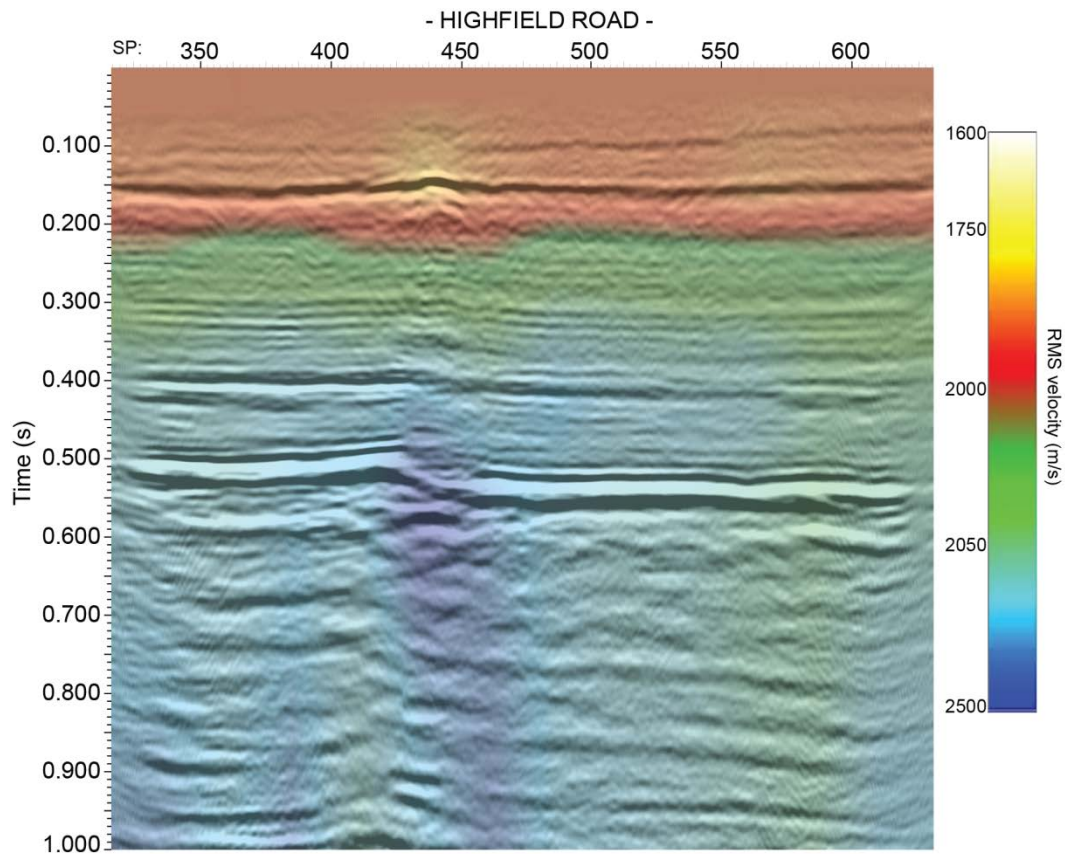


Figure C3. RMS velocities provided by Sensor Geophysical Ltd. and overlain on processed seismic data acquired at Highfield Road, Canterbury, New Zealand. Vertical exaggeration x2.5, for 2400 m/s.

APPENDIX D: ENVIRONMENTAL CANTERBURY WELL LOGS

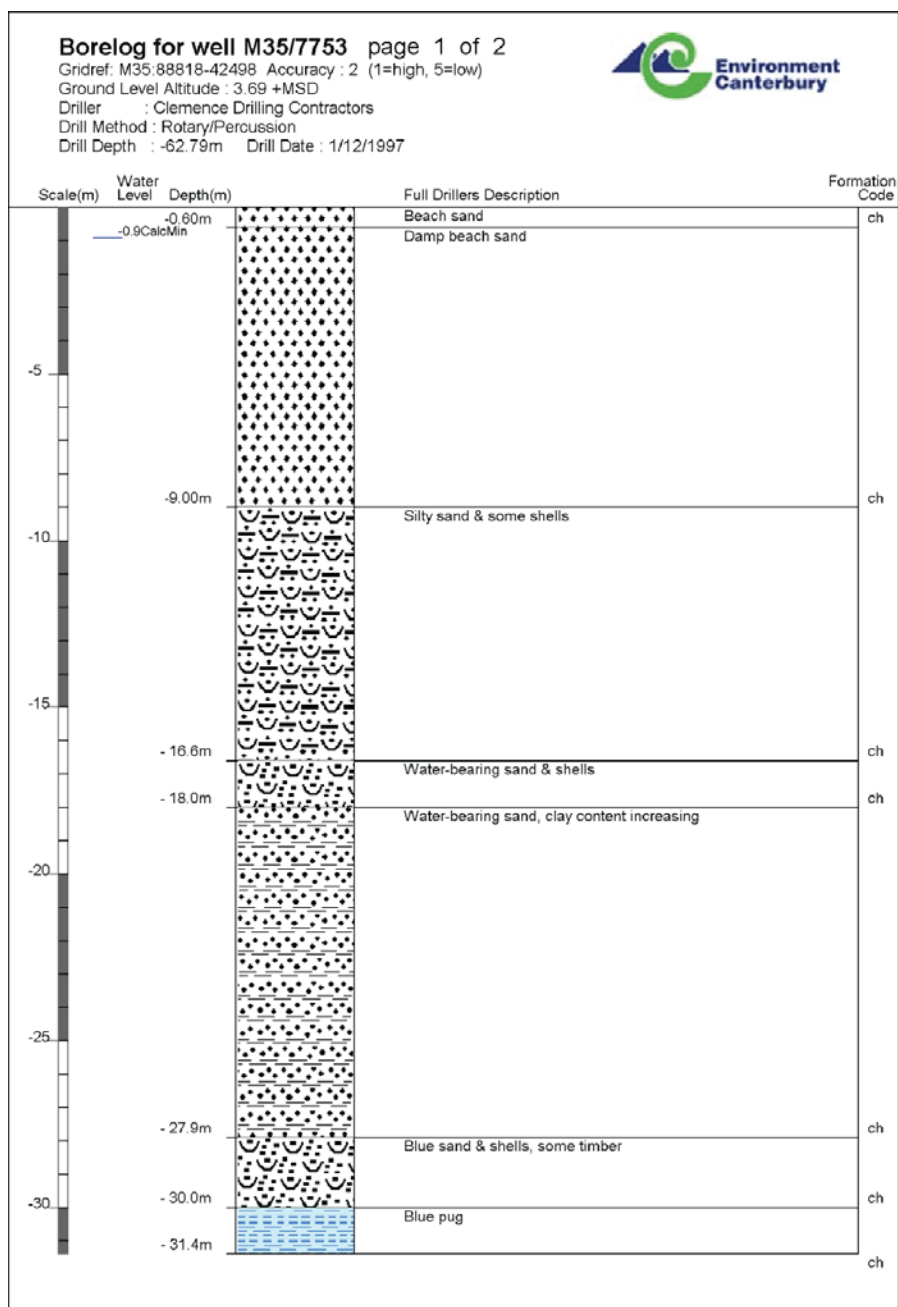


Figure D1-1. Environment Canterbury Well Log M35, New Brighton Beach. Page 1 of 2.

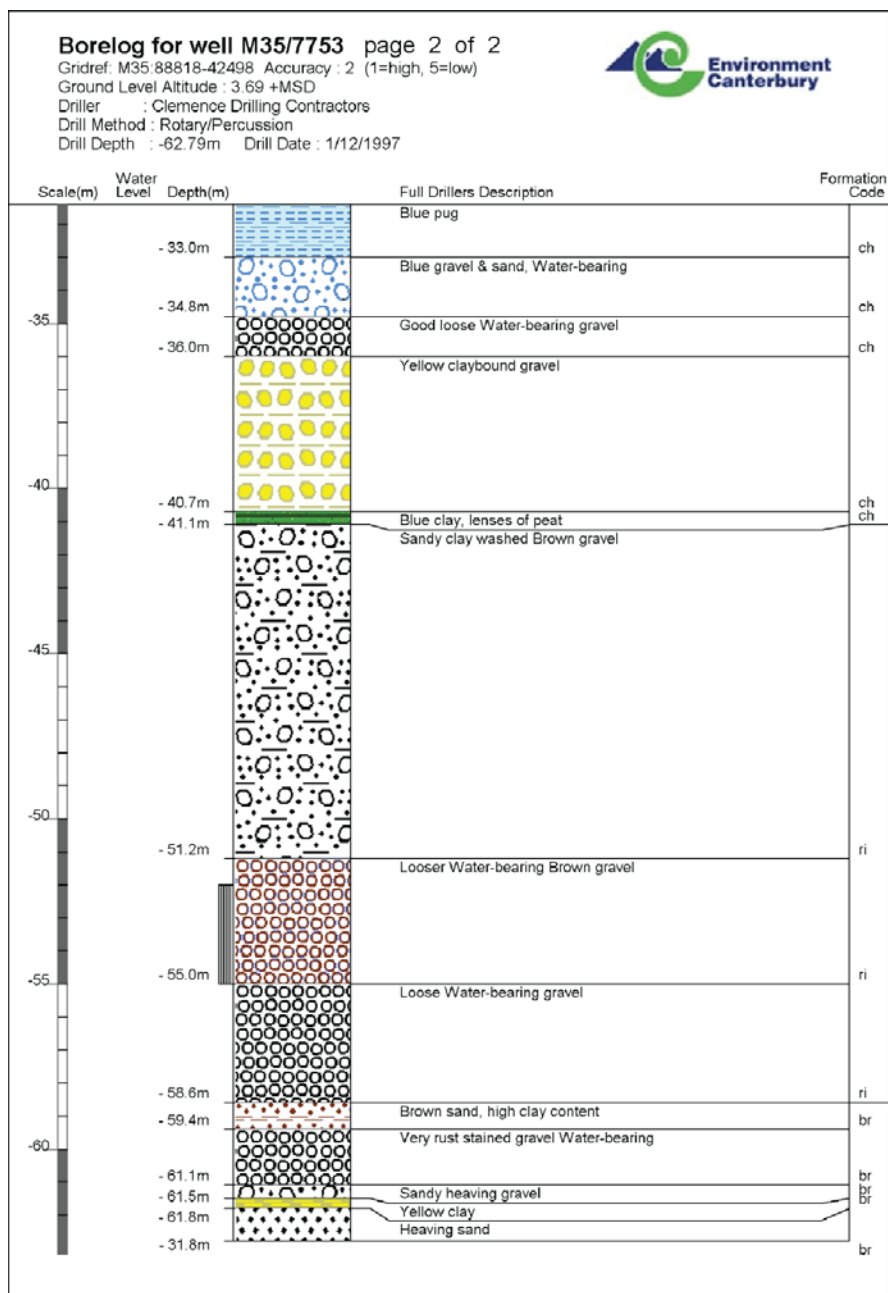


Figure D1-2. Environment Canterbury Well Log M35, New Brighton Beach. Page 2 of 2.

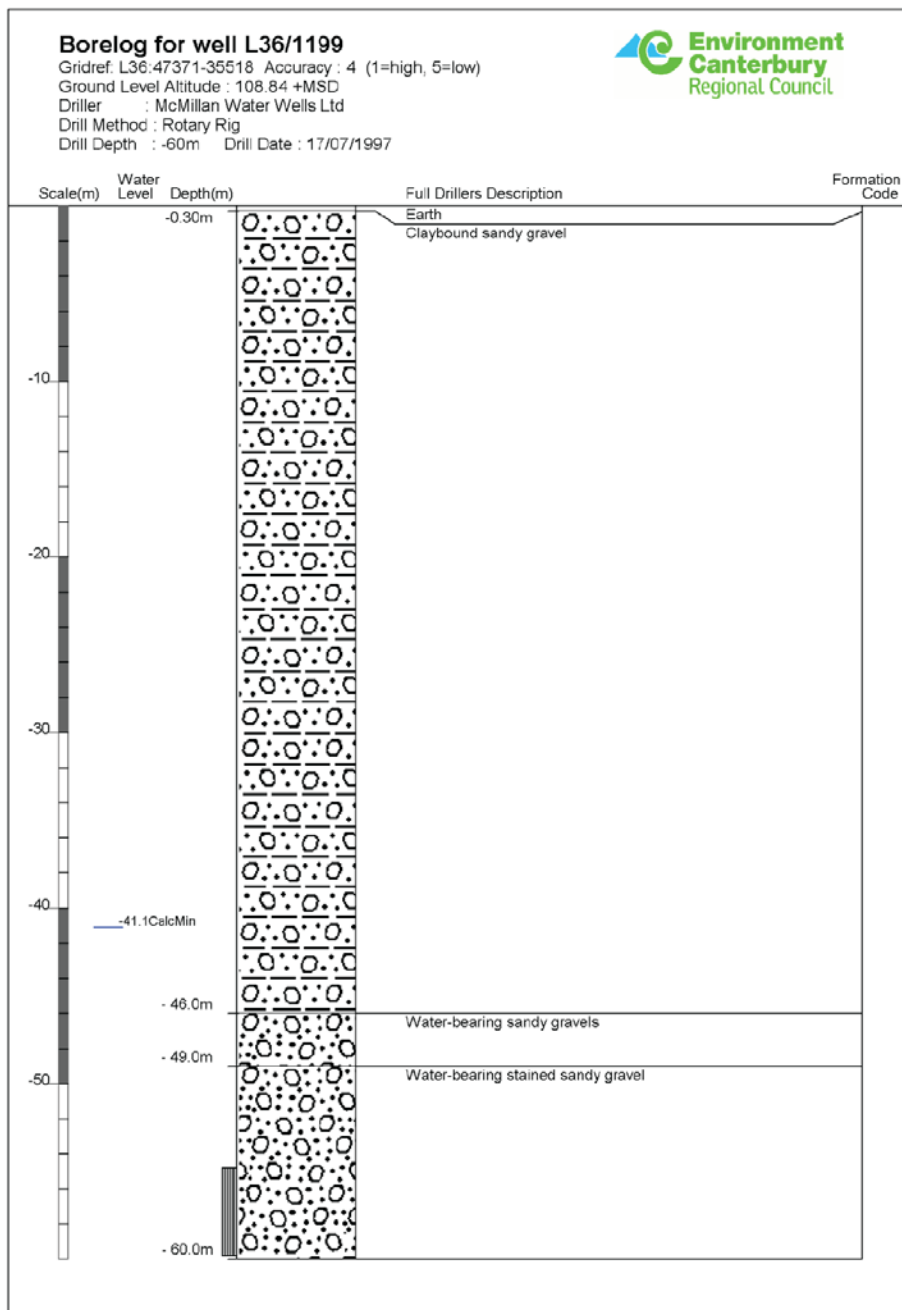
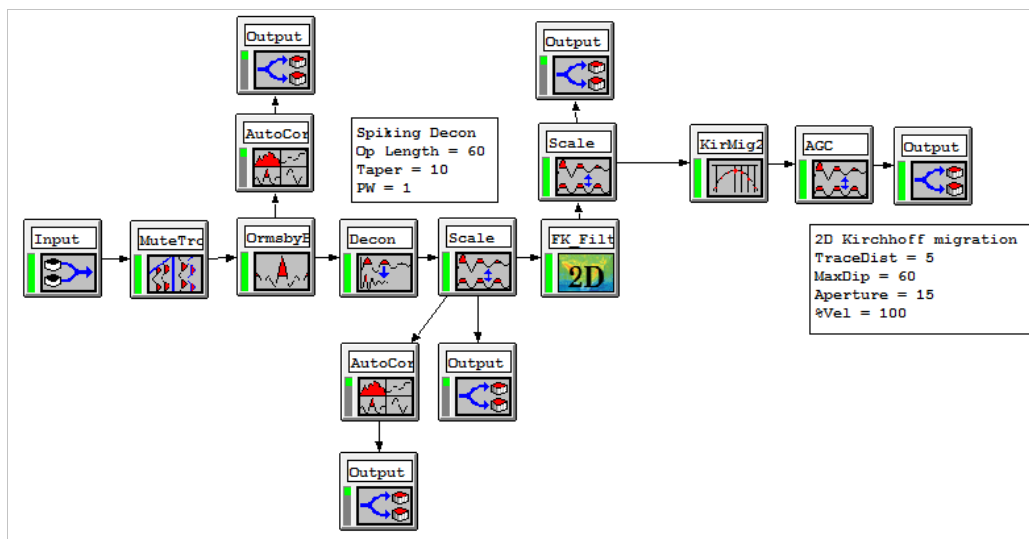


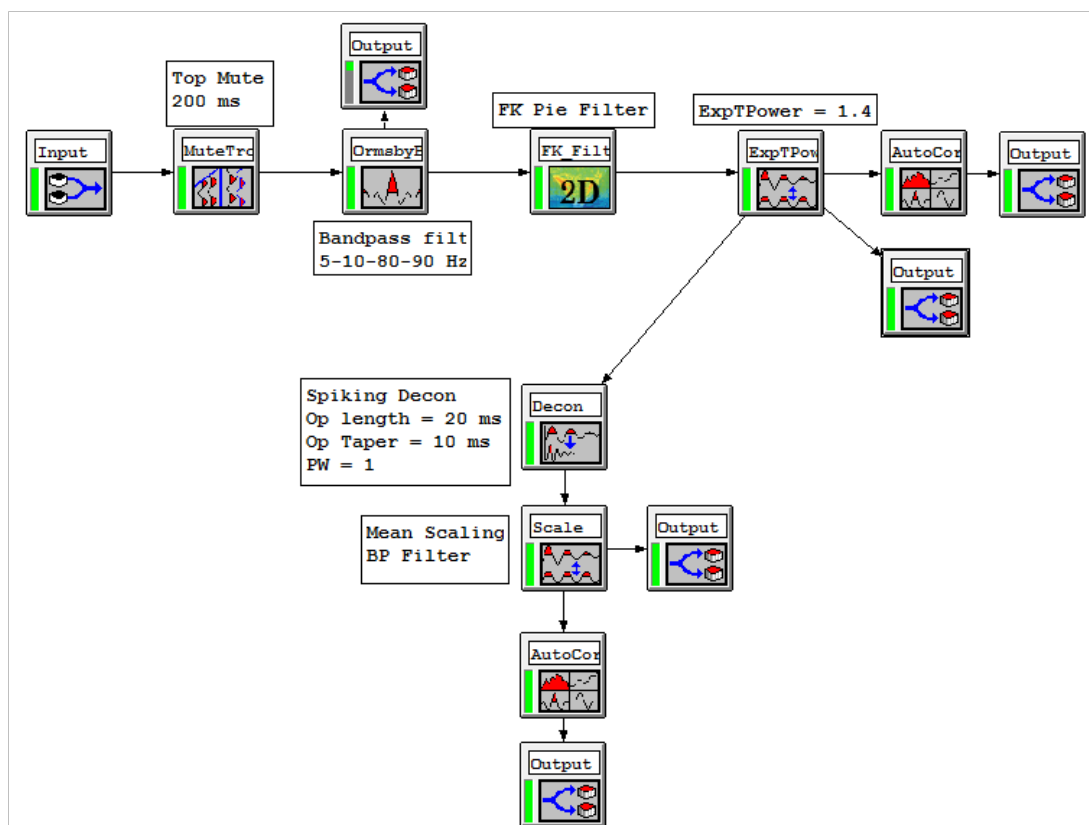
Figure D1-3. Environment Canterbury Well Log M35, Highfield Road Page 1 of 1.

APPENDIX E: PROCESSING JOB FLOWS FOR PHYSICAL MODELING

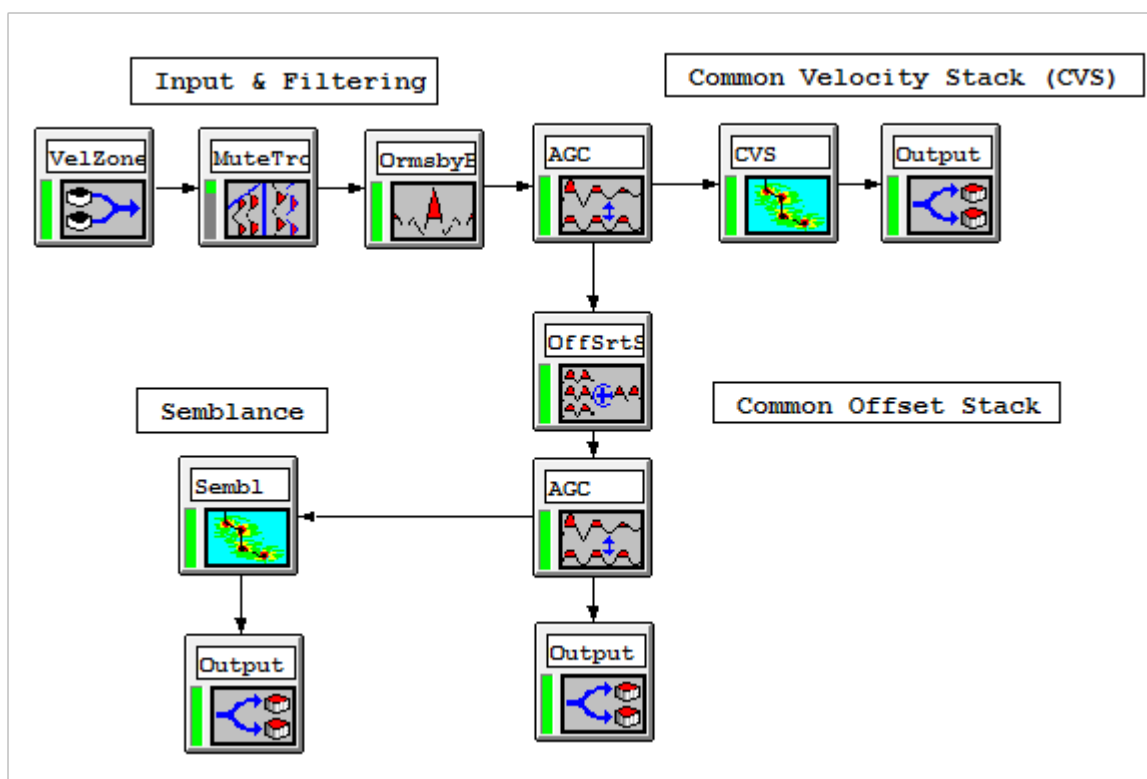
E.1. VISTA job flow created for zero-offset data



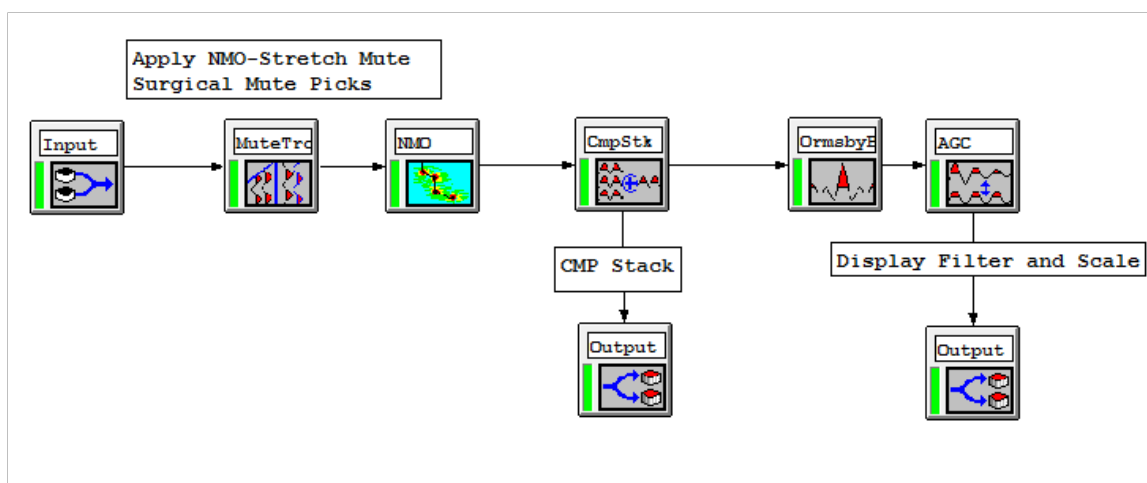
E.2. VISTA job flow for common-source data (Part 1: Filtering and deconvolution)



E.3. VISTA job flow for common-source data (Part 2: Velocity analysis)



E.4. VISTA job flow for common-source data (Part 3: Apply NMO and stack)



E.5. VISTA job flow for common-source data (Part 4: 2D Post-stack Kirchhoff migration)

